

UC Davis

UC Davis Electronic Theses and Dissertations

Title

Portable, Low Field Nuclear Magnetic Resonance: Theoretical Foundations and Field Applications

Permalink

<https://escholarship.org/uc/item/58h0s507>

Author

Fricke, Sophia Noelle

Publication Date

2021

Peer reviewed|Thesis/dissertation

Portable, Low Field Nuclear Magnetic Resonance:
Theoretical Foundations and Field Applications

By

SOPHIA NOELLE FRICKE
DISSERTATION

Submitted in partial satisfaction of the requirements for the degree of

DOCTOR OF PHILOSOPHY

in

Chemistry

in the

OFFICE OF GRADUATE STUDIES

of the

UNIVERSITY OF CALIFORNIA

DAVIS

Approved:

Matthew P. Augustine, Chair

Alexei A. Stuchebrukhov

R. David Britt

Committee in Charge

2021

ABSTRACT

Nuclear magnetic resonance (NMR) is a powerful chemometric method for any scientist because it is easily translated to a portable format. Recent advances have made portable NMR spectroscopy economically and practically feasible. Here, the foundational physics of spin dynamics is discussed as a bridge from the abstract theory of NMR to practical applications of low field relaxometry. Relaxometry can provide a window into the molecular dynamics of a system through measurement of spin relaxation rates, which directly relate to chemical interactions and mobility within a system.

The ease with which it can be customized makes portable NMR an extremely desirable technique for non-destructive, quantitative chemical analysis. However, portable NMR obtains a weaker signal with decreased resolution compared to traditional NMR. This is because spin states are not strongly split in low magnetic fields and are therefore populated nearly equally at thermodynamic equilibrium, causing weak longitudinal magnetization. As such, one typically measures exponential decay constants at low field rather than frequencies. Filtering and data analysis are considered with the development of the matrix pencil method (or MPM, so named after the mathematical entity which it employs) as a tool to aid in studies of low signal-to-noise systems and complex materials. Here, the MPM is explored first as a filtering strategy, and second, as a stable, reproducible data processing method in low field NMR. Currently, the inverse Laplace transform (ILT) is the conventional method for processing data in low field NMR. However, the ILT is hindered by sensitivity to noise, poor resolution, and high computational requirements that make it difficult to apply in non-laboratory environments. Improving the efficiency of data processing could expand the applications of portable NMR and enhance the quality of information gained from correlation experiments. The MPM fits in a broad category of filter diagonalization methods for digital signal analysis, and was developed for use in radar, antenna, and acoustics technologies. The success of the MPM in other areas of signal processing makes its application to low field NMR promising.

The latter half of this dissertation describes some applications of portable NMR by coupling hardware innovations with a creative data processing strategy. First, a hospital-based measurement of blood plasma water content is developed. Next, factory-based analysis of rheological properties is presented. Finally, the use of portable high-field NMR is established for metabolomic-type assays in agricultural and environmental studies.

TABLE OF CONTENTS

ABSTRACT.....	ii
ACKNOWLEDGEMENTS.....	vii
1. INTRODUCTION TO THE THEORY OF MAGNETIC RESONANCE.....	1
1.1 Classical Interactions of Nuclei with Electromagnetic Fields.....	1
1.2 Quantum Mechanical Description of Spin Populations	5
1.2.1 A Brief Overview: Quantum Mechanics in a Nutshell	5
1.2.2 Liouville Space	7
1.2.3 Angular Momentum, Magnetic Moments, and Spin.....	8
1.2.4 Density Operator Representation and the Liouville-von Neumann Equation	10
1.2.5 Independent Spin $\frac{1}{2}$ Nuclear Systems	11
1.2.6 Two Coupled Spins.....	13
1.2.7 Thermal Equilibrium.....	14
1.2.8 Rotations and Relaxation: the “Master Equation” for Spin Density.....	15
1.2.9 The Nuclear Spin Hamiltonian	15
1.2.10 Motional Averaging.....	16
1.2.11 The Rotating Frame Transformation.....	17
1.2.12 Electronic Effects: Shielding and Chemical Shift.....	18
1.2.13 Chemical Shielding Tensor and the Zeeman Hamiltonian	19
1.2.14 J Coupling	20
1.2.15 Dipolar Coupling	21
1.2.16 Quadrupolar Coupling	22
1.2.17 rf Excitation Hamiltonian	22
1.2.18 Average Hamiltonian Theory	23
References.....	28
2. NUCLEAR SPIN RELAXATION: FROM FUNDAMENTAL MECHANICS TO PRACTICAL APPLICATION.....	29
2.1 Relaxation Mechanisms	30
2.1.1 Longitudinal Magnetization and T_1	30
2.1.2 Transverse Magnetization and T_2	32

2.1.3 Relationships between T_1 , T_2 , and the Autocorrelation Time, τ_c	34
References.....	38
3. THE MATRIX PENCIL AS A TUNABLE FILTER.....	39
Abstract.....	39
3.1 Introduction	40
3.2 Theory	42
3.3 Experimental	44
3.4 Results and Discussion.....	45
3.5 Conclusion.....	53
Acknowledgements.....	53
References.....	54
4. DATA PROCESSING IN NMR RELAXOMETRY USING THE MATRIX PENCIL.....	56
Abstract.....	56
4.1 Introduction	56
4.2 Theory	58
4.2.1 The Inverse Laplace Transform	58
4.2.2 The Matrix Pencil	59
4.2.3 MPM Implementation.....	62
4.2.4 Error Analysis.....	64
4.3 Experimental	65
4.4 Results and Discussion.....	66
4.5 Conclusion.....	79
Acknowledgements.....	81
References.....	84
5. ESTIMATES OF BLOOD PLASMA WATER CONTENT USING PORTABLE NMR RELAXOMETRY.....	88
Abstract.....	88
5.1 Introduction.....	89
5.2 Methods	94
5.2.1 Plasma Standards	94

5.2.2 Standard PWC and Na ⁺ Concentration Measurements	94
5.2.3 NMR Testing	95
5.3 Results.....	96
5.3.1 T ₂ and T ₁ Analysis	96
5.3.2 T ₂ and T ₁ Correlation to PWC	100
5.3.3 PWC Model Testing	106
5.3.4 Electrolyte Test Correction	107
5.4 Discussion.....	110
5.5 Conclusion	111
5.6 Acknowledgements.....	112
References.....	115
6. REAL-TIME SENSOR FOR IN-LINE ANALYSIS OF MATERIAL RHEOLOGY.....	119
6.1 Introduction	119
6.2 Methods and Results	121
6.3 Discussion and Future Work	129
References.....	131
7. PORTABLE HIGH RESOLUTION NMR FOR AGRICULTURAL AND ENVIRONMENTAL PURPOSES.....	132
7.1 Field-based Agricultural Plant Screening for Citrus Greening Disease	132
7.2 Tracking Wildfire Forest Recovery through Terpene Analysis of Pine Resin	133
7.3 Multiple Quantum Coherence Experiments: Detection of J-Coupling at Low Fields.....	134
References.....	136
8. CONCLUSION	137

ACKNOWLEDGEMENTS

The phase of life that I have spent in graduate school has been very much like any other journey: marked with incredible highs as well as struggles and lows, and interspersed with long, flat stretches that have been peaceful and boring in turn. Through it all, I have been uplifted by a remarkable community of people, and I am grateful that our paths have crossed in Davis.

First, I would like to thank my intrepid advisor, Dr. Matt Augustine: you have taught me a tremendous amount about NMR research, radiation damping, building circuits, problem solving, math, surfing, van building, an appreciation for a unique category of humor, and ... the list goes on. To this day, I do not know how I lucked out to find an advisor who also turned out to be a genuine friend in life. The fact that I have loved the day-to-day existence in grad school while embracing a bold and open-minded approach to scientific research is something that I credit to joining your lab.

I also owe a great deal of thanks to everyone else who has been a mentor to me during my PhD at Davis. Thank you, Dr. Dave Britt, for teaching me about spin physics as well as sailing. And thank you, Dr. Alexei Stuchebrukhov, for the thought-provoking discussions about topics ranging from time-dependent quantum mechanics to the thermodynamics of phase changes in extreme environments. I owe a great deal to Dr. Mike McCarthy, for acting as a mentor and guide. I would like to thank Dr. Kristie Koski, for numerous enlightening quarters of being your TA and many fun times with quantum mechanics, as well as invaluable career advice. All of you have been role models in some way, and I am grateful for your influence on me as a scientist.

Finally, no success in a lab is possible without the rest of the team working there. Special thanks to Dan Gruber, Tim Newman, Josh Steele, Michele Martin, Gerry Ochoa, Tricia Wong, Julia Kerr, Vanessa Lee, Matthew Parziale, Sam Martinez, Brandon Cutler, and Javier Aztiazarain. Words will not do justice

to describe the conversations, experiences, and camaraderie we have shared, but I am grateful for it all the same.

1. INTRODUCTION TO THE THEORY OF MAGNETIC RESONANCE

Equipped with his five senses, man explores the universe around him and calls the adventure Science.

– Edwin Powell Hubble, 1889 – 1953

The study of magnetic resonance arises naturally from the quantum mechanical property of ‘spin,’ a phenomenon that remains as mysterious as it is fundamental to the order of the world as we know it. As such, any systematic discussion of magnetic resonance must include a rigorous treatment of quantum mechanics, which will follow shortly. However, since the quantities that we measure holistically relate to the behavior of large collections of spins, it is equally relevant to develop a classical treatment. Of the two, this approach is perhaps the more physically intuitive, and is beneficial for providing a framework of relations and formulae from which to build a discussion of magnetic resonance. Ultimately, as mandated by the Correspondence Principle, there must be a bridge between the two approaches. Although a perfect unification is still lacking, the theoretical foundations discussed here will reflect both classical and quantum mechanics and attempt to highlight a necessary feature of the two approaches, which is their complementarity.

1.1 Classical Interactions of Nuclei with Electromagnetic Fields

Unlike electrons, atomic nuclei experience minimal interactions with their physical environments. Nevertheless, nuclei with nonzero spin are highly sensitive to magnetic fields. As such, a collection of matter can be seen as a dynamic spin system in the (n,P,V) microcanonical ensemble that undergoes

evolution toward thermal equilibrium via the process of relaxation. The achievement of thermal equilibrium can be characterized by parallel or antiparallel alignment of the nuclear spins with an external magnetic field, \vec{B} , as shown in Fig. 1.1.

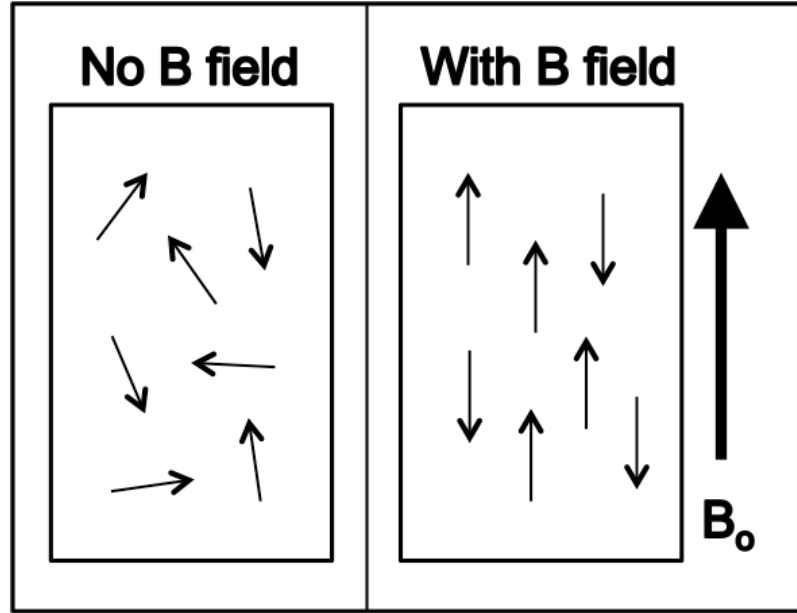


Figure 1.1. A depiction of nuclear spins randomly aligned without an external \vec{B} field (left), and aligned parallel and antiparallel with \vec{B}_0 , which is the z component of \vec{B} (right).

The equations of motion that describe this process are known as the Bloch equations, which can be written in terms of a single magnetic dipole, $\vec{\mu}$, or the bulk magnetism, \vec{M} , which is the summation over all values of $\vec{\mu}$ in a system, as

$$\frac{\partial \vec{M}}{\partial t} = \gamma \vec{M} \times \vec{B}. \quad (1.1)$$

When $B = B_0 \hat{z}$, and relaxation terms are included, this expression becomes

$$\frac{\partial \vec{M}}{\partial t} = \gamma \vec{M} \times B_0 \hat{z} - \frac{M_x x + M_y y}{T_2} - \frac{(M_z - M_0) \hat{z}}{T_1}. \quad (1.2)$$

The presence of linear gradients in the magnetic field for a given spatial dimension n , $G_n(t) = \left. \frac{dB_0}{dn} \right|_{n=0}$,

causes the expression for \vec{B} to be modified to $B = (B_0 + G_x(t)x + G_y(t)y + G_z(t)z)\hat{z}$.

By probing matter with electromagnetic radiation, a great deal of chemically specific information can be learned. The energies associated with nuclear magnetic resonance (NMR) are much less than the typical thermal energy that is available to molecules; this is because the Zeeman splitting of spin energy levels that occur is in the radio frequency (rf) range.

In general, there are three main experimental methods that incorporate NMR: spectroscopy, relaxometry, and imaging. NMR spectroscopy refers to high field experiments that utilize Fourier transforms to analyze chemical shifts and J couplings of functional groups for structure determination. On the other hand, NMR relaxometry typically involves low field, permanent magnets with lower resolution, and signals are typically analyzed in the time domain. The relaxation properties of a material depend on dynamic processes such as chemical exchange, inter- and intramolecular interactions, diffusion, flow, and Brownian motion that results in molecular tumbling. Imaging involves the use of magnetic field gradients in at least two dimensions to create spatially resolved graphs of proton density and relaxation rates.

Broadly speaking, the signal recorded [1] in an experiment is

$$S(t) = M \left(\frac{\gamma}{2\pi} \int_0^t G_x(t') dt', \frac{\gamma}{2\pi} \int_0^t G_y(t') dt', \frac{\gamma}{2\pi} \int_0^t G_z(t') dt' \right) = M(k_x, k_y, k_z). \quad (1.3)$$

When placed in an external magnetic field, the energy levels of nuclei with $I \neq 0$ split in an effect called Zeeman splitting. Application of rf pulses drives transitions between these spin-related energy levels, and the decay back to thermal equilibrium can be observed in a traditional way via spectroscopy and imaging (i.e., by Fourier transforming the time domain signals to analyze frequency spectra). However, the third implementation of NMR that exists in the form of relaxometry involves analysis of time domain signals to characterize samples through the dynamics of their spin relaxation [1]. In particular, NMR

relaxometry is useful for working at low magnetic fields, where signals are weaker and have decreased resolution in comparison to traditional, high field NMR. Low field NMR setups can be advantageous, as they are typically smaller and more portable than their high field counterparts, due to the use of permanent, rather than superconducting, magnets.

Recent technological advancements have made portable NMR economically and practically feasible. The ease with which it can be customized to address scientific and clinical problems makes portable NMR an extremely attractive technique. Nevertheless, there are consequences to working at the low magnetic fields common to portable NMR spectroscopy. Specifically, since there is insufficient resolution to measure chemical shifts and J-couplings in the frequency domain, the transverse and longitudinal relaxation rate constants (T_2 and T_1) are the relaxometry parameters typically measured at low field [2].

NMR relaxometry observes spin relaxation, which occurs predominantly through dipolar coupling brought about by locally fluctuating magnetic fields [1,3]. The chief effector of these field fluctuations is Brownian movement of molecules [4]. In addition to water, other molecules in a sample interact with water via the formation of hydrogen bonds. In turn, these interactions affect the spin relaxation properties of water by altering the rotational correlation time of the bound-state water, which is inversely proportional to T_2 and (to a point) T_1 , and is defined as the time required for a molecule or molecular complex to rotate by one radian. Since the correlation time increases with an increase in molecular size, as well as with an increase in viscosity or decrease in temperature as described by the generalized Stokes-Einstein-Debye equation [4,5], it is expected that samples with lower water content will have faster relaxation times.

Moreover, rapid proton exchange occurs between free water and bound water in many materials. Since the exchange rate for these protons is fast in comparison to T_2 and T_1 , with respective timescales of 10^{-9} s for exchange versus $10^{-3} - 10^0$ s for spin relaxation, this phenomenon results in a weighted averaging of T_2 and T_1 values for bound and unbound water.

1.2 Quantum Mechanical Description of Spin Populations

The systems observed in NMR experiments are large collections of approximately 10^{23} spins or more; as such, their behavior must be described statistically. In addition, there are shortcomings to the classical picture of NMR that motivate a more precise quantum mechanical description. Namely, the Bloch equations are valid only for collections of non-interacting spins. Moreover, individual spins do not have associated T_1 or T_2 values. Therefore, a statistical description of nuclear spin relaxation must be developed on the basis of interactions between spins, including nuclear dipolar and J couplings, chemical exchange, and electron-nuclear interactions such as shielding, dipolar coupling, and J coupling.

1.2.1 A Brief Overview: *Quantum Mechanics in a Nutshell*

Analogous to the classical trajectory, which describes the succession in time of the classical state of a particle, a wavefunction $\Psi(\vec{r}, t)$ completely describes the quantum state of a particle. The square modulus of the wavefunction is interpreted as a probability density of the presence of the particle in space, as

$$dP(\vec{r}, t) = C \left| \Psi(\vec{r}, t) \right|^2 d^3r \quad (1.4)$$

where C is the square of the normalization constant. Wavefunction normalization is a requirement to scale the total probability of existence to 1, such that $\int dP(\vec{r}, t) = 1$. Each wavefunction eigenstate can be treated as an element in a linear vector space, written as a ket $|\Psi(\vec{r})\rangle$ in Dirac notation. The elements of the dual vector space are indicated by the complex conjugate bra $\langle\Theta|$. The scalar product $\langle\Theta|\Psi\rangle$ is used to generate a Hilbert space, which is a complete vector space occupied by all the available eigenstates of a system.

The superposition principle states that a wavefunction, $|\Psi\rangle$, can be expressed as a linear combination of eigenvectors in a basis set, as given by

$$|\Psi\rangle = \sum_{i=1}^n c_i |\varphi_i\rangle. \quad (1.5)$$

A basis is an N-dimensional vector space that is constituted by linearly independent eigenvectors, where linear independence implies that no element in the set can be written as a linear combination of the other elements in the set. It is an equivalent statement that the only solution to the equation

$$\sum_i c_i |\varphi_i\rangle = 0 \quad (1.6)$$

is $c_i \equiv 0$ for all i . In general, quantum mechanics deals with orthonormal bases:

$$\langle \psi_i | \psi_j \rangle = \begin{cases} 1 & i = j \\ 0 & i \neq j \end{cases}. \quad (1.7)$$

Most quantum mechanical operators, \hat{O} , are linear such that $\hat{O}(\lambda_1 |\varphi_1\rangle + \lambda_2 |\varphi_2\rangle) = \lambda_1 \hat{O} |\varphi_1\rangle + \lambda_2 \hat{O} |\varphi_2\rangle$ for λ_1 and λ_2 that are scalars.

It is useful to consider the matrix representations of wavefunctions and operators. For example, when a ket, $|\Psi\rangle$, is written as a linear combination of basis elements, $\sum_{i=1}^n c_i |\varphi_i\rangle$, it is natural to construct a column vector from a ket as

$$|\Psi\rangle = \vec{\Psi} = \begin{pmatrix} c_1 \\ c_2 \\ \vdots \\ c_n \end{pmatrix}. \quad (1.8)$$

Likewise, the complex conjugate bra corresponds to a row vector as $\langle \Psi | = \overline{\Psi}^\dagger = (c_1^\dagger \quad c_2^\dagger \quad \cdots \quad c_n^\dagger)$.

Operators can also be written as matrices, for instance when $\hat{O}|\psi\rangle = \lambda|\psi\rangle$ where λ represents the eigenvalues of \hat{O} , which is an $n \times n$ matrix with elements $O_{ij} = \langle \psi_i | \hat{O} | \psi_j \rangle$. Since the trace of a matrix is invariant in a change of basis, a useful metric is the trace of the operator, which corresponds to the sum of the diagonal eigenvalues $Tr(\hat{O}) = \sum_i O_{ii} = \sum_i \lambda_i$.

The Schrödinger equation describes the evolution of a wavefunction in time as

$$\frac{\partial}{\partial t} |\Psi(t)\rangle = -i\hat{H}(t) |\Psi(t)\rangle \quad (1.9)$$

where $\hat{H}(t)$ is the Hamiltonian, or the total energy operator.

1.2.2 Liouville Space

To deal with interactions between particles or spins, it quickly becomes clear that it is helpful to move from an N -dimensional Hilbert space to an N^2 -dimensional vector space called Liouville space. Operators that are defined in Hilbert space are elements of Liouville space, and, unlike in Hilbert space, the product of two elements of Liouville space is defined as $Tr[\hat{A}^\dagger \hat{B}] = (\hat{A} | \hat{B})$. It is important to remember that, in general, $\hat{A}\hat{B} \neq \hat{B}\hat{A}$.

Superoperators are operators that work on elements of Liouville space, indicated by a double hat, and are defined through the commutator $\hat{\hat{A}}|\hat{B}\rangle \equiv [[\hat{A}, \hat{B}]] = |\hat{A}\hat{B} - \hat{B}\hat{A}\rangle$ [6].

1.2.3 Angular Momentum, Magnetic Moments, and Spin

The deeply interconnected natures of angular momentum, the magnetic moment, and spin are demonstrated in the linear relationship between their corresponding quantum mechanical operators.

$$\hat{\mu}_{x,y,z} = \gamma \hat{L}_{x,y,z} = \gamma \hbar \hat{I}_{x,y,z} \quad (1.10)$$

where $\hat{\mu}$ represents the magnetic moment, \hat{L} is orbital angular momentum, and \hat{I} is the nuclear spin operator. Here, \hat{I} is analogous to the more general spin angular momentum operator denoted as \hat{S} . It is worth noting that the total angular momentum is $\hat{J} = \hat{L} + \hat{S}$. The commutators of the x, y, and z components of each form of angular momentum can be described most simply by the rules for Levi-Civita tensor notation. For example, $[\hat{I}_i, \hat{I}_j] = \varepsilon_{ijk} \hat{I}_k$, where $\varepsilon = 1$ for cyclic $i, j, k = x, y, z$ and $\varepsilon = -1$ for anticyclic indexing. This relationship is also true for the Cartesian components of \hat{J} , \hat{L} , and \hat{S} .

An expression for γ , the gyromagnetic ratio, is developed naturally from a classical derivation of the magnetic moment that arises from current flowing through a loop as $\vec{\mu} = I\vec{A}$. Here, the current is the charge per unit time, $I = \frac{q}{t}$, and the area as assumed for a symmetric or round particle or orbital is circular

as $A = \pi r^2$. At this time, if we note that in general, velocity is the distance of displacement per time as

$v = \frac{x}{t}$, we can rearrange to express time as $t = \frac{x}{v} = \frac{2\pi r}{v}$ for motion on a circular path. Thus, by

substitution, our expression for magnetic moment becomes $\vec{\mu} = I\vec{A} = \frac{qrv}{2} = \frac{e(\vec{r} \times \vec{v})}{2} = \frac{e\vec{L}}{2m}$ where we

have taken advantage of the fact that the cross product $\vec{r} \times \vec{v} = rv \sin \theta = rv$ for $\theta = 90^\circ$, and this cross product is equivalent to the orbital angular momentum scaled by the mass, m . Additionally, we have used the fact that the charge here is the charge of the electron, e . As such, the gyromagnetic ratio of the so-

called Bohr magneton is $\gamma_B = \frac{e}{2m_e}$. To make this expression suitable for other nuclei, this expression is

modified by the scaling nuclear g-factor as $\gamma_N = \frac{e g_N}{2m_N}$ to account for the subtle complexities that slightly

alter the charge to mass ratios of each respective nucleus beyond the other terms in this expression.

In a magnetic field, B_0 , particles with a magnetic dipole moment align parallel or antiparallel and precess around the direction of the field – much like the wobble of a compass needle – with a frequency termed the Larmor frequency, $\omega_L \equiv \gamma B_0$.

If we shift back to a quantum mechanical viewpoint, we will find that the eigenvalues for a spin $\frac{1}{2}$ particle are obtained by operating with \hat{I}_z on the up and down spin states (denoted + or α and – or β) as $\hat{I}_z|+\rangle = +\frac{1}{2}|+\rangle$ and $\hat{I}_z|-\rangle = -\frac{1}{2}|-\rangle$. The Pauli matrices are used to represent the x, y, and z spin components in the $\{|+\rangle, |-\rangle\}$ basis as

$$\hat{I}_x = \frac{1}{2} \begin{pmatrix} 0 & 1 \\ 1 & 0 \end{pmatrix}, \hat{I}_y = \frac{1}{2} \begin{pmatrix} 0 & -i \\ i & 0 \end{pmatrix}, \text{ and } \hat{I}_z = \frac{1}{2} \begin{pmatrix} 1 & 0 \\ 0 & -1 \end{pmatrix}. \quad (1.11)$$

The next objective is to consider how to find an appropriate form of a wavefunction, $|\Psi(t)\rangle$, to describe a nuclear system in a magnetic field, which we will initially assume is uniform in strength. The most simplistic procedure is to first find $\hat{H}(t)$, then to apply the Schrödinger equation in Eq. 1.9 to solve for $|\Psi(t)\rangle$. From this point, other quantities of interest may be calculated directly, such as the average components of the magnetic moment $\langle \hat{\mu}_x \rangle$, $\langle \hat{\mu}_y \rangle$, and $\langle \hat{\mu}_z \rangle$, or their corresponding macroscopic quantities M_x , M_y , and M_z . Unfortunately, this approach is rapidly met with pitfalls when extended to systems containing many nuclear spins.

1.2.4 Density Operator Representation and the Liouville-von Neumann Equation

Realistic, measurable systems typically encompass a minimum of several moles of spins, which means that we must deal with more than 10^{23} spins at any given time. Immediately, this causes the Schrödinger equation approach to become intractable, as the expression for the pure state $|\Psi(t)\rangle$ will involve a summation over more than 10^{23} components as

$$|\Psi(t)\rangle = \sum_{i=1}^{n \text{ spins}} c_i(t) |u_i\rangle \quad (1.12)$$

where the set $\{|u_i\rangle\}$ forms an orthonormal basis.

To move forward in this case, we will develop the idea of a spin density operator, which can be applied to our large system of spins in a pure state or a statistical mixture. Let us define the density operator as

$$\hat{\sigma}(t) = |\Psi(t)\rangle\langle\Psi(t)| \quad (1.13)$$

while also noting a key property of this operator in terms of how it can be used to predict the expectation value of another observable, which we will denote here as \hat{A} :

$$\langle\hat{A}\rangle(t) = \sum_{i,j} \langle u_j | \hat{\sigma}(t) | u_i \rangle \langle u_i | \hat{A} | u_j \rangle = \text{Tr} \{ \hat{\sigma}(t) \hat{A} \}. \quad (1.14)$$

Next, by applying the Schrödinger equation, it can be shown that the time evolution of the density operator is

$$\begin{aligned}
\frac{\partial}{\partial t} \hat{\sigma}(t) &= \frac{\partial}{\partial t} [|\Psi(t)\rangle\langle\Psi(t)|] \\
&= -i[\hat{H}, |\Psi(t)\rangle\langle\Psi(t)|] \\
&= -i[\hat{H}, \hat{\sigma}] \\
&= -i\hat{H}\hat{\sigma}.
\end{aligned}$$

This yields the familiar result that is known as the Liouville-von Neumann equation

$$\frac{\partial}{\partial t} \hat{\sigma}(t) = -i[\hat{H}, \hat{\sigma}] \text{ or } \frac{\partial}{\partial t} |\hat{\sigma}\rangle = -i\hat{H}|\hat{\sigma}\rangle. \quad (1.15)$$

Naturally, we must consider the case when our system no longer characterizes a pure state, but rather contains a statistical mixture of states, Ψ_n . If the probabilities corresponding to each state are denoted p_n , the system's density operator becomes $\hat{\sigma} = \sum_n p_n \hat{\sigma}_n$. Additionally, the ensemble average of the observable, \hat{A} , is

$$\overline{\langle \hat{A} \rangle} = \text{Tr} \{ \hat{\sigma} \hat{A} \}. \quad (1.16)$$

1.2.5 Independent Spin $\frac{1}{2}$ Nuclear Systems

Let us step back briefly and recapitulate the most important points that have been developed above. First, we decided that the most convenient basis set to use for a system of independent spins is the set of available eigenstates of \hat{H}_0 . The simplest set of eigenkets, $\{|+\rangle, |-\rangle\}$, corresponds to spin $\frac{1}{2}$ nuclei. Next, we developed the construct of spin density through a density operator to replace the idea of a wavefunction for a large, statistical system. Like a wavefunction, spin density can be written in matrix form in terms of the time dependent coefficients of each substate, which are here $|+\rangle$ or $|-\rangle$, as

$$\underline{\sigma} = \begin{pmatrix} \overline{|c_+|^2} & \overline{c_+ c_-^*} \\ \overline{c_+^* c_-} & \overline{|c_-|^2} \end{pmatrix}. \quad (1.17)$$

If we relabel this matrix in short form as

$$\begin{array}{cc} & |+\rangle & |-\rangle \\ |+\rangle & \begin{pmatrix} Z & T \end{pmatrix} \\ |-\rangle & \begin{pmatrix} T & Z \end{pmatrix} \end{array} \quad (1.18)$$

we can conveniently express the longitudinal magnetization as “Z” and the transverse magnetization, or spin coherence, as “T”. For a single spin, we can write this in matrix form as

$$\underline{\sigma} = Z_{11} \begin{pmatrix} 1 & 0 \\ 0 & 0 \end{pmatrix} + T_+ \begin{pmatrix} 0 & 1 \\ 0 & 0 \end{pmatrix} + T_- \begin{pmatrix} 0 & 0 \\ 1 & 0 \end{pmatrix} + Z_{22} \begin{pmatrix} 0 & 0 \\ 0 & 1 \end{pmatrix} \quad (1.19)$$

or, perhaps more conveniently, as

$$\underline{\sigma} = a_1 \begin{pmatrix} 1 & 0 \\ 0 & 1 \end{pmatrix} + a_x \begin{pmatrix} 0 & 1/2 \\ 1/2 & 0 \end{pmatrix} + a_y \begin{pmatrix} 0 & -i/2 \\ i/2 & 0 \end{pmatrix} + a_z \begin{pmatrix} 1/2 & 0 \\ 0 & -1/2 \end{pmatrix}. \quad (1.20)$$

Alternatively, in operator form, σ can be written as a vector in Liouville space (also referred to as coherence space for this purpose) as

$$\hat{\sigma} = \begin{pmatrix} Z_{11} \\ T_+ \\ T_- \\ Z_{22} \end{pmatrix}. \quad (1.21)$$

The so-called “operator” basis set of $\{\hat{E}, \hat{I}_x, \hat{I}_y, \hat{I}_z\}$ can be developed when we consider another operator representation of σ as

$$\hat{\sigma} = a_1 \hat{E} + a_x \hat{I}_x + a_y \hat{I}_y + a_z \hat{I}_z. \quad (1.22)$$

We will see how a product of these operators, or “product operators”, become useful as we press onward to consider a coupled system of two spins next.

1.2.6 Two Coupled Spins

To address the case of two coupled spins, we must modify the basis set in which we are working to reflect the dependence of the overall states available to the system on the manner in which the individual states combine. The new set of available eigenstates of \hat{H}_0 , for spin $\frac{1}{2}$ nuclei, is $\{|++\rangle, |+-\rangle, |-+\rangle, |--\rangle\}$. Likewise, we can adjust the spin density matrix to clearly show the respective populations, P, of each of these states on the diagonal, and the mixtures – or coherences, C – on the off-diagonal:

$$\underline{\sigma} \Rightarrow \begin{array}{c} |++\rangle \\ |+-\rangle \\ |-+\rangle \\ |--\rangle \end{array} \begin{array}{c} |++\rangle \\ |+-\rangle \\ |-+\rangle \\ |--\rangle \end{array} \begin{pmatrix} P_{1,1} & C_{1,2} & C_{1,3} & C_{1,4} \\ C_{2,1} & P_{2,2} & C_{2,3} & C_{2,4} \\ C_{3,1} & C_{3,2} & P_{3,3} & C_{3,4} \\ C_{4,1} & C_{4,2} & C_{4,3} & P_{4,4} \end{pmatrix}. \quad (1.23)$$

Now we can use the product operators to handily write the complete, orthonormal basis set of $2^4 = 16$ total states for this system in four parts as

$$\begin{aligned} & \left\{ \frac{1}{2}\hat{E}, \hat{I}_x, \hat{I}_y, \hat{I}_z, \hat{S}_x, \hat{S}_y, \hat{S}_z; \right. \\ & 2\hat{I}_x\hat{S}_z, 2\hat{I}_y\hat{S}_z, 2\hat{I}_z\hat{S}_x, 2\hat{I}_z\hat{S}_y; \\ & 2\hat{I}_z\hat{S}_z; \\ & \left. 2\hat{I}_x\hat{S}_x, 2\hat{I}_y\hat{S}_y, 2\hat{I}_x\hat{S}_y, 2\hat{I}_y\hat{S}_x \right\} \end{aligned} \quad (1.24)$$

where \hat{I} represents the first spin and \hat{S} represents the second spin. The states in the first group of product operators are in-phase single quantum coherences; in the second group, the anti-phase single quantum

coherences; while the third group corresponds to a longitudinal two-spin order; and the fourth group is made up of the remaining linear combinations of “forbidden” double and zero quantum coherences.

1.2.7 Thermal Equilibrium

Predictably, the remaining logical step is to return to the big picture and generalize these results for a system of n spins. We will find, unsurprisingly, that the spin density matrix in Eq. 1.23 becomes

$$\underline{\sigma} = \begin{pmatrix} P_{1,1} & C_{1,2} & \cdots & C_{1,n} \\ C_{2,1} & P_{2,2} & \ddots & \vdots \\ \vdots & \ddots & \ddots & C_{n-1,n} \\ C_{n,1} & \cdots & C_{n,n-1} & P_{n,n} \end{pmatrix}. \quad (1.25)$$

We can note that the off-diagonal coherences average to zero at thermal equilibrium (i.e., there is no transverse magnetization). To find the probability of occupying the various states available to a system, the Boltzmann distribution can be applied in the following manner:

$$\hat{\sigma}_{\text{Boltzmann}} = \frac{1}{Z} e^{-\hbar\hat{H}_0/kT} \quad (1.26)$$

where the partition function is defined as $Z = \text{Tr} \left\{ e^{-\hbar\hat{H}_0/kT} \right\}$ and $\hat{H}_0 = \frac{E}{\hbar}$. It is generally reasonable to use

the high temperature approximation by taking the first two terms in the Taylor expansion of the exponentials to simplify the expression for the Boltzmann equilibrium density matrix as

$$\hat{\sigma}_{\text{Boltzmann}} \simeq \frac{1}{2} \left(E - \frac{\hbar}{kT} \hat{H}_0 \right) \quad (1.27)$$

for spin $\frac{1}{2}$ particles.

1.2.8 Rotations and Relaxation: the “Master Equation” for Spin Density

The end goal of these gymnastics is to find an equation that can adequately describe and predict the behavior of a realistic spin system to connect with signals measured in laboratory experiments. This coupling of theory and experiment is the essence of physical chemistry. As such, we must add a final modification to the Liouville-von Neumann equation (Eq. 1.15) to describe spin relaxation, as well as the rotations generated by the Hamiltonian. Ultimately, we seek an equation of the form

$$\frac{\partial}{\partial t}|\hat{\sigma}\rangle = -i\hat{H}|\hat{\sigma}\rangle - \hat{\Gamma}(|\hat{\sigma}\rangle - |\hat{\sigma}_{Boltzmann}\rangle) \quad (1.28)$$

where $\hat{\Gamma}$ is the relaxation superoperator [6,7]. Note the similarities in this equation to the Bloch equations, which also contain a rotation part – in the cross product – as well as relaxation terms. At this point, it also becomes clear that we must develop strategies to find the Hamiltonian if we wish to make any reasonable progress with applying this equation in a practical sense.

1.2.9 The Nuclear Spin Hamiltonian

In order to validate and predict magnetic resonance experiments, it is helpful to calculate the Hamiltonians of spin systems. Since these Hamiltonians are generally time-dependent, the nature of this problem is inherently complex. Therefore, some strategic techniques to simplify or approximate the time dependent terms must be implemented.

In magnetic resonance, it is common to transform into the rotating frame to simplify calculations or derivations. In essence, the transformation into a rotating reference frame fixes the axes with respect to the precession about the z-axis at the Larmor frequency of the spins. This approach proves useful for calculating Hamiltonians as well; in fact, one of the most common approximation techniques is based on this transformation. Once in the rotating frame, we can simply truncate the Hamiltonian to only include the

time-independent, or secular, terms. Not surprisingly, this technique is called the Secular Approximation (or the Rotating Wave Approximation).

In general, the energy describing the interaction between a magnetic dipole, $\vec{\mu}$, and an external magnetic field, \vec{B} , is a dot product of the two vector quantities, $E = -\vec{\mu} \cdot \vec{B} = -|\mu|B \cos \theta$. However, there are other interactions that contribute to the complete expression for energy, and as such, the total Hamiltonian operator that yields this energy is a sum of terms that describe each interaction. For example, if we assert that $\hat{H} = \hat{H}_1 + \hat{H}_2 + \hat{H}_3 + \dots$, then we could ascribe the first term to the interaction of the spin in question with B_0 , the second term to interactions with the magnetic dipole fields of surrounding nuclei, the third term to electron couplings, etc. If we think of a nuclear spin as a magnet, there is a term in the Hamiltonian that describes the orientation dependence of the spin with respect to an external electromagnetic field. This so-called “Zeeman” term corresponds to the classical dot product energy shown above as $\hat{H}_{ext} = -\vec{\mu} \cdot \vec{B} = -\gamma \hbar \vec{I} \cdot \vec{B}$. In general, we can use \hat{H}_{ext} to describe the static field and the rf field, and \hat{H}_{int} to describe internal interactions such as chemical shift, J-couplings (through bond), dipole-dipole couplings (through space), and quadrupolar couplings.

1.2.10 Motional Averaging

At this point, if we take molecular motion into account, we can simplify the possible time-dependence of this term with motional averaging. This arises from a combination of translation, rotation, and internal molecular motions such as bond axis rotations. Note that these effects are reasonable to assume for liquids and gases, where molecules undergo relatively free movement, but not for solids, due to the fixed molecular positions in a crystal lattice [8]. The assumption of motional averaging of various molecular orientations over time can be used to write the secular Hamiltonian as

$$\overline{\hat{H}_{\text{int}}^0} = \frac{1}{\tau} \int_0^{\tau} \hat{H}_{\text{int}}^0(\Theta(t)) dt \quad (1.29)$$

where $\Theta(t)$ represents a molecular orientation. Invoking the properties of ergodicity, we can rewrite this as an integral over a probability density, $p(\Theta)$, to eliminate the time dependence and equivalently state

$$\overline{\hat{H}_{\text{int}}^0} = \int \hat{H}_{\text{int}}^0(\Theta) p(\Theta) d\Theta$$

or, with normalization,

$$\overline{\hat{H}_{\text{int}}^0} = \frac{1}{N} \int \hat{H}_{\text{int}}^0(\Theta) d\Theta. \quad (1.30)$$

1.2.11 The Rotating Frame Transformation

As one might guess, the straightforward representation in Eq. 1.30 is oftentimes too simplified to adequately describe complex systems. Instead, the next reasonable approach is to analyze time variations as perturbations that show up in the transverse plane as

$$\hat{H}(t) = -\omega_0 \hat{I}_z - \omega_1 \left(\hat{I}_x \cos \omega t - \hat{I}_y \sin \omega t \right) \quad (1.31)$$

for an rf pulse with frequency ω and amplitude ω_1 , applied perpendicular to the DC field \vec{B}_0 that defines ω_0 and the z direction. Note that this form presumes that crossed rf coils are used to provide the circularly polarized rf field.

However, managing multiple oscillatory components in the Hamiltonian can become unwieldy. It now becomes advantageous to describe a frame transformation from the laboratory to the rotating frame, which is a common tactic to simplify terms. We define the rotating frame Hamiltonian, \hat{H}' , as

$$\hat{H}'_{rot} = e^{-i\omega t \hat{I}_z} \hat{H} = e^{-i\omega t \hat{I}_z} \hat{H}_{lab} e^{i\omega t \hat{I}_z}. \quad (1.32)$$

The benefit of this is that we can drop the sines and cosines in Eq. 1.31 and transform into time independent terms, yielding a simpler, effective external Hamiltonian as

$$\hat{H}_{eff} = -(\omega_0 - \omega) \hat{I}_z - \omega_1 \hat{I}_x \quad (1.33)$$

in the rotating frame. To be clear, this Hamiltonian is being developed to describe the external interactions with the static and rf fields, defined above as \hat{H}_{ext} . It is worth noting that the dominant component in the Hamiltonian is the interaction with the static field.

1.2.12 Electronic Effects: Shielding and Chemical Shift

The magnetic field that is experienced by an atomic nucleus is modified by its surrounding electrons. As the electrons, which are effectively moving charges, move around a nucleus – or a network of nuclei in a molecule – they generate a smaller magnetic field in a direction opposing the external magnetic field. This effect is called shielding, and can be described by the shielding constant, σ . The effective magnetic field becomes

$$B_{eff} = B_0(1 - \sigma). \quad (1.34)$$

The effect can also be generalized to describe the bulk magnetic susceptibility, χ , of a material as

$$B_{nuc} = B_0(1 - \chi) \quad (1.35)$$

where B_{nuc} is the magnetic field “felt” at the nuclei within the material.

In practice, one of the most useful observations that arises from the phenomenon of shielding is chemical shift. As the electron cloud density varies locally within a molecule, due in part to the presence

of different functional groups, distinct nuclei experience varying degrees of shielding. This leads them to experience slightly different magnitudes of B_{eff} , which causes them to precess at frequencies that vary slightly depending on the local chemical environment. When measured spectroscopically, this effect manifests as peaks that are shifted in frequency depending on their molecular environment. Thus, the name “chemical shift” is an intuitive designation.

1.2.13 Chemical Shielding Tensor and the Zeeman Hamiltonian

The Zeeman Hamiltonian,

$$\hat{H}_{zeeman} = -\gamma \vec{I} \cdot \vec{B}, \quad (1.36)$$

which describes the interaction energy between a magnetic moment and an external magnetic field, can now be modified to include the effects of chemical shielding as a 3×3 tensor, $\underline{\sigma}$ (not to be confused with the spin density), in the following way:

$$\hat{H}_{zeeman} = -\gamma \vec{I} \cdot (\underline{1} - \underline{\sigma}) \cdot \vec{B}. \quad (1.37)$$

It is necessary to use a tensor to describe the orientation dependence of electron shielding in a molecule, i.e., anisotropy. This effect is particularly noticeable in solids and crystal lattices. A sum of three terms can be used to define the shielding tensor as

$$\underline{\sigma} = \begin{pmatrix} \sigma_{xx} & \sigma_{xy} & \sigma_{xz} \\ \sigma_{yx} & \sigma_{yy} & \sigma_{yz} \\ \sigma_{zx} & \sigma_{zy} & \sigma_{zz} \end{pmatrix} = \sigma_{isotropic} \begin{pmatrix} 1 & 0 & 0 \\ 0 & 1 & 0 \\ 0 & 0 & 1 \end{pmatrix} + \underline{\sigma}^{(1)} + \underline{\sigma}^{(2)}. \quad (1.38)$$

Here, the first and second order terms are time-varying, and $\underline{\sigma}^{(2)}$ is the chief effector of a relaxation mechanism called chemical shift anisotropy, or CSA. It is worth noting that most terms in the Hamiltonian

also give rise to relaxation mechanisms, as they involve splitting of energy levels that can lead to transfers or exchanges of energy following rf excitation.

In liquids, rapid molecular tumbling leads to motional averaging of anisotropic components, which simplifies the shielding tensor and allows it to collapse to a single, isotropic value as

$$\sigma_{isotropic} = Tr(\underline{\sigma} / 3). \quad (1.39)$$

Therefore, for an isotropic sample placed in a homogeneous magnetic field along z, the simplest Zeeman Hamiltonian is

$$\hat{H}_{zeeman} = -\gamma(1-\sigma)\hat{I}_z\hat{B}_0. \quad (1.40)$$

1.2.14 J Coupling

At close range, with distances on the order of a bond length, it is possible for nuclear spins to interact with each other directly as well as with their surrounding electrons. These “through-bond” interactions are isotropic, unlike the more general “through-space” dipolar interactions, and are described by scalar “J” values. Note that J coupling can also be called the Fermi contact interaction, spin-spin coupling, or scalar coupling. The J coupling Hamiltonian is

$$\hat{H}_J = 2\pi\vec{J}\vec{I} \cdot \vec{S} \quad (1.41)$$

if the two interacting spins are denoted \vec{I} and \vec{S} . In most cases, J is independent of molecular orientation, and therefore does not typically contribute substantially to relaxation. The exceptions to this are cases when the J value appears to change over time, namely when (1) one of the spins takes part in chemical exchange, or (2) when the T_1 of one of the spins is much less than $1/J$. Relaxation in these cases is respectively called scalar relaxation of the first and second kind [7].

1.2.15 Dipolar Coupling

As we have already discussed, any nucleus with nonzero spin behaves like a miniature magnetic dipole. The dipolar magnetic field generated by a nucleus in the xy plane can be described by a formula that is dependent on both radial distance and angular inclination, r and θ , from the nucleus as

$$B_{\mu x} = \left(\frac{\mu_0}{4\pi}\right)\left(\frac{\mu}{r^3}\right)3\sin\theta\cos\theta \quad (1.42)$$

$$B_{\mu y} = 0 \quad (1.43)$$

$$B_{\mu z} = \left(\frac{\mu_0}{4\pi}\right)\left(\frac{\mu}{r^3}\right)(3\cos^2\theta - 1) \quad (1.44)$$

where μ_0 is the permeability of free space. However, any realistic system is populated with many spins, and therefore, many miniature dipolar fields. Since these fields drop off very quickly, due to their $\frac{1}{r^3}$ dependence, the dipolar coupling effect is predominantly intramolecular. By nature, this coupling is time-dependent. As a molecule tumbles within an external magnetic field, B_0 , its nuclear spins remain in alignment with B_0 even as the molecule continually re-orient itself. The dipolar Hamiltonian is

$$\hat{H}_{dipolar} = -\frac{\mu_0\hbar\gamma_I\gamma_S}{4\pi r_{IS}^3}\left(\vec{\hat{I}}\cdot\vec{\hat{S}} - \frac{3}{r_{IS}^2}\left(\vec{\hat{I}}\cdot\vec{r}_{IS}\right)\left(\vec{\hat{S}}\cdot\vec{r}_{IS}\right)\right) \quad (1.45)$$

where \vec{r}_{IS} is the internuclear distance. A secular approximation can somewhat simplify this expression by removing the dependence on \vec{r}_{IS} as

$$\hat{H}_{dipolar} = d\left(3\hat{I}_z\hat{S}_z - \vec{\hat{I}}\cdot\vec{\hat{S}}\right). \quad (1.46)$$

Here, the dipolar coupling constant is $d = -\frac{\mu_0 \hbar \gamma_I \gamma_S}{4\pi r_{IS}^3} (3 \cos^2 \Theta_{IS} - 1)$ and Θ_{IS} is the angle between B_0

and the internuclear vector. While all of these constants can be rather unwieldy, we find a happy simplification in the case of time-averaged isotropic tumbling that the dipolar Hamiltonian goes to zero. Nonetheless, before we get too excited about this approximation and decide to make widespread use of it, we should note that the temporal variations of $\hat{H}_{dipolar}$ are often the foremost cause of both T_1 and T_2 relaxation, which will be discussed in the next chapter.

1.2.16 Quadrupolar Coupling

It is important to mention the fact that many nuclei have spin values greater than $1/2$. These nuclei possess nonuniform charge distributions that give rise to an electrical quadrupolar moment, which in turn interacts with local gradients in electric field. These dynamic interactions result in energy shifts that alter the resonance frequencies, as described by the quadrupolar coupling Hamiltonian. Within the secular approximation, this Hamiltonian appears to be an interaction of the spin with itself:

$$\hat{H}_Q = \frac{3eQ}{4I(2I-1)\hbar} V_0 \left(3\hat{I}_z^2 - \vec{\hat{I}} \cdot \vec{\hat{I}} \right) \quad (1.47)$$

where V_0 is the orientation-dependent electric field gradient and Q is a quadrupolar coupling constant.

1.2.17 rf Excitation Hamiltonian

When we add an rf pulse at frequency ω_1 to perturb the spin system in an experiment, the term that describes the interaction is

$$\hat{H}_{rf} = -\omega_1 \hat{I}_x \quad (1.48)$$

or, for two distinct types of spins,

$$\hat{H}_{rf} = -\omega_1 \hat{I}_x - \omega_1 \hat{S}_x. \quad (1.49)$$

Overall, we can summarize the total Hamiltonian at this point with each of the contributing terms that have been discussed so far (Zeeman and rf interactions, J coupling, dipolar coupling, quadrupolar) as

$$\begin{aligned} \hat{H} = & -\gamma_I \hat{I} (1 - \underline{\sigma}_I) \hat{B}_0 - \gamma_S \hat{S} (1 - \underline{\sigma}_S) \hat{B}_0 - \omega_1 \hat{I}_x - \omega_1 \hat{S}_x + 2\pi J \left(\vec{\hat{I}} \cdot \vec{\hat{S}} \right) + d \left(3\hat{I}_z \hat{S}_z - \vec{\hat{I}} \cdot \vec{\hat{S}} \right) \\ & + \frac{3eQ}{4I(2I-1)\hbar} V_0 \left(3\hat{I}_z^2 - \vec{\hat{I}} \cdot \vec{\hat{I}} \right). \end{aligned} \quad (1.50)$$

1.2.18 Average Hamiltonian Theory

It would be nice to have a method for evaluating some of the non-secular (or time-dependent) terms of the Hamiltonian [9-14]. Average Hamiltonian Theory (AHT) is one such method. A few other notable techniques are Floquet theory and Van Vleck transformations. To develop the framework of AHT, we must start with the time-dependent Schrodinger Equation (letting $\hbar \rightarrow 1$, shown in Eq. 1.9), which describes the time evolution of a wavefunction. We can relate the wavefunction at time “t” to the initial wavefunction through a time-dependent propagator, U(t), whose time evolution is given by

$$\frac{\partial}{\partial t} U(t) = -iH(t)U(t). \quad (1.51)$$

Next, we must decide how to deal with this propagator. It is clear that if we can solve Eq. 1.51 for H(t), which is the full, time-dependent Hamiltonian of the spin system, we will be able to find a form of U(t). A logical next step might be to use perturbation theory to separate H(t) into time independent and time-dependent terms as

$$H(t) = H_0 + H'(t) \quad (1.52)$$

where $H'(t)$ represents a time-dependent perturbation (i.e., an rf pulse) and H_0 represents the internal, time-independent terms (i.e., chemical shift, dipolar couplings, etc.). Now, we might find it useful to separate the propagator into a product of two terms as well:

$$U(t) = L^\dagger(t)\mathcal{L}(t). \quad (1.53)$$

In this form, $L^\dagger(t)$ represents solely the external perturbing Hamiltonian, while $\mathcal{L}(t)$ represents the summed interaction of the external Hamiltonian with the internal Hamiltonian of the system. Since our goal is to solve for the propagator, it is useful to write $U(t)$ in this form because we know that

$$L^\dagger(t) = e^{-i\int_0^t H'(t')dt'}. \quad (1.54)$$

Now, our goal is to find the appropriate form of $\mathcal{L}(t)$ such that the Schrodinger Equation is satisfied. Once we know this, we will be able to directly calculate what are called “average Hamiltonians” by implementing a Magnus expansion of the propagator. This brilliant mathematical manipulation will yield $\bar{H}^{(n)}$, or the average Hamiltonians, as orders of the expansion when it is collapsed back into exponential form. But first, let us solve for $\mathcal{L}(t)$. By using the product rule for derivatives and equating the results with Eq. 1.51, we may recognize that

$$\frac{\partial}{\partial t}U(t) = \frac{\partial}{\partial t}L^\dagger(t)\mathcal{L}(t) + L^\dagger(t)\frac{\partial}{\partial t}\mathcal{L}(t) = -i(H_0 + H'(t))L^\dagger(t)\mathcal{L}(t). \quad (1.55)$$

Rearranging to solve for the time derivative of $\mathcal{L}(t)$, we find

$$\frac{\partial}{\partial t}\mathcal{L}(t) = -iL(t)(H_0 + H'(t))L^\dagger(t)\mathcal{L}(t) - L(t)\frac{\partial}{\partial t}L^\dagger(t)\mathcal{L}(t). \quad (1.56)$$

Noting that $L(t)$ represents the complex conjugate of $L^\dagger(t)$, and since $L(t)\frac{\partial}{\partial t}L^\dagger(t) = -iH'(t)$, it follows

that

$$\frac{\partial}{\partial t} \mathcal{L}(t) = -iL(t)H_0L^\dagger(t)\mathcal{L}(t). \quad (1.57)$$

If we define an interaction representation, or “togglng frame”, Hamiltonian as

$$\tilde{H}(t) = L(t)H_0L^\dagger(t), \quad (1.58)$$

then Eq. 1.57 simplifies to a form that yields a simple solution for $\mathcal{L}(t)$:

$$\frac{\partial}{\partial t} \mathcal{L}(t) = -i\tilde{H}(t)\mathcal{L}(t). \quad (1.59)$$

And thus

$$\mathcal{L}(t) = e^{-i\int_0^t \tilde{H}(t')dt'}. \quad (1.60)$$

Now, given the conditions that the perturbing Hamiltonian must be periodic and cyclic, we can assert that

$$H'(t + N\tau_c) = H'(t) \quad (1.61)$$

for an arbitrary cycle time, τ_c . In the case of an rf pulse, $\tau_c = \frac{2\pi}{\omega} \approx 10$ ms. For magic angle sample rotation, $\tau_c \approx 100$ μ s. We can note, furthermore, that the interaction representation Hamiltonian will also be periodic and cyclic:

$$\tilde{H}'(t + N\tau_c) = \tilde{H}'(t). \quad (1.62)$$

Due to this periodicity, the perturbing Hamiltonian will average to zero over one cycle, which leads to the simplification

$$L^\dagger(N\tau_c) = e^{-i\int_0^{N\tau_c} H'(t)dt} = 1. \quad (1.63)$$

Thus, if evaluated over the course of N cycle repetitions, the propagator can also be simplified as

$$U(N\tau_c) = L^\dagger(N\tau_c)\mathcal{L}(N\tau_c) = \mathcal{L}(N\tau_c) = [\mathcal{L}(\tau_c)]^N. \quad (1.64)$$

At this point, we have shown that for any periodic and cyclic perturbation, we can describe the system at any integer multiple of the cycle time by an arbitrary $\mathcal{L}(\tau_c)$ over the cycle length τ_c . We can rearrange $\mathcal{L}(\tau_c)$ to see how it directly relates to the perturbing Hamiltonian

$$\mathcal{L}(\tau_c) = e^{-i\int_0^{\tau_c} \tilde{H}(t)dt} = e^{-i\int_0^{\tau_c} e^{+i\int_0^{t'} \tilde{H}(t')dt'} H_0 e^{-i\int_0^{t'} \tilde{H}(t')dt'} dt}. \quad (1.65)$$

This form is now perfectly suited to apply a Magnus Expansion, which will collapse the nested exponential into a different power series

$$\mathcal{L}(\tau_c) = e^{-i\tau_c[\bar{H}^{(0)} + \bar{H}^{(1)} + \bar{H}^{(2)} + \dots]} \quad (1.66)$$

where the $\bar{H}^{(n)}$ are average Hamiltonians, with the first few given by

$$\begin{aligned} \bar{H}^{(0)} &= \frac{1}{\tau_c} \int_0^{\tau_c} \tilde{H}(t) dt \\ \bar{H}^{(1)} &= \frac{i}{2\tau_c} \int_0^{\tau_c} dt_1 \int_0^{t_1} dt_2 [\tilde{H}(t_1), \tilde{H}(t_2)] \\ \bar{H}^{(2)} &= -\frac{1}{6\tau_c} \int_0^{\tau_c} dt_1 \int_0^{t_1} dt_2 \int_0^{t_2} dt_3 \left\{ [\tilde{H}(t_1), [\tilde{H}(t_2), \tilde{H}(t_3)]] + [\tilde{H}(t_3), [\tilde{H}(t_2), \tilde{H}(t_1)]] \right\}. \end{aligned} \quad (1.67)$$

Thus, knowledge of the toggling frame, or interaction representation Hamiltonian will yield straightforward calculation of the average Hamiltonian for a spin system.

This is a powerful technique that can be used to explain the Bloch Siegert Shift, which is a small shift in the resonant frequency that arises from the counter-rotating component in a driven oscillator (such

as a solenoid or coil which sends out the radio frequency pulse that is used to induce a changing magnetic field to perturb spin systems in magnetic resonance experiments).

Average Hamiltonian Theory can also be used to predict ways to achieve homonuclear decoupling by averaging out dipolar interactions through some strategic experimental setups. The first common example of this is magic angle spinning, which affects the real space component of the overall Hamiltonian. We can also design multi-pulse sequences to influence the spin space part of the Hamiltonian (which, recall, is a product of real and spin space components) – the WAHUHA experiment [11] is one such example.

Ultimately, AHT is an important tool that should have a place in the “mathematical toolbox” of every quantum chemist.

References

- [1] Levitt M. *Spin Dynamics: Basics of Nuclear Magnetic Resonance*. John Wiley & Sons, Ltd, New York, NY, 2001.
- [2] Blumich B, Perlo J, Casanova F. Mobile single-sided NMR. *Prog Nucl Magn Reson Spectrosc* 2008;52(4):197-269.
- [3] Freeman R. *A Handbook of Nuclear Magnetic Resonance* (second ed.). Longman Group, London, United Kingdom, 1997.
- [4] Einstein A. *Investigations on the Theory of the Brownian Movement*. Dover Publications, Mineola, New York, 1956 (re-publication of the original translation from 1926).
- [5] Debye PJW. *Polar Molecules*: The Chemical Catalog Company, Inc., New York, 1929.
- [6] Ernst R, Bodenhausen G, Wokaun A. *Principles of Nuclear Magnetic Resonance in One and Two Dimensions*. Oxford University Press, Oxford, United Kingdom, 1990.
- [7] Kowalewski J, Mäler L. *Nuclear Spin Relaxation in Liquids: Theory, Experiments, and Applications*. Taylor & Francis, Boca Raton, Florida, 2006.
- [8] Van de Ven FJM. *Multidimensional NMR in Liquids*. Wiley-VCH, New York, Weinheim, Cambridge, 1995.
- [9] Magnus W. On the exponential solution of differential equations for a linear operator. *Comm. Pure and Appl. Math.* 7(4): 649–673, 1954.
- [10] Waugh JS. Average Hamiltonian Theory. *eMagRes*. 2007. DOI: 10.1002/9780470034590.emrstm0020
- [11] Waugh JS, Huber LM, Haeberlen U. *Phys. Rev. Lett.* 20, 180–182, 1968.
- [12] CHE 210B Course Notes (Alexei Stuchebrukhov, UC Davis).
- [13] CHE 216 Course Notes (Matthew Augustine, UC Davis).
- [14] CHE 216 Course Notes (R. David Britt, UC Davis).

2. NUCLEAR SPIN RELAXATION: FROM FUNDAMENTAL MECHANICS TO PRACTICAL APPLICATION

We think there is color, we think there is sweet, we think there is bitter, but in reality there are atoms and a void.

– DEMOCRITUS, C. 460 – C. 370 BC

Relaxometry is a convenient way of obtaining distinctive chemical information with low-field, portable NMR. It is employed widely in areas such as medical imaging, process control, and security sensing. In particular, single-sided nuclear magnetic resonance (NMR) is a powerful experimental technique because it can non-invasively probe samples with unorthodox geometries and differentiate between components of mixtures. Furthermore, the low frequencies associated with permanent magnets can penetrate conductive layers covering a sample. Due to the low resolution associated with weak field strengths, the longitudinal and transverse relaxation rate constants (T_1 and T_2) and the diffusion coefficient (D) are the parameters typically extracted from this form of NMR, rather than chemical shifts and J-couplings. This is because the T_1 , T_2 , and D parameters are easily obtained from an inhomogeneous magnet. In particular, 2D relaxometry is useful due to its ability to correlate measurables in a material, thereby giving insight to exchange processes. The mathematical functions that govern the observed signals are damped exponentials, and thus can be elucidated through data processing. The immediate usefulness of a measurement is largely influenced by the efficiency of the data processing technique that is implemented. Before discussing data analysis in further detail, let us first explore the mechanisms of spin relaxation on a fundamental level.

2.1 Relaxation Mechanisms

In general, spin relaxation arises from temporal or spatial variations in the magnetic field in which a collection of spins exist [1-6]. One predominant effect that leads to these magnetic field fluctuations is the random dipolar interactions between nuclei, which occur naturally as a result of molecular motion. These dipolar interactions allow dissipation of the transition energy from an excited state to the ground state (i.e., a transition from nonequilibrium alignment with the static magnetic field following the cessation of a pulse to parallel or antiparallel alignment according to the Boltzmann distribution).

Another way of saying this is that relaxation is facilitated by molecular tumbling or material structure that causes nuclei to exist in proximity to each other and, thereby increasing the probability and rate of dipolar interactions for cross-relaxation. This can also be pictured as dissipation of energy to a surrounding spin bath.

The timescale of molecular motion is important to predict its resulting physical effects, and can be correlated to the relative amount of energy needed for the resulting process that occurs.

2.1.1 Longitudinal Magnetization and T_1

The time constant T_1 characterizes the time it takes longitudinal relaxation to recover to thermal equilibrium alignment with the static magnetic field, B_0 . It is important to note that a signal directly associated with longitudinal magnetization, M_z , is not directly measurable with a conventional single-channel NMR setup; as such, saturation or inversion recovery experiments involve a final “read-out” pulse to tip the longitudinal magnetization into the transverse plane for detection. As shown in Fig. 2.1, it is also

possible to calculate M_z as $M_z = \gamma \hbar \text{Tr} \{ \hat{\sigma} \hat{I}_z \} = \gamma \hbar \overline{\langle \hat{I}_z \rangle}$.

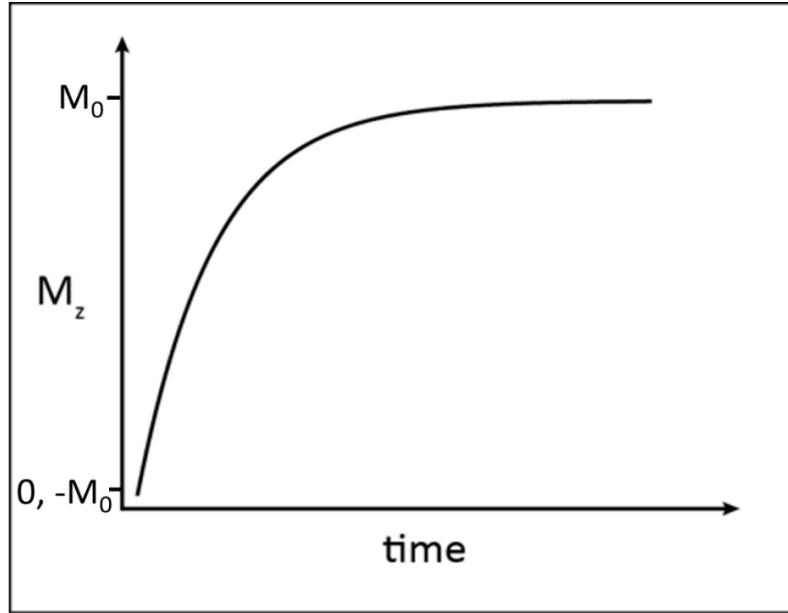


Figure 2.1. Plot of the z component of magnetization over time as equilibrium is achieved. At time = 0, $M_z = 0$ or $-M_0$, depending on whether a saturation recovery or inversion recovery pulse sequence is used.

For an inversion recovery experiment, a diagrammatic representation of a pulse sequence is shown in Fig. 2.2.

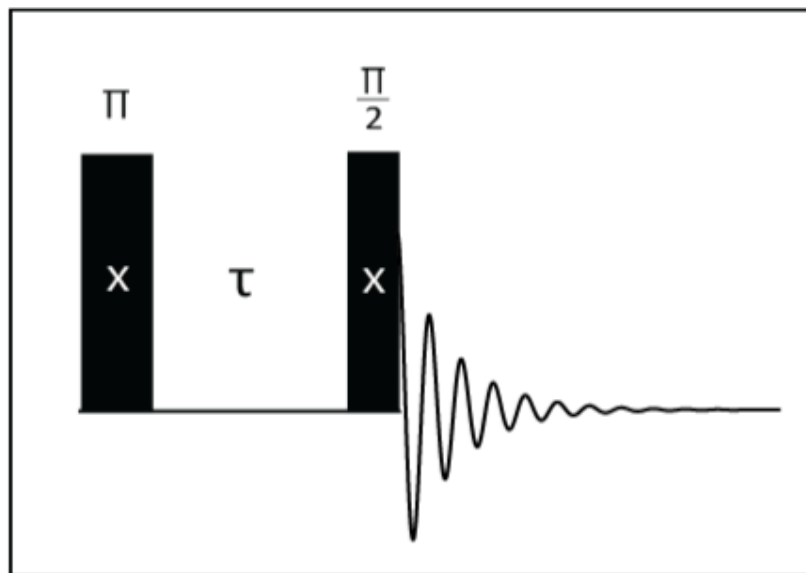


Figure 2.2. Inversion recovery pulse sequence diagram.

For a saturation recovery experiment, a pulse sequence is shown in Fig. 2.3.

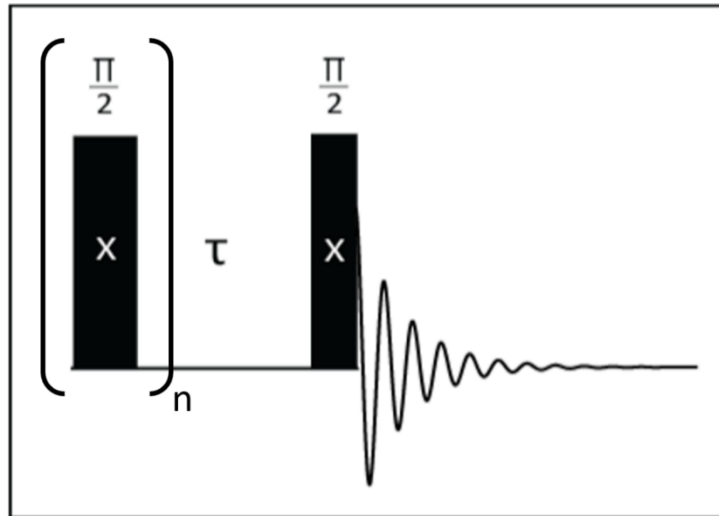


Figure 2.3. Saturation recovery pulse sequence diagram, where the first train of $\frac{\pi}{2}$ pulses is repeated n times to achieve “saturation” of magnetization.

2.1.2 *Transverse Magnetization and T_2*

The T_2 relaxation rate constant relates to dephasing in the transverse plane, which can also be described as a loss of phase coherence within a spin system. This is caused by precession at slightly varying rates due to local, fluctuating fields, as shown in Fig. 2.4.

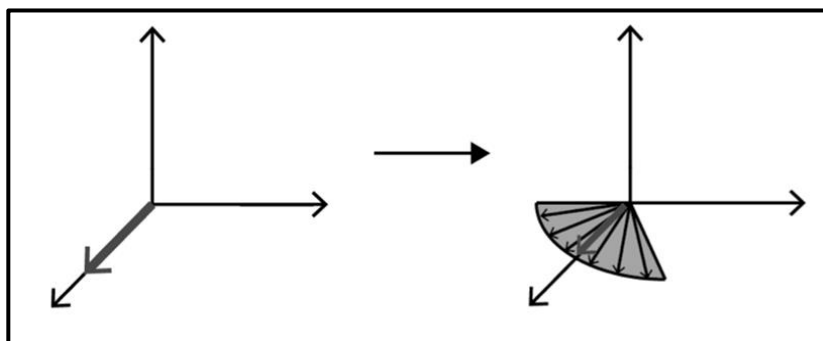


Figure 2.4. Dephasing of spins that results in loss of transverse magnetization over time.

T_2 is often measured by a Carr-Purcell-Meiboom-Gill (CPMG) pulse sequence involving a long train of echoes, shown diagrammatically in Fig. 2.5.

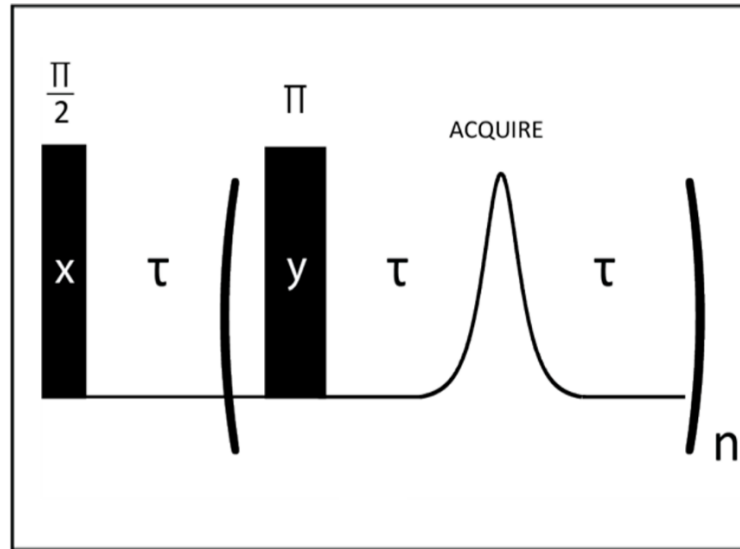


Figure 2.5. Carr-Purcell-Meiboom-Gill (CPMG) pulse sequence diagram.

The intensity of the echoes in a CPMG experiment decays over time, as pictured in Fig. 2.6, and the envelope of their decay can be fit to extract T_2 .

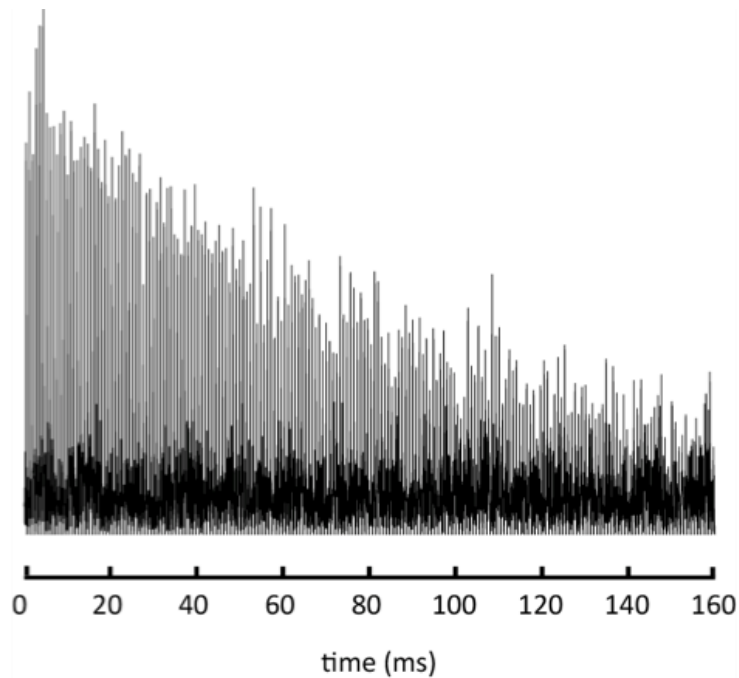


Figure 2.6. Echo train signal following application of a CPMG pulse sequence.

The signals observable with rf coils are associated with transverse magnetization, such as $M_x = \gamma\hbar\text{Tr}\{\hat{\sigma}\hat{I}_x\} = \gamma\hbar\langle\hat{I}_x\rangle$ and $M_y = \gamma\hbar\text{Tr}\{\hat{\sigma}\hat{I}_y\} = \gamma\hbar\langle\hat{I}_y\rangle$.

2.1.3 Relationships between T_1 , T_2 , and the Autocorrelation Time, τ_c

T_1 and T_2 are convenient parameters to describe the interactions between spins and locally fluctuating fields that are brought about by molecular motion, chemical exchange, thermal motion in the lattice, and nearby paramagnetic centers. The timescale of the interaction is ultimately one of the most important features that will dictate its relaxation effects. It can be seen in Eq. 2.1 that T_1 is related to x and y fluctuations as

$$\frac{1}{T_1} = \frac{\gamma^2 \langle B_x^2 + B_y^2 \rangle \tau_c}{1 + \tau_c^2 \omega_0^2} \quad (2.1)$$

and is most strongly influenced by fluctuations near the Larmor frequency, $\omega = \gamma B_0$. Here, τ_c represents the autocorrelation time, which is defined as the time it takes for a molecule to rotate one radian. Alternatively, the autocorrelation time can be expressed as a ratio of viscosity, η , and volume, V , to the thermal energy, kT , as $\tau_c = \frac{\eta V}{kT}$.

Next, we will describe T_2 , noting that this parameter relates to fluctuations in the z direction as

$$\frac{1}{T_2} = \gamma^2 \langle B_z^2 \rangle \tau_c + \frac{1}{2} \frac{\langle B_x^2 + B_y^2 \rangle \tau_c}{1 + \tau_c^2 \omega_0^2}. \quad (2.2)$$

T_2 is most sensitive to low frequency fluctuations, in which ω approaches zero. The so-called “extreme narrowing limit” can be found by plotting T_1 and T_2 versus the autocorrelation time, as shown in Fig. 2.7.

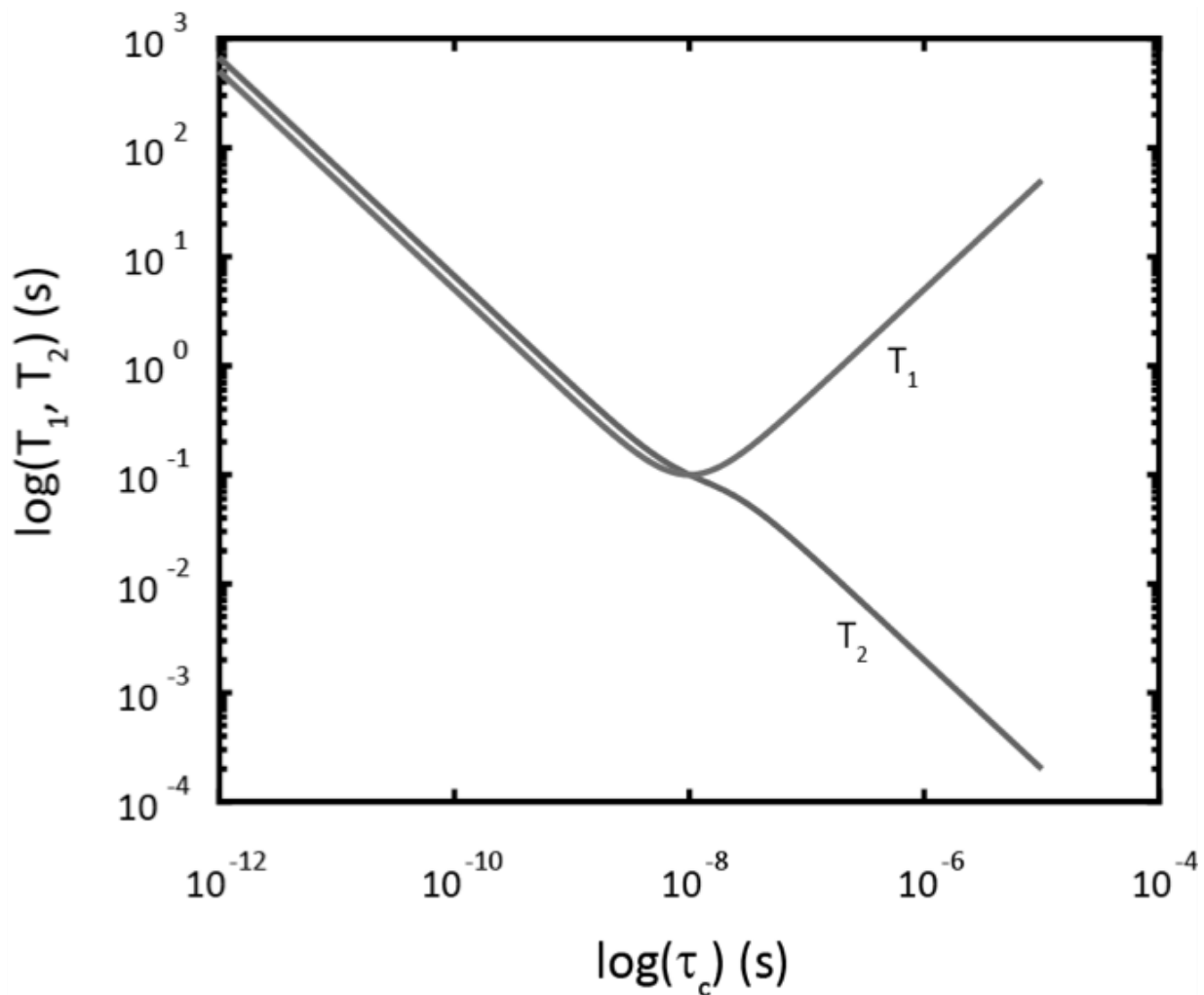


Figure 2.7. Logarithmic plot showing the relationship between T_1 and T_2 and the autocorrelation time.

Now that we have a grasp of some theoretical essentials of magnetic resonance, we will turn our attention to the next chronological steps in an NMR experiment after the signal has been recorded. The development and implementation of the new data processing algorithms is motivated by the need for field-based instruments that can be used in remote settings, such as field hospitals, factories, and geological sites for immediate analysis of noisy spectroscopic signals. Typically, filtering is an important step before fitting, and this is discussed in Ch. 3. Signal analysis is then completed with fitting the filtered signal and extracting the parameters of interest; this is discussed in Ch. 4. The coupling and automation of these strategies allows

us to tackle diverse and previously inaccessible problems, some examples of which are discussed in the remaining chapters.

References

- [1] Levitt M. Spin Dynamics: Basics of Nuclear Magnetic Resonance. John Wiley & Sons, Ltd, New York, NY, 2001.
- [2] Freeman R. A Handbook of Nuclear Magnetic Resonance (second ed.). Longman Group, London, United Kingdom, 1997.
- [3] Einstein A. Investigations on the Theory of the Brownian Movement. Dover Publications, Mineola, New York, 1956 (re-publication of the original translation from 1926).
- [4] Debye PJW. Polar Molecules: The Chemical Catalog Company, Inc., New York, 1929.
- [5] Ernst R, Bodenhausen G, Wokaun A. Principles of Nuclear Magnetic Resonance in One and Two Dimensions. Oxford University Press, Oxford, United Kingdom, 1990.
- [6] Kowalewski J, Mäler L. Nuclear Spin Relaxation in Liquids: Theory, Experiments, and Applications. Taylor & Francis, Boca Raton, Florida, 2006.

3. THE MATRIX PENCIL AS A TUNABLE FILTER

A peculiar beauty reigns in the realm of mathematics, a beauty which resembles not so much the beauty of art as the beauty of nature and which affects the reflective mind, which has acquired an appreciation of it, very much like the latter.

– Ernst Eduard Kummer, 1810 – 1893

Abstract

The matrix pencil method (MPM) is developed as a tunable filtering and phasing tool for nuclear magnetic resonance (NMR) spectroscopy. The next chapter more rigorously and methodically describes the MPM and its use as a fitting tool in NMR is demonstrated. In this chapter, the ability of the MPM to precisely model noisy data is explored for the purposes of achieving a mathematical separation of the information-containing signal from the noise and promoting the usefulness of this approach. First, data from unilateral magnetic resonance experiments provides a framework for demonstration of the MPM filtering ability by modeling the damping components of a signal, and selectively reconstructing the low frequency decay without the risk of aliasing seen with Fourier filters. Next, a modulation in a steady state free precession experiment is removed to aid in analysis, which is useful for correcting field drifting from temperature variations in long measurements. Finally, for high field experiments, a pure phase correction is shown to aid with “untwisting” complex spectra in simulation as well as data resulting from a water suppression pulse sequence. The cases shown here suggest that the matrix pencil filter is a simple and versatile tool that can enhance the results obtained from both low and high field experiments.

3.1 Introduction

As digital signal acquisition technology has progressed in NMR spectroscopy, multifarious filters have been developed for pre-processing data [1]. Filters are necessary for a myriad of reasons, with one of the most notable being the fact that NMR is a fundamentally insensitive measurement. The electrical signals detected in a receiver are typically on the order of μV , and therefore must be significantly amplified for substantive analysis to occur [2]. Application of a pass-band filter can considerably improve the sensitivity and signal to noise ratio. Other issues that may be encountered in pre-processing are the introduction of unwanted frequencies, sometimes arising from field drifting due to thermal instability or heteronuclear contamination, and phase twisting of complex spectra. Fourier transform windowing filters are one of the most widely used methods, but other techniques such as wavelet transforms have also been explored recently [3,4]. However, there is still room for improvement in the filters that exist to this date. In the standard approach, pass-band filters are implemented in the frequency domain. While this is strategy is natural in the case of high field spectroscopic and imaging applications, this method is less suited for low field NMR data that is typically analyzed in the time domain [2,5].

The matrix pencil method (MPM) has been established as an algorithm for parameter estimation of exponentially damped and undamped sinusoids in NMR relaxometry [6-9]. Indeed, the MPM is less susceptible to some of the difficulties associated with the gold standard inverse Laplace transform (ILT) [10-13] in low resolution cases that cause instability in integral transforms. To demonstrate the usefulness of the MPM in disentangling the components of complex materials and mixtures with a high degree of precision, a comparative analysis of crude oil is shown in Fig. 3.1 with the MPM and ILT.

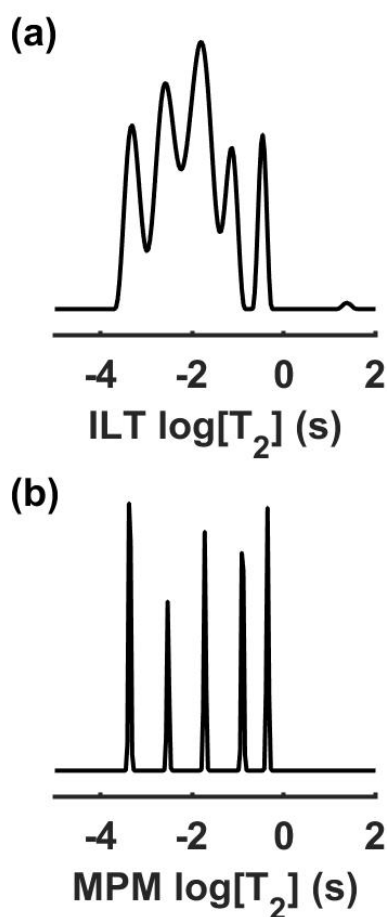


Figure 3.1. In comparison to the ILT processing method in (a), the MPM offers superb resolution in (b), as demonstrated by a comparative analysis of a crude oil with five T_2 components.

The matrix pencil method can also be used as a tunable filtering and phasing tool for NMR spectroscopy. Here, the ability of the MPM to precisely model noisy data is explored for the purpose of achieving a mathematical separation of the meaningful signal from the noise. First, data from unilateral magnetic resonance experiments provides a framework for demonstration of the filtering ability by modeling the damping components of a signal, and selectively reconstructing the low frequency decay without the risk of aliasing seen with Fourier filters. Next, a modulation in a steady state free precession (SSFP) experiment [5] is removed to aid in analysis, which is useful for correcting field drifting from temperature variations in long measurements. Finally, for high field experiments, a pure phase correction

is shown to aid with “untwisting” complex spectra in simulation as well as data resulting from a water suppression pulse sequence. The cases shown here suggest that the matrix pencil filter is a simple and versatile tool that can enhance the results obtained from both low and high field experiments.

3.2 Theory

The goal of this section is to describe the implementation of the MPM as a filter to remove noise and enhance the signal. One may proceed in essentially the same way as with a Fourier filter applied in a tunable low pass, high pass, or notch style. The critical difference with the MPM is that the eigenvalues yield a distribution of real and imaginary frequency components with resolution matching the number of data points, whereas a Fourier filter only obtains imaginary components. The matrix pencil filter (MPF) can therefore model and smooth the damping components of a signal with greater accuracy while simultaneously allowing the reconstruction of pure phased spectra, as demonstrated in Fig. 3.2. An additional benefit to this approach is that it is not susceptible to aliasing, due to its ability to also obtain the real components of an exponential signal, unlike Fourier filters which often cause a loss of the beginning and ending data points due to necessary truncation of aliased components.

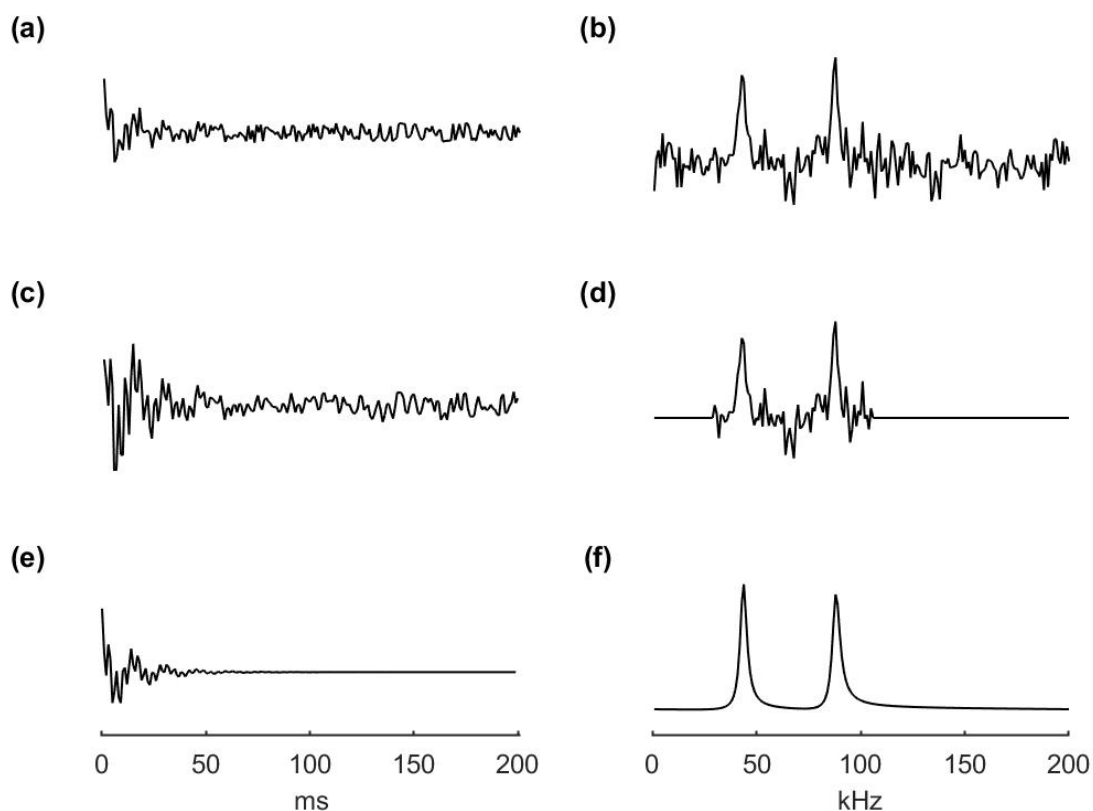


Figure 3.2. A simulated noisy signal in (a) and corresponding spectrum in (b) is Fourier filtered with a 65 kHz window in (d), yielding the inverse transformed signal in (c). In contrast, the MPM filtered spectrum is shown in (f), with the reconstructed signal in (e). The MPM was performed with 20 components, and filtering was also accomplished with a 65 kHz bandwidth.

The MPM can be used in a straightforward way to determine the number of decay constants present in a damped, transient 1D or 2D signal, as well as their relative contributions and values. At this point, knowledge of a set of decay constants and respective amplitudes allows reconstruction of the initially decomposed noisy signal. To filter this data, specific frequencies can be selectively removed, and a signal can be reconstructed with any subset of the originally decomposed data that is desired to preserve the meaningful components and discard the obfuscating noise or unwanted modulations or phase twisting.

3.3 Experimental

To assess the widespread scope and utility of the MPF technique, a range of samples were analyzed with a variety of pulse sequences and magnets. Samples included crude oil, cod liver oil, mineral oil, a standardized equal volume mixture of olive oil and 3.12 mM CuSO₄ in water, and a standardized mixture of 80% water and 20% ethyl alcohol by volume. All chemicals were obtained from Sigma-Aldrich except for olive oil, which was purchased from Trader Joe's and used as received, and the crude oil and cod liver oil which were used as received.

The first three oil samples were studied with a Carr-Purcell-Meiboom-Gill (CPMG) pulse sequence for T₂ measurement. The olive oil/water mixture was used with a steady state free precession (SSFP) pulse sequence [14]. The ethyl alcohol/water mixture was explored with a 1331 water suppression pulse sequence as described by P. J. Hore [15].

The crude oil sample was analyzed with a 0.55 T (23 MHz ¹H Larmor frequency) Pure Devices benchtop magnet with a delay of 80 μs between the π radio frequency (rf) pulses of the CPMG and 32 scans for signal averaging.

The cod liver oil was analyzed with 0.40 T and 0.47 T (17 MHz and 20 MHz ¹H Larmor frequency) unilateral magnets constructed by Bruce Balcom, et al. at the University of New Brunswick [16]. A delay of 300 μs between the π rf pulses was used in CPMG experiments with 8 scans for signal averaging.

The mineral oil was analyzed with a 0.11 T (4.5 MHz ¹H Larmor frequency) unilateral magnet also built by Bruce Balcom et al., interfaced to a Tecmag Redstone spectrometer and a homebuilt rf coil with a delay of 400 μs between the CPMG π rf pulses and 8 scans for signal averaging.

A 1.01 T (43.7 MHz ¹H Larmor frequency) Aspect Imaging M100 magnet with a 60 mm bore was interfaced to a Tecmag Apollo spectrometer to provide a large volume, homogeneous region to explore the relaxometry properties of the olive oil/water mixture with SSFP experiments. Typically, π/2 rf pulse lengths

of 30 μs with 7 W of applied rf power were used with a pulse spacing of 3 μs and a maximum delay time of 1.6 ms.

An Aspect Imaging 1.4 T (60 MHz ^1H Larmor frequency) cryogen-free, high-resolution benchtop spectrometer was interfaced to a Tecmag Apollo spectrometer and used with a 1331 pulse sequence to explore water suppression with the 80% water, 20% ethyl alcohol sample. Typical $\pi/2$ rf pulse lengths of 8 μs with 2.4 W of applied rf power were used.

All calculations and MPM data processing were accomplished with Matlab (Mathworks, Natick, MA). All comparison ILT relaxometry results were generated using Prospa, the commercially available ILT software from Magritek (Malvern, PA.).

3.4 Results and Discussion

In the limit of zero noise, the MPM provides an analytically exact, closed-form solution to the problem of multi-exponential decomposition. This ability of the MPM to precisely model diverse arrays of data also enables it to handle noisy relaxometry signals by acting as a robust filter similar to singular value decomposition.

Figure 3.3 illustrates a typical workflow for the bandpass filtering process with the MPM by first modeling the data, and then incrementally narrowing the bandpass region until all apparent noise has been removed, but the specific signature of the decay rate has not been altered in the signal.

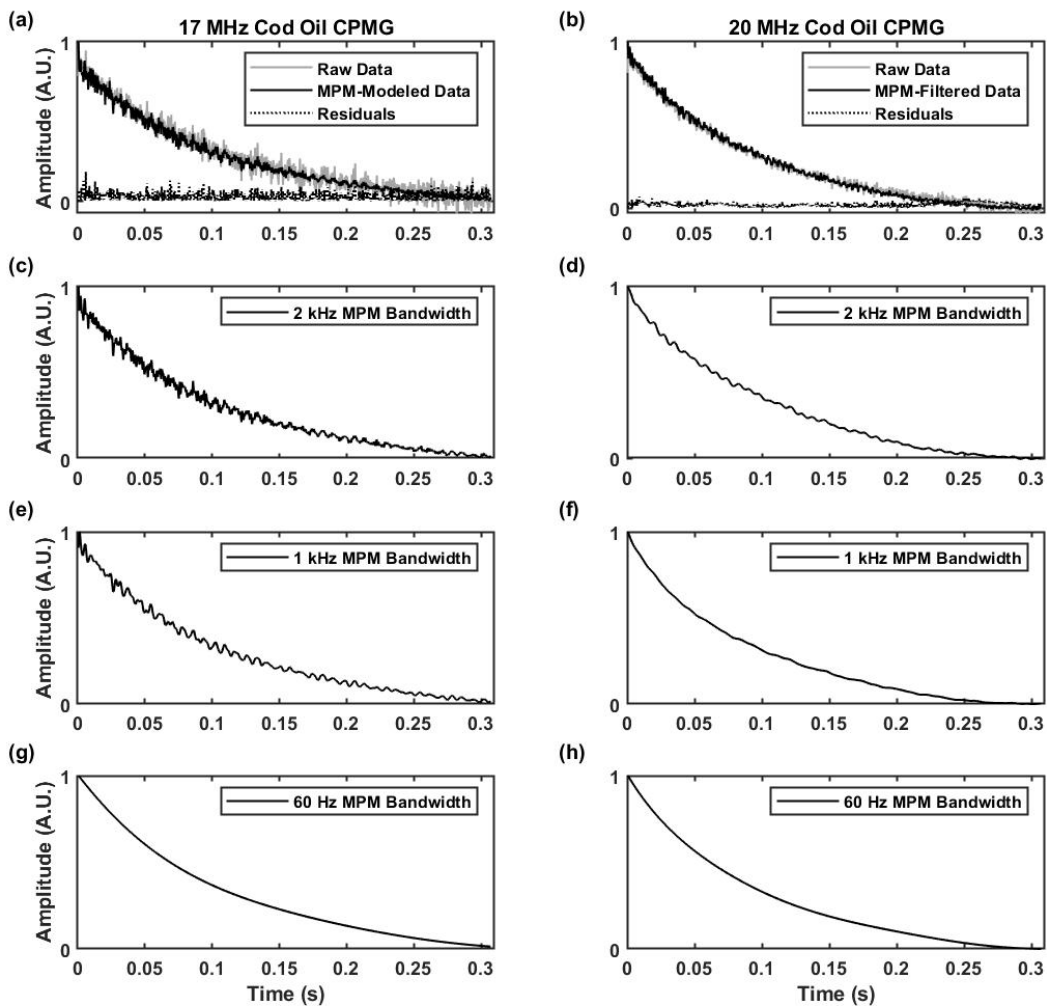


Figure 3.3. Standard CPMG data of cod liver oil at 17 MHz (left) and 20 MHz (right) with incrementally increasing filtering. The plots in (a) and (b) show the raw data in grayscale overlaid with MPM models of the data created by reconstructing the data as a sum of damped exponentials; the residuals in each case are shown as a dotted line to demonstrate the ability to model the noisy data precisely. This ability to model the noise allows for incremental elimination of the higher frequency exponential components attributed to noise by systematic reduction of bandwidth, as shown in the process from (a) to (c) to (e) to (g) for 17 MHz data in the left column, and from (b) to (d) to (f) to (h) for 20 MHz data in the right column.

Next, a test sample composed of mineral oil was chosen to study the performance of the MPF in much noisier data with a standard CPMG relaxometry experiment. A comparison of ILT analysis of the raw signal and the MPM filtered signal is shown in Fig. 3.4(a) and (b) to demonstrate how filtering can improve the ILT analysis on data that may otherwise not be reasonably processed with the ILT. The ILT initially produced a reasonable, single-component distribution, but fragmented when the limits were narrowed due to instability of the posed mathematical problem.

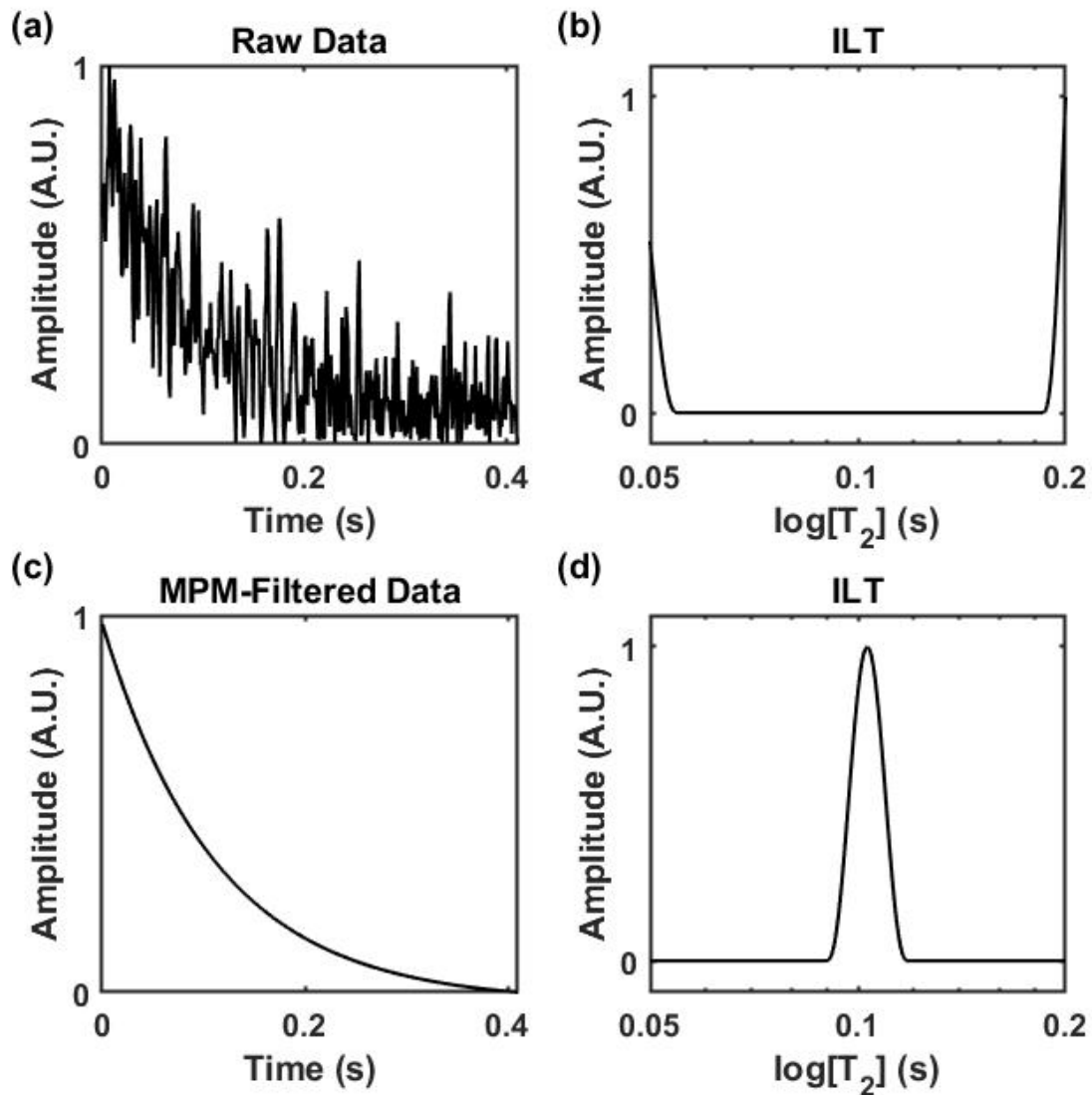


Figure 3.4. Standard CPMG of a mineral oil sample with a 4 MHz unilateral magnet. The raw data shown in (a) is unfit for Laplace inversion, shown in (b) which yielded only edge artifacts when the fitting

window was narrowed. The MPM filtered signal shown in (c) yielded a much more stable ILT, shown in (d).

To explore additional uses of the MPF, a steady state free precession experiment was considered next. Here, an additional modulation in the exponential decay of the signal to a steady state inhibits straightforward fitting and analysis of the data. Figure 3.5 illustrates the raw data and the data following removal of the modulation with the MPF. The demodulation enables direct analysis of the decay with any processing method desired, such as the ILT, nonlinear least squares fitting, or MPM.

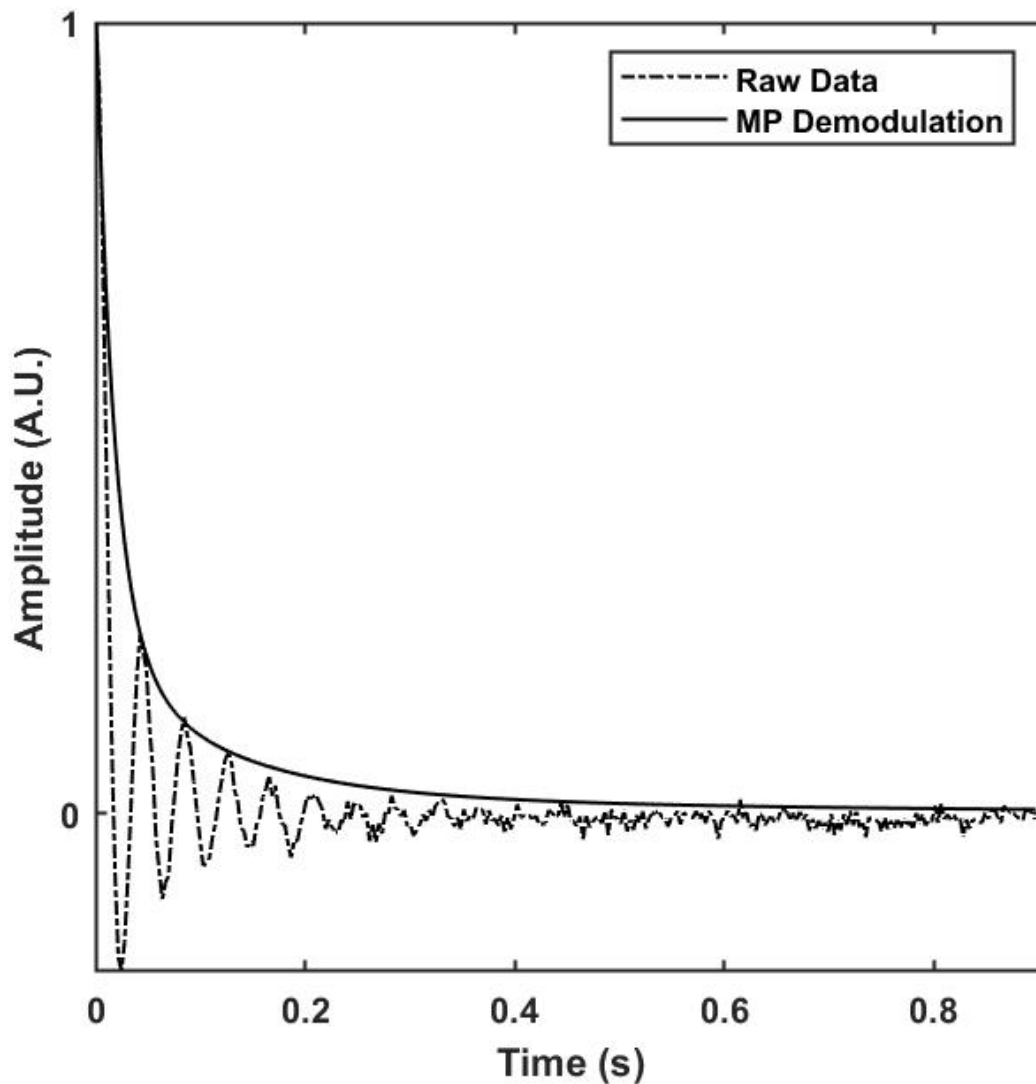


Figure 3.5. Demodulation of the signal from a steady state free precession experiment with a standardized sample composed of equal volumes of olive oil and 3.12 mM CuSO_4 -doped water.

The next example in Fig. 3.6 demonstrates filtering the imaginary part of the signal, rather than the real. To explore ability of the MPM to produce pure absorption phased spectra, a simulated spectrum in Matlab was generated and analyzed with the MPF to reconstruct a spectrum with zero and first order phase corrections, i.e., with phase distortions removed, but no other alterations.

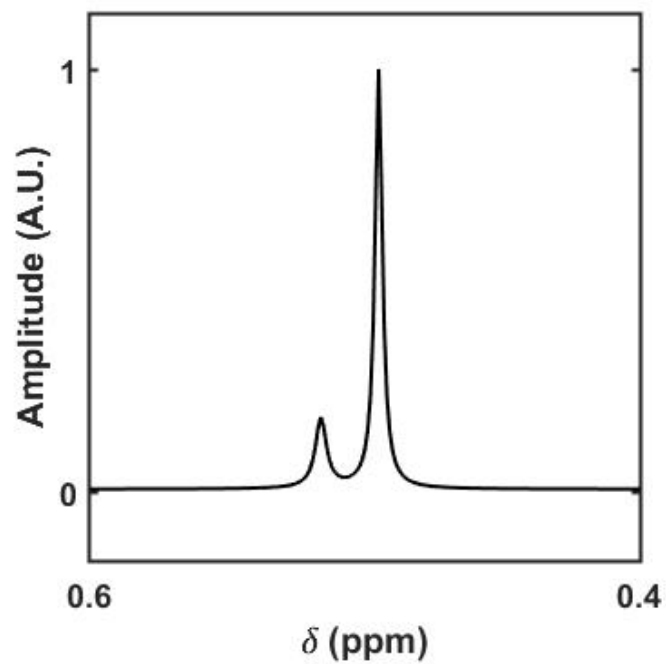
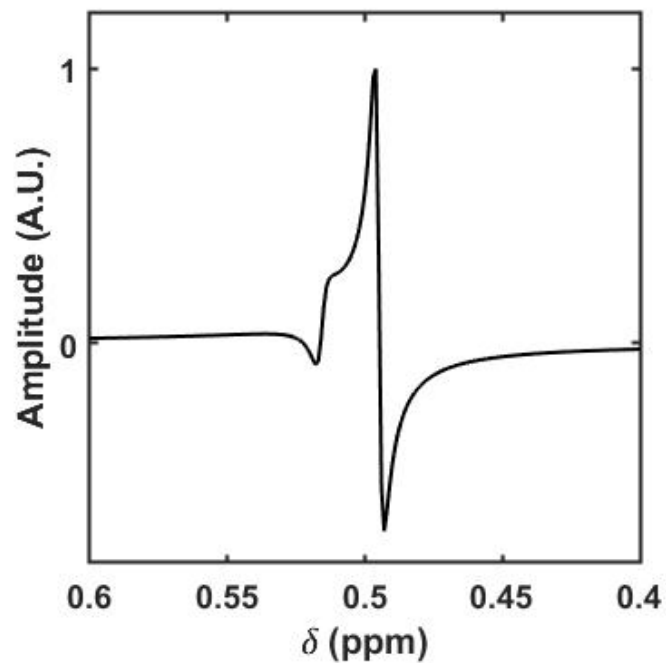


Figure 3.6. Simulated data created in Matlab depicted in (a) was analyzed with the MPF for pure absorption phase correction shown in (b).

To apply the MPM as a pure phasing tool on experimental data, a sample of wet ethyl alcohol was studied at a 60 MHz ^1H Larmor frequency with the benchtop, cryogen-free Aspect magnet. The initial spectrum without water suppression is shown alongside the resulting phase distorted spectrum after a 1331 water suppression pulse sequence was applied in Fig. 3.7 (a-b), as well as the MPM phase corrected spectrum in Fig. 3.7 (c).

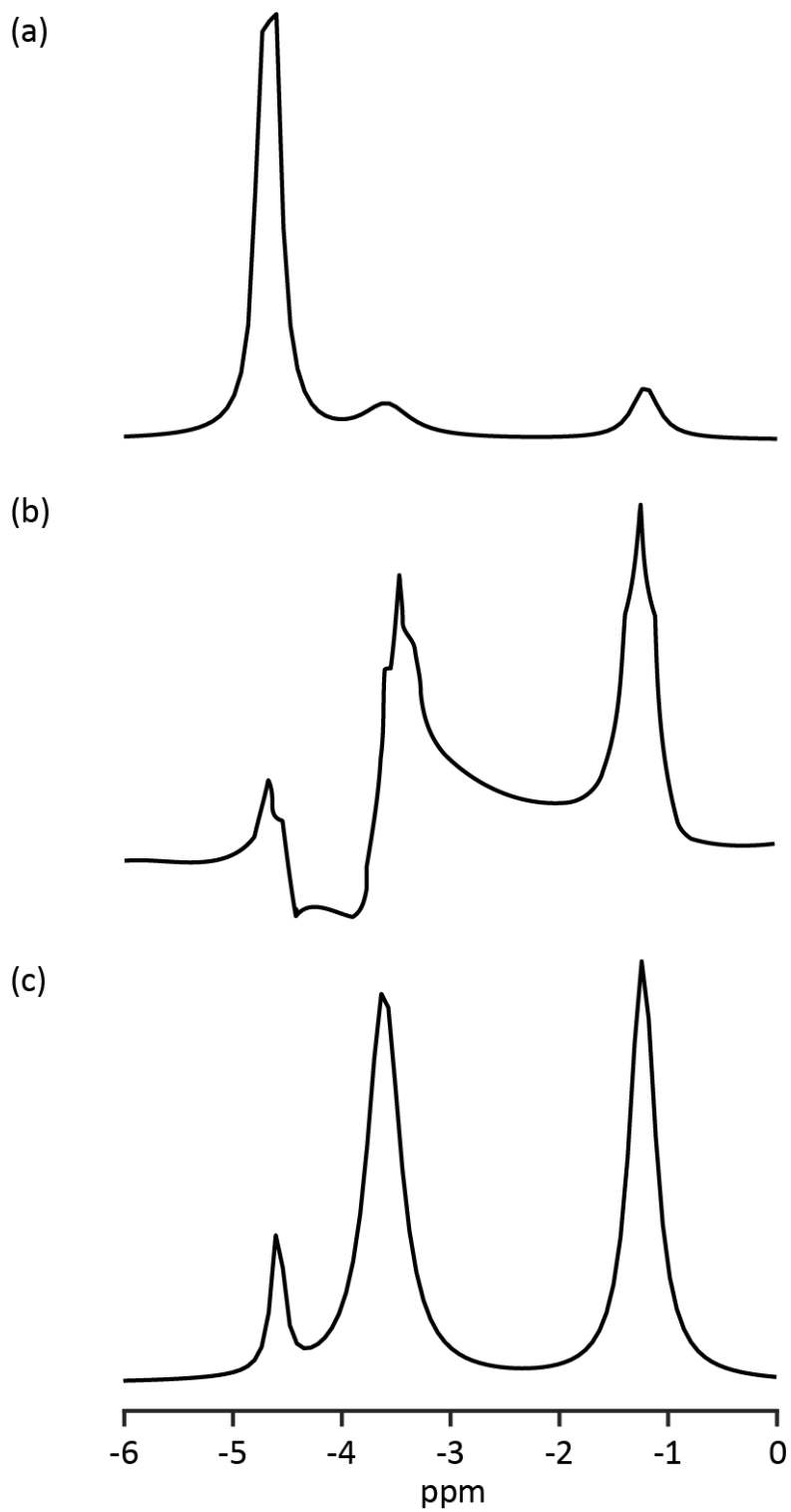


Figure 3.7. (a) ^1H spectrum from AI60 of 80% water, 20% ethyl alcohol sample, where (b) shows water suppression of the same sample with a 1331 pulse sequence with resulting phase twisting and (c) shows the MPM reconstruction of the pure phased spectrum from (b).

Ultimately, the usefulness of NMR is limited by the ability of an algorithm to extract information from a recorded signal. Based on its performance here, the MPM appears to enhance the ability of other algorithms to extract information when used as a filter.

3.5 Conclusion

The ability of the MPM to function as both a filtering tool and as a fitting tool allow it to perform at the interface between low S/N input and high resolution output. The broad canvas of samples, pulse sequences, and magnets considered in this study demonstrate the versatility and robustness of the MPM. This suggests that the use of matrix pencil-based techniques will facilitate the analysis of systems and samples that have previously been inaccessible to NMR spectroscopy.

Acknowledgements

The authors thank Dr. Michael McCarthy for his continued inspiration, and Dr. Charlie Eads for valuable guidance and constructive feedback. Support from the University of Washington, Center for Process Analysis and Control is gratefully acknowledged.

References

- [1] D. Moskau, Application of real time digital filters in NMR spectroscopy, *Concepts Magn. Reson.*, 15(2) (2002) 164–176.
- [2] A. Valori, J. Mitchell, E.J. Fordham, Digital filters for low-field NMR, *Concepts Magn. Reson. Part B*, 46B (2016) e21346.
- [3] W.M Wittbold, A.J. Fischman, C. Ogle, D. Cowburn, Optimal filtering in Fourier transform NMR, *J. Magn. Reson.*, 39 (1980) 127-135.
- [4] R. Xie, Y. Wu, K. Liu, M. Liu, L. Xiao, De-noising methods for NMR logging echo signals based on wavelet transform, *J. Geophys. Eng.*, 11 (2014) 035003.
- [5] T. Monaretto, A. Souza, T.B. Moraes, V. Bertucci-Neto, C. Rondeau-Mouro, L.A. Colnago, Enhancing signal-to-noise ratio and resolution in low-field NMR relaxation measurements using post-acquisition digital filters, *Magn. Reson. Chem.*, 57(9) (2019) 616-625.
- [6] S.N. Fricke, J.D. Seymour, M.D. Battistel, D.I. Freedberg, C.D. Eads, M.P. Augustine, Data processing in NMR relaxometry using the matrix pencil, *J. Magn. Reson.*, 313 (2020) 106704.
- [7] Y. Lin, P. Hodgkinson, M. Ernst, A. Pines, A novel detection-estimation scheme for noisy NMR signals: Applications to delayed acquisition data, *J. Magn. Reson.*, 128(1) (1997) 30–41.
- [8] V.A. Mandelshtam, H.S. Taylor, A.J. Shaka, Application of the filter diagonalization method to one- and two-dimensional NMR spectra, *J. Magn. Reson.*, 133 (1998) 304-312.
- [9] Y. Hua, T.K. Sarkar, Matrix pencil method for estimating parameters of exponentially damped/undamped sinusoids in noise, *IEEE Trans. Acoust. Speech Signal Process.*, 38(5) (1990) 814–824.

- [10] L. Venkataramanan, Y. Song, M. Hurlimann, Solving Fredholm integrals of the first kind with tensor product structure in 2 and 2.5 dimensions, *IEEE Trans. Signal Process.* 50 (5) (2002) 1017–102.
- [11] Y. Song, L. Venkataramanan, L. Burcaw, Determining the resolution of Laplace inversion spectrum, *J. Chem. Phys.*, 122 (2005) 104104.
- [12] C.L. Lawson, R.J. Hanson, *Solving Least Squares Problems*, Prentice-Hall, Englewood Cliffs, NJ, USA, 1974.
- [13] R.J.S. Brown, Proton relaxation in crude oils, *Nature*, 189 (1961) 4762.
- [14] P. Waldstein, W.E. Wallace, Jr., Driven equilibrium methods for enhancement of nuclear transients, *Rev. Sci. Instr.*, 42(4) (1971) 437-440.
- [15] P.J. Hore, Solvent suppression in fourier transform nuclear magnetic resonance, *J. Magn. Reson.*, 55(2) (1983) 283-300.
- [16] A.E. Marble, I.G. Mastikhin, B.G. Colpitts, B.J. Balcom, A compact permanent magnet array with a remote homogeneous field, *J. Magn. Reson.*, 186 (2007) 100-104.

4. DATA PROCESSING IN NMR RELAXOMETRY USING THE MATRIX PENCIL

Reproduced in part with permission from “S.N. Fricke, J.D. Seymour, M.D. Battistel, D.I. Freedberg, C.D. Eads, M.P. Augustine, Data processing in NMR relaxometry using the matrix pencil, *J. Magn. Reson.*, **313** (2020) 106704.”

Abstract

The matrix pencil method (MPM) is explored for stable, reproducible data processing in nuclear magnetic resonance (NMR) relaxometry. Data from one-dimensional and two-dimensional relaxometry experiments designed to measure transverse relaxation T_2 , longitudinal relaxation T_1 , diffusion coefficient D values, and their correlations in a standard olive oil/water mixture serve as a platform available to any NMR spectroscopist to compare the performance of the MPM to the benchmark inverse Laplace transform (ILT). The data from two practical examples, including the drying of a solvent polymer system and the enzymatic digestion of polysialic acid, were also explored with the MPM and ILT. In the cases considered here, the MPM appears to outperform the ILT in terms of resolution and stability in the determination of fundamental constants for complex materials and mixtures.

4.1 Introduction

The translation of a time-dependent signal into values for meaningful parameters is central to a successful nuclear magnetic resonance (NMR) experiment. In the case of high resolution, high field NMR, the fast Fourier transform (FFT) is used to convert a time domain, oscillatory signal into a more readily interpreted spectrum of frequency versus amplitude. This spectrum communicates the fractional

contribution of each frequency component to the change in the signal over time. At low field strengths, where both signal-to-noise (S/N) and frequency resolution are poor, NMR relaxometry has emerged as a powerful tool to characterize complex materials and mixtures.[1,2] In NMR relaxometry, the measured non-oscillatory time domain signals damp or decay as a function of time. Non-linear least squares (NLLS) regression to a defined set of damped exponential functions, as well as the inverse Laplace transform (ILT) with variable regularization criteria, have been used in an effort to make relaxation “spectra” of relaxation times.[3] These graphs of decay time constant versus amplitude are used to characterize mixtures at low field, much like frequency resolved NMR spectra are used at high field to infer chemical structure.

The matrix pencil method (MPM) [4-6] provides an alternative way to estimate the decay constants for multi-exponential NMR relaxometry signals produced by complex mixtures. The MPM is rapid, accurate, and well suited to operate in the low S/N regime. Unlike the ILT, this implementation of the MPM produces delta function-like peaks that can be used to construct distributions where the peak width unambiguously communicates uncertainty in the central values of the measured constants. Rather than using NLLS to fit a set of a pre-supposed number of exponentials or an integral transformation like the ILT, the MPM relies on an interesting property of a uniformly sampled exponential decay that can be extended to multi-exponential signals with linear algebra. To appreciate this property, consider a simple single exponential signal $f(t) = \exp(-Rt)$ that decays at the rate, R , as a function of the time, t . The MPM begins by separating the data, sampled at intervals Δt , into two point-shifted arrays $f_1((i-1)\Delta t) = f((i-1)\Delta t)$ and $f_2((i-1)\Delta t) = f(i\Delta t)$. The two point-shifted arrays are equated in a so-called “matrix pencil” as $f_2 = zf_1$ and the scaling factor z is determined. Since the uniformly sampled data in this example corresponds to a single exponential $f((i-1)\Delta t) = (\exp(-R\Delta t))^{i-1}$, $z = \exp(-R\Delta t)$ solves the generalized eigenvalue problem $f_2 = zf_1$ at each point and provides the decay rate $R = -\log(z)/\Delta t$. This manuscript considers the extension of this basic idea to damped multi-exponential signals using linear algebra powered by singular value decomposition (SVD).

NMR relaxometry signals establish a platform for testing the performance of the MPM in a variety of magnetic field environments and with an array of samples, from simple to complex. This performance is corroborated in all cases by direct comparison to results obtained from the benchmark relaxometry data processing standard, the ILT. Ultimately, these results provide an avenue to explore the usefulness of the MPM in NMR relaxometry and the role of a suite of inversion modalities in quantifying complex system dynamics.

4.2 Theory

The goal of this section is to provide the reader with a working knowledge of the MPM approach, how to use it to obtain fundamental constants from relaxation data, and how it differs from – and in many cases is more useful than – the ILT. For a more intimate mathematical understanding of the MPM and SVD, the reader may consult refs. 4 and 5.

4.2.1 *The Inverse Laplace Transform*

Currently, the benchmark standard signal processing technique for exponentially decaying NMR relaxometry data is the Fredholm integral approach [7], broadly referred to as the ILT. In this method, the measured one-dimensional (1D) data array, $f(t)$, is viewed as the Laplace transform of a distribution of relaxation rates $P(R)$ as

$$f(t) = \int_0^{\infty} P(R)e^{-Rt} dR. \quad (4.1)$$

Therefore, performing the inverse transform yields $P(R)$ as the distribution function of sample relaxation rates.

A great deal of superb work has been devoted to establishing ways of applying the ILT to NMR relaxometry.[7-9] Unfortunately, though, this approach remains a mathematically ill-posed problem. The problem is ill-posed because the sets of closely related exponential curves used in the ILT are nearly linearly

dependent, so many highly disparate, but equally valid distributions solve Eq. (4.1). In order to convert to a well-posed inverse problem, ILT algorithms impose regularization constraints, which limit the space of acceptable solutions. Because these regularization constraints are mathematically convenient but not physically or statistically meaningful, they introduce ambiguities into the meaning of the computed result. Moreover, the ILT is computationally expensive, as the matrix regularization generally needed to successfully invert the data array requires a considerable amount of time.

4.2.2 *The Matrix Pencil*

The goal of the MPM is to formulate a generalized eigenvalue problem from an array of data that displays first order relaxation. To apply this approach, the NMR data must be sampled or resampled at regular intervals, Δt , and expressed as an $n \times m$ two-dimensional (2D) array or matrix, \underline{Y} . The matrix elements of \underline{Y} , $Y[i,j] = f((i-1)\Delta t_1, (j-1)\Delta t_2)$, are simply elements of the measured data matrix $f(t_1, t_2)$ at the times $t_1 = (i-1)\Delta t_1$ and $t_2 = (j-1)\Delta t_2$ in a 2D experiment. For a 1D experiment, the matrix \underline{Y} is a symmetrically incremented Hankel or Toeplitz matrix formed from the measured data vector $f((i-1)\Delta t)$. When written in this manner, it should be clear that $Y[l,i] = Y[i,l] = f((i-1)\Delta t)$. The elements of successive rows and columns in this type of matrix are shifted from each preceding row and column. A consequence of constructing \underline{Y} in this way is that the elements in the rows and columns in the 1D case are indexed to the same Δt value, whereas in the 2D case, the same elements can be indexed to different values, Δt_1 and Δt_2 , as determined by experimental parameters.

In order to create the eigenstructure necessary for the MPM, a matrix pencil is formed by windowing \underline{Y} in each dimension to construct submatrices \underline{Y}_1 and \underline{Y}_2 . The pair of matrices that appear together in a generalized eigenvalue problem is defined as a matrix pencil. These submatrices are constructed by removing either the last column and row or the first column and row of the $n \times m$ matrix \underline{Y} as

$$\underline{Y}_1 = \begin{pmatrix} Y[1,1] & \dots & Y[1,m-1] \\ \vdots & \ddots & \vdots \\ Y[n-1,1] & \dots & Y[n-1,m-1] \end{pmatrix} \quad (4.2)$$

and

$$\underline{Y}_2 = \begin{pmatrix} Y[2,2] & \dots & Y[2,m] \\ \vdots & \ddots & \vdots \\ Y[n,2] & \dots & Y[n,m] \end{pmatrix}. \quad (4.3)$$

It can be noted that, for the 1D case, $n = m$. The \underline{Y}_1 and \underline{Y}_2 submatrices are used to construct a matrix pencil

$$\underline{Y}_2 \bar{p}_i - z_i \underline{Y}_1 \bar{p}_i = 0, \quad (4.4)$$

where p_i is an eigenvector and z_i is the corresponding eigenvalue. This equation can be rearranged to

$$(\underline{Y}_1^{-1} \underline{Y}_2 - z_i E) \bar{p}_i = 0 \quad (4.5)$$

using the inverse \underline{Y}_1^{-1} and the identity matrix E .

Provided that \underline{Y}_1^{-1} can be defined in the 1D case, z_i immediately reports the decay rates R_i of the measured decay transient as $z_i = \exp(-R_i \Delta t)$. Thus, for spin lattice, longitudinal T_1 or spin-spin, transverse T_2 relaxation, $T_1^{(i)} = \Delta t / \log(z_i)$ and $T_2^{(i)} = \Delta t / \log(z_i)$. For diffusion measured with a pulsed gradient spin echo (PGSE) pulse sequence, $D_i = \log(z_i) / [\gamma^2 \delta^2 (\Delta - \delta/3) \Delta G^2]$, where D_i is the diffusion coefficient for the i^{th} component, γ is the gyromagnetic ratio, Δ is the time delay between gradient pulses, δ is the gradient pulse length and ΔG^2 is the incremental change in gradient strength squared that is used in the MPM in direct analogy to Δt . [10]

In most cases, the inverse matrix \underline{Y}_1^{-1} cannot be calculated because it may not be square with $n \neq m$, and because the number of physically justified components will usually be less than the number of rows or columns. The pseudoinverse of \underline{Y}_1 can be defined as

$$\underline{Y}_1^\dagger = \underline{V} \cdot \underline{\zeta}^{-1} \cdot \underline{U}^T \quad (4.6)$$

where the matrix of right singular vectors \underline{V} , the transposed matrix of left singular vectors \underline{U}^T , and the diagonal inverse spectral matrix $\underline{\zeta}^{-1}$ are invertible and directly obtained from the SVD of the matrix \underline{Y}_1 as

$$\underline{Y}_1 = \underline{U} \cdot \underline{\zeta} \cdot \underline{V}^T. \quad (4.7)$$

Since \underline{Y}_1 is an $(n-1) \times (m-1)$ dimensional matrix where n and m are set by the dimensionality of the original data matrix \underline{Y} , the unitary matrices of left and right singular vectors \underline{U} and \underline{V}^T are $(n-1) \times p$ and $p \times (m-1)$ dimensional with p being the reduced dimensionality of the diagonal spectral matrix $\underline{\zeta}$ of singular values. The dimensionality p represents the number of significant singular values found with SVD and also the number of unique eigenvalues z_i determined from Eq. (4.5) by using Eq. (4.6) with the solutions for \underline{U} , \underline{V}^T , and $\underline{\zeta}$ obtained from Eq. (4.7).

The $p \times p$ dimensional signal amplitude matrix \underline{A} can be obtained in two ways. The first uses the solutions for \underline{U} and \underline{V}^T from Eq. (4.7) along with the submatrix \underline{Y}_2 to provide

$$\underline{A} = \underline{U}^T \cdot \underline{Y}_2 \cdot \underline{V}. \quad (4.8)$$

The second approach applies a similar transformation of \underline{Y}_2 but instead constructs a pair of left and right Vandermonde matrices element-wise by taking powers of the eigenvalues determined from Eq. (4.5) as

$$\underline{Z}_L[k, \ell] = (z_k)^{\ell-1} \propto \underline{U}^T[k, \ell] \quad \text{and} \quad \underline{Z}_R[\ell, k] = (z_k)^{\ell-1} \propto \underline{V}[\ell, k] \quad (4.9)$$

where the subscripted L and R denote usage for left and right multiplication on \underline{Y}_2 , respectively. The damped form for the $n \times m$ MPM-developed data matrix \underline{Y}^{MPM} becomes clear when it is formulated directly from the Vandermonde matrices. In terms of the matrix elements of \underline{A} , the 2D matrix elements of \underline{Y}^{MPM} are

$$Y^{MPM}[i, j] = \sum_{k,q=1}^p A[k, q] z_k^{i-1} z_q^{j-1}. \quad (4.10)$$

In the case where \underline{Y} is derived from 1D data, this equation can be used to construct the elements for a comparative MPM solution as

$$f^{MPM}((i-1)\Delta t) = \sum_{k,q=1}^p A[k, q] z_k^{i-1}. \quad (4.11)$$

4.2.3 MPM Implementation

The MPM can be used in a straightforward way to determine the number of decay constants present in a damped, transient 1D or 2D signal, as well as their relative contributions and values. The practical application of the algorithm involves four steps, namely: 1) construction of data matrices and sub-matrices; 2) application of SVD to the created matrices; 3) obtention of the optimal number of components that adequately represent the data and reduction of dimensionality, and 4) MPM calculation to obtain eigenvalues and amplitudes. Each step is explained in detail below.

First, the data matrix \underline{Y} and the submatrices \underline{Y}_1 and \underline{Y}_2 are constructed from the measured data. Second, SVD is performed on \underline{Y}_1 to obtain \underline{U} , \underline{V}^T , and the $p \times p$ dimensional spectral matrix $\underline{\xi}$. Singular value matrix decomposition of a raw signal is a robust tool for isolation of the spectral components of

mixtures. The MPM employs this procedure to detect the optimal number of unique components in a signal by reconstructing a decay curve with a varying number of SVD components.

The optimal number of components is chosen in the third step, in which the dimensionality of ξ is reduced by finding a subset of the p components of ξ that adequately describe Y_1 . This involves removing elements of the diagonal spectral matrix ξ while concomitantly removing the appropriate rows and columns of U and V^T to insure that the matrix product in Eq. (4.7), with a reduced dimensionality spectral matrix ξ , can be performed to yield an estimated spectral matrix Y_1^{est} . The elements of ξ that are removed are either complex numbers or are so small that there is little effect on Y_1^{est} , as verified by calculating the chi-squared statistic

$$\chi_1^2 = \frac{1}{(n-1)(m-1)} \sum_{i=1}^{n-1} \sum_{j=1}^{m-1} (Y_1[i, j] - Y_1^{est}[i, j])^2 \quad (4.12)$$

for the residuals between the reconstructed curve and the raw signal. Error analysis can also be accomplished by reconstruction of a signal based on amplitudes and relaxation rate constants estimated by the MPM. Typically, the elements removed from ξ do not contribute to the damping behavior of the signal in any significant way and correspond largely to noise. The truncation of ξ is facilitated by knowledge that the desired components must be real-valued and cannot reasonably decay much faster than $1/\Delta t$. Removal of the components that fail to meet these criteria tends to yield the best set of components, and the criteria can be imposed automatically in software. Typically, the largest number of singular values that does not yield unphysical components is the best choice; however, for precious or singular samples, or in the presence of legitimate decay envelope modulations, this step must be more closely supervised. An essential feature of the MPM is that it provides a list of intensities (and phases) and decay rates (and frequencies). With this list, the user may pick any features to keep or reject, and this choice is imposed in the third step.

For the fourth step, the reduced dimensionality of $\underline{\zeta}$, \underline{U} and \underline{V}^T propagates through the MPM calculation in Eqs. (4.5) and (4.8), and yields a similarly reduced number of eigenvalues z_i and signal amplitudes $A[k,q]$. If the original data is 2D, the data matrix \underline{Y} is transposed and these four steps are repeated to analyze the indirect dimension. Depending on the pulse sequence, the eigenvalues are directly related to T_1 , T_2 and D_i as described above, and the $A[k,q]$ report the fractional contribution of the given decay components to the overall measured signal.

4.2.4 Error Analysis

The MPM analysis described above provides a list of eigenvalues \underline{z} and amplitudes \underline{A} that are used in Eq. (10) to construct an estimate of the full data matrix \underline{Y}^{MPM} . A graph of decay constant versus amplitude can be created by taking the decay constants calculated from z_k and z_q as the center of a multidimensional Gaussian peak with amplitude $A[k,q]$. The width of this Gaussian peak is calculated from the appropriate diagonal elements of the covariance matrix $\underline{\Sigma}$ of decay rates and signal amplitudes. The matrix elements of the Hessian matrix

$$H[k,q] = \frac{\partial^2}{\partial \xi_k \partial \xi_q} \chi^2 \quad (4.13)$$

are used to calculate the covariance matrix in the usual way as $\underline{\Sigma} = \chi^2 H^{-1}$ [11]. The ξ_k and ξ_q parameters refer to either the decay constants T_1 , T_2 and D_i or the amplitudes $A[k,q]$. The chi-squared statistic is calculated from the matrix elements of \underline{Y} and \underline{Y}^{MPM} in Eq. (4.10) as

$$\chi^2 = \frac{1}{n \times m} \sum_{i=1}^n \sum_{j=1}^m (Y[i,j] - Y^{MPM}[i,j])^2 \quad (4.14)$$

where n and m pertain to the original size of the data matrix. By treating the MPM results in this way, the constructed Gaussian peak not only communicates the MPM-determined decay constant value from the location of the peak maximum but also the uncertainty in that decay constant via the peak width.

It is worth noting that this approach only works under the assumption of Gaussian uncertainties. Monte Carlo simulations and additional statistical testing, which will be included in a future publication, demonstrate that the uncertainties are quite markedly Gaussian, as long as the uncertainties are less than the distances separating the rate constants. However, when the uncertainties are greater than or equal to the resolution of the rate constants, the shapes become associated with each other and lose their Gaussian character. For a generalized approach to parameter estimation, in these challenging cases, the MPM results may be used as an initial guess in subsequent least-squares fitting. This approach consistently yields the best estimate of the interdependent parameter set that describes the signal.

4.3 Experimental

All chemicals were obtained from Sigma-Aldrich with the exception of olive oil, which was purchased from Trader Joe's and used as received. A standardized equal volume mixture of olive oil and 3.12 mM CuSO₄ in water was prepared.

A 43.7 MHz ¹H Larmor frequency, 1.01 Tesla Aspect Imaging M100 magnet interfaced to a Tecmag Apollo spectrometer with a maximum gradient strength of 0.24 T/m was used to explore the relaxometry properties of the olive oil/water mixture. The 60 mm diameter radio frequency (rf) coil inside of the NMR probe allowed large sample volumes to be studied. Typically, $\pi/2$ rf pulse lengths of 30 μ s with 7 W of applied rf power were used. A saturation recovery pulse sequence with 100 indirect dimension time points and a maximum delay time of 2.5 s was used to measure T_1 . For T_2 measurement, a Carr-Purcell-Meiboom-Gill (CPMG) pulse sequence was used with 1500 echoes and a delay of $\Delta t = 1$ ms between the π rf pulses. A pulsed gradient spin echo (PGSE) pulse sequence with $\delta = 16$ ms field gradient

pulses separated by $\Delta = 35$ ms was used to measure diffusion coefficients D_i in 140 diffusion gradient steps. Two-dimensional T_1T_2 and T_2T_2 correlations were performed with saturation recovery–CPMG and CPMG–CPMG pulse sequences [12] using the same parameters applied in the 1D cases. The mixing time in the T_2T_2 experiment was set to 37 ms.

All calculations and MPM data processing were accomplished with Matlab (Mathworks, Natick, MA). All comparison ILT relaxometry results were generated using Prospa, the commercially available ILT software from Magritek (Malvern, PA.).

4.4 Results and Discussion

In the limit of zero noise, the MPM provides an analytically exact, closed-form solution to the problem of multi-exponential decomposition. This is demonstrated in Fig. 4.1 with model data in (a) simulated using

$$f((i-1)\Delta t_1, (j-1)\Delta t_2) = \sum_{k,q=1}^p A[k,q] (e^{-\frac{\Delta t_1}{T_1[k]}})^{i-1} (e^{-\frac{\Delta t_2}{T_2[q]}})^{j-1} \quad (4.15)$$

where $A[k,q]$ represents the peak amplitudes and allows for exchange between populations. In the limit of no exchange, \underline{A} is diagonal with p positive, non-zero elements. For fast exchange, or when the exchange rate exceeds the difference between spin relaxation rates, \underline{A} has just one positive, non-zero element located on the diagonal. Slow to intermediate exchange introduces $k \neq q$ non-zero elements in \underline{A} . As evidenced in Fig. 4.1(b), the MPM processed result reproduces the input parameters exactly, including the exchange between relaxation modes. This ability of the MPM to precisely model diverse arrays of data also enables it to handle noisy relaxometry signals by acting as a robust filter similar to SVD.

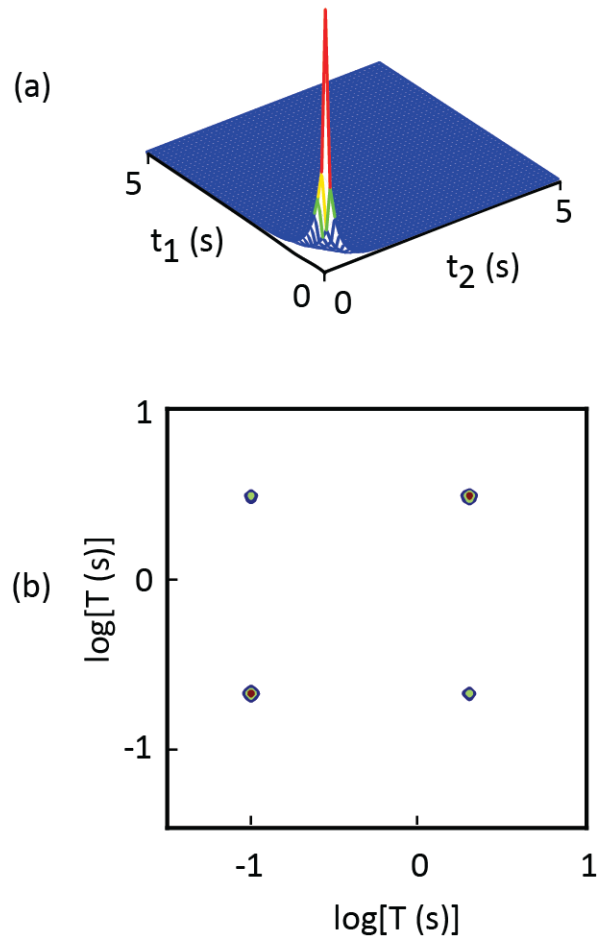


Figure 4.1. (a) Noise-free data surface calculated from Eq. (15) with $T_1[1] = 3$ s, $T_1[2] = 0.2$ s, $T_2[1] = 2$ s, $T_2[2] = 0.1$ s, $A[1,1] = A[2,2] = A[1,2] = A[2,1] = 1$. (b) The plot produced from MPM processing that reproduces the T_1 , T_2 , and $A[k,q]$ values exactly. The 2D contour peak width in this plot is artificial. The width is included to represent the data in a 2D graph and is 0.06 % of the full bandwidth.

A test sample composed of equal volumes of olive oil and 3.12 mM CuSO₄-doped water was chosen to study the initial performance of the MPM in standard 1D and 2D relaxometry experiments. The T_1 , T_2 , and D values were 198 ms, 84 ms, and 1.2×10^{-10} m²/s for the olive oil, while for the CuSO₄-doped water sample they were 515 ms, 198 ms, and 5.3×10^{-8} m²/s, respectively. A mixture of the two substances was used because they are readily obtained, allowing anyone with an NMR instrument to accomplish similar benchmark comparisons. Moreover, the two-layered sample is easy to prepare because the oil and water are not miscible, and therefore provide two distinct values each for T_1 , T_2 , and D to challenge the resolution of data processing techniques in the limit that these values become similar. In the case of spin relaxation, this can be regulated by controlling the concentration of CuSO₄ in water.

Figure 4.2 compares the performance of the MPM and ILT data processing approaches for the measurement of T_2 , T_1 and D values in (a), (b) and (c) respectively, for the oil and CuSO₄-water system. The data that generated the plots in Fig. 4.2(a) – (c) were obtained from the respective CPMG, saturation recovery, and PGSE pulse sequences. Two facts emerge from a comparison of the MPM (left) to the ILT (right) results in Fig. 4.2. First, the MPM provides better resolution than the ILT. This observation is not due to any artificial data handling, as the peak width obtained by MPM reflects the true error in the parameter estimate calculated by the Hessian analysis described in Sec. 4.2.4. For example, the T_2 values shown in Fig. 4.2(a) are 198 ± 24 ms and 115 ± 3 ms from the MPM and 190 ± 45 ms and 98 ± 39 ms for the ILT. The greater uncertainty in the ILT-derived T_2 values leads to the broader responses in the figure and, thus, decreased resolution in comparison to the MPM. It is true that the broad ILT lines can be artificially narrowed with an alternative choice for the regularization parameter α . However, this risks introducing computational instability and often relies on prior knowledge of the sample. In all ILT results reported here, the value of α was selected by optimization of the χ^2 statistic for the fit parameters with respect to the data, as described in [13]. In all of the cases considered here, this procedure produced an α value slightly

greater than, slightly less than or equal to 10^{10} . Therefore, to remain consistent amongst all of the ILT results presented here, $\alpha = 10^{10}$ was used.

The second fact that emerges from Fig. 4.2 is that the MPM analysis of the saturation recovery data shown in Fig. 4.2(b) produces two peaks appropriately labelling the distinct T_1 values for the separate substances while the ILT yields just one. Changes to α in the ILT analysis of this data set does not reintroduce these two peaks. To evaluate the accuracy of MPM and ILT results, NLLS fitting was applied to all benchmark and exploratory 1D studies performed to date. The MPM treatment typically produces constants within 5 % of the NLLS value, while the ILT values may differ by up to an order of magnitude.

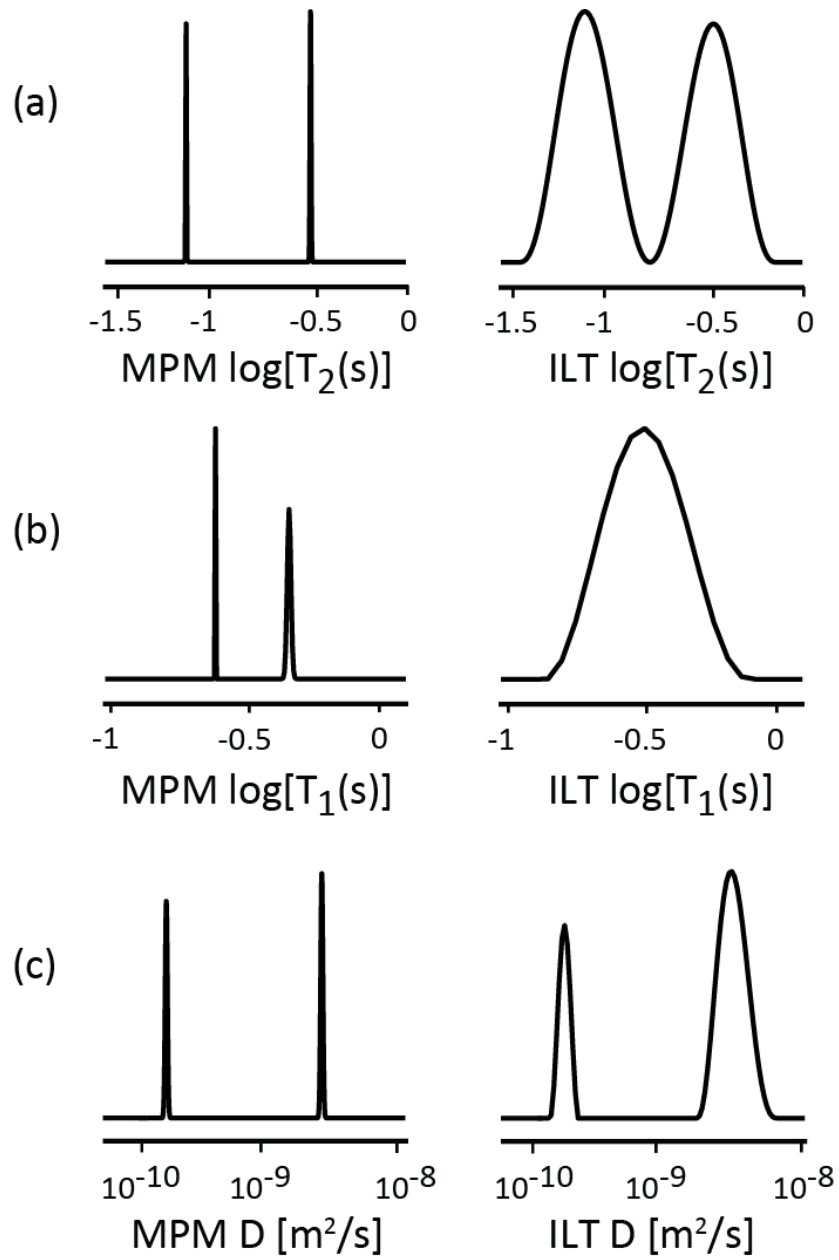


Figure 4.2. Standard 1D graphs of processed decay constants versus amplitude obtained from the olive oil/water mixture. The CPMG, saturation recovery, and PGSE pulse sequences were used to create data that produced the graphs in (a), (b), and (c), respectively. The left column summarizes the MPM performance, while the right column shows the ILT results.

A comparison of the MPM and ILT approaches to processing typical multidimensional relaxometry data is shown in Fig. 4.3(a) and (b) for data obtained from T_2T_2 and T_1T_2 correlations respectively. Similar contrasts emerge from this comparison, specifically related to linewidth and the appearance of artifacts in the 2D relaxometry correlation plots. The linewidth, judged from the size of the similarly plotted contours, from maximum intensity to half intensity in ten increments, is always significantly less in the MPM cases. This suggests that error was correctly included in the MPM estimates, as this approach has inherently higher resolution than the ILT. However, this immediate conclusion is based on the flawed interpretation that broad ILT linewidths solely reflect parameter uncertainty. Such an interpretation is not precisely true, as the ILT also reports a physical distribution of time constants by inverting Eq. (4.1) to solve for $P(R)$. Moreover, as mentioned above, the linewidth of the ILT is also influenced by the α smoothing parameter. This demonstrates the difficulty associated with disentangling true parameter error in an ILT analysis from the actual distribution of relaxation rates across a range of parameter values [8]. This issue is relevant in low-field NMR, particularly given the greater field inhomogeneity encountered when using single sided magnets equipped with surface coils.

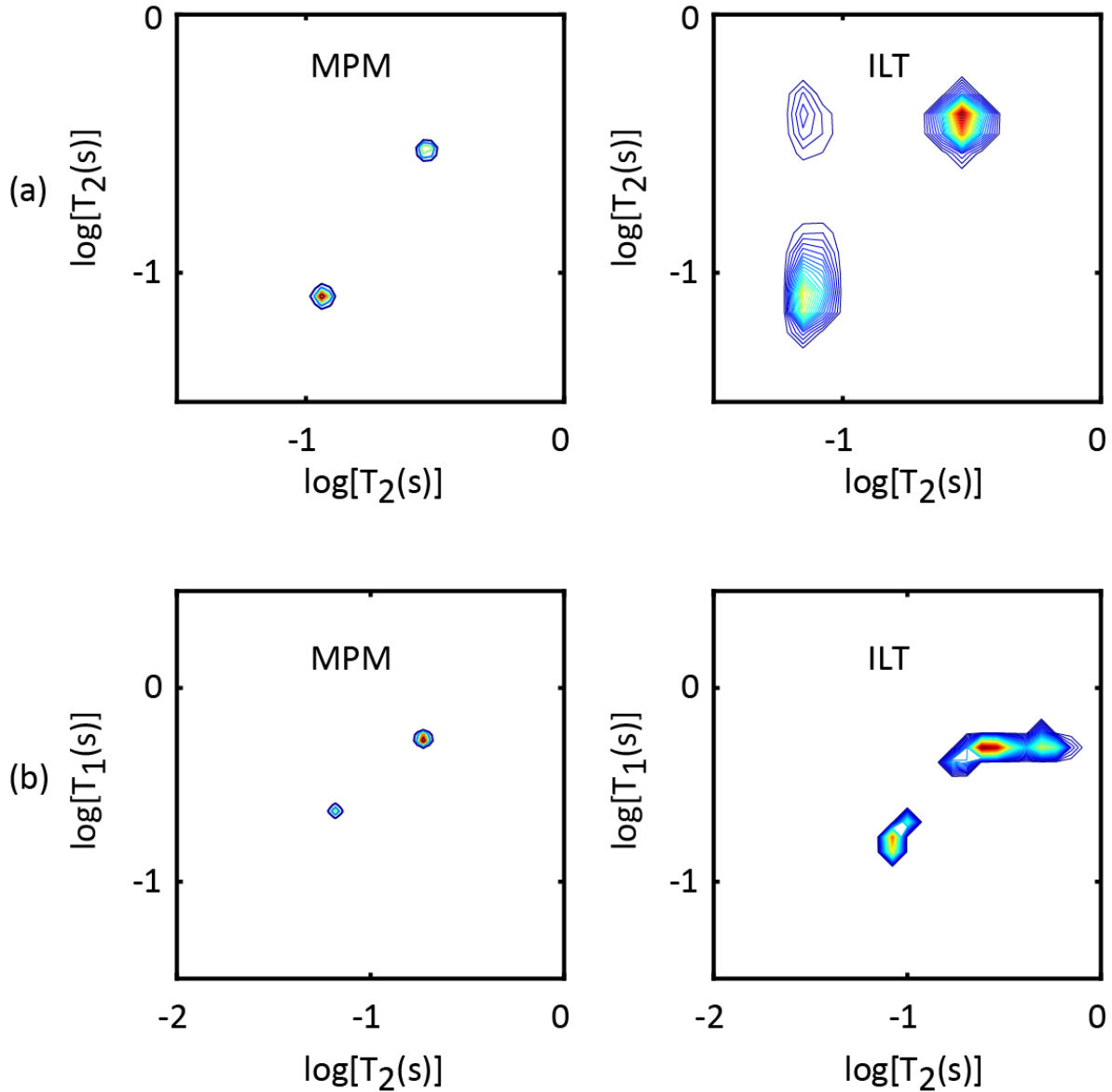


Figure 4.3. Standard 2D contour plots correlating measured decay constants obtained from the olive oil/water mixture 2D relaxometry signals. The CPMG-CPMG T_2T_2 and the CPMG-saturation recovery T_1T_2 pulse sequences were used to create the data that produced the contour plots in (a) and (b), respectively. Again, the left column summarizes the MPM performance while the right column shows the ILT results.

It is worth commenting on the fact that the MPM does not handle truly continuous distributions of relaxation rates gracefully. It automatically, by prior assumption, models the data as a discrete sum. For continuous distributions, the MPM finds a parsimonious set of discrete components that best models the distribution. Nonetheless, a continuous distribution can be modeled to high precision with a very small number of discrete components. This approach may be useful in the measurement of pure systems as well as systems with high heterogeneity, such as biological tissues [3,14-18], whose continuous spectra are informative yet difficult to interpret as they often lack sharp and clear separation of spectral components. However, this specific application of the MPM is yet untested. Ultimately, any fitting approach like the MPM or L1 regularization that models the data as a sum of discrete exponentials is limited in its ability to describe truly heterogeneous systems such as biomaterials. The discrete nature of this sum leads to a delta function-like appearance of the corresponding component distribution. Conversely, it is often difficult to interpret the linewidth in a continuous distribution spectrum obtained by complementary inversion approaches, as the linewidth reflects a combination of error and underlying system heterogeneity whose deconvolution is problematic. Without prior knowledge of a system, it is impossible to conclude directly that any one fitted distribution is superior. Rather, the most useful conclusions may be drawn by comparison of the results from many techniques, through which their complementarity may be leveraged to enhance the statistical rigor of data analysis. In this way, it is possible to not only provide a robust and compelling evaluation of data, but also to maximize the system-specific information that is extracted from the raw signal.

The ILT linewidth is also closely tied to the choice of the α regularization parameter. For noisy data, it is often necessary to choose a large α value to allow data matrix inversion. This choice causes the results to appear as classic “oversmoothed” spectra, where the peak width is primarily associated with error introduced in the algorithm. It is this oversmoothing effect that leads to the broad ILT results shown in Figs. 4.2 and 4.3. The ILT results in Fig. 4.3 also have off-diagonal correlation responses or artifacts that are not present in the MPM analysis. In this case, exchange peaks are not expected as the two sample

components are immiscible. Additionally, the center positions of the contours in both Figs. 4.3(a) and (b) are slightly different in the two data processing approaches. As in the case of the benchmark 1D study described above, an NLLS analysis of the raw 2D data produced time constant values within 5 % of the MPM results.

For the ILT, L2 regularization is often used to invert the Fredholm equation, generally implemented with Tikhonov regularization and/or ridge regression models that add a squared magnitude coefficient penalty term to scale solutions that do not fit given constraints. Another approach using L1 regularization is commonly implemented by Least Absolute Shrinkage and Selection Operator (Lasso) regression or the fast iterative shrinkage-thresholding algorithm (FISTA) [13,19,20]. Here an absolute value magnitude coefficient penalty term is used. The Lasso or FISTA approach shrinks the coefficients of the less significant features to zero, thus removing some spectral features entirely resulting in delta function-like results similar to the MPM. However, the outcome of this approach can be a loss of information relating to the system heterogeneity that cannot be accessed for comparison to the MPM. For this reason and because L1 regularization methods are not widely available, the L2 regularization approach used in Prospa was chosen to perform benchmark comparisons with the MPM. One major benefit of the MPM in comparison to inversion methods based on regularization – either L1 or L2 – is computational ease. As can be seen in the MPM algorithm included in the Appendix, the steps required to perform the MPM are brief (i.e., formation of element-shifted submatrices from the data array, and then finding eigenvalues), and use standard algorithms in Matlab and Python.

The 1D and 2D relaxometry results in Figs. 4.2 and 4.3 suggest that the MPM produces fewer artifacts and narrower lines than the ILT, as well as accurate peak positions with widths that directly communicate parameter uncertainty. In order to explore whether these data processing improvements were merely the result of choosing a well-behaved benchmark sample with high S/N, two additional real-world examples from entirely different scientific applications in two dramatically different magnets were considered.

The first example involves using NMR relaxometry at a 250 MHz ^1H Larmor frequency to study the dynamic nanoscale heterogeneity of a physically cross-linked solvent-polymer system near the glass transition temperature.[21] This example has application in many industrial, biomedical, and environmental systems, as the drying of solvent-polymer solutions is a key process undergone by paints, dyes, and spray drying materials in food and pharmaceutical processing [22-24], and is important in energy materials [25] and many biomedical systems such as wound healing and drug delivery.[26] The ability to resolve the components from multidimensional relaxometry experiments enables the elucidation of rotational and translational dynamics of a system. An experimental understanding of rotational and translational dynamics yields information about domains associated with regions of solid-like and liquid-like character and the cross-link density of a polymer network respectively. This information is used to report quantitative length and timescales of nanoscale heterogeneity in the drying solvent polymer system. The results shown in Fig. 4.4(a) repeat the ILT analysis of raw data obtained for a drying solvent polymer system originally shown in Fig. 4.2(a) of ref. 21. The MPM analysis of the same data set produces Fig. 4.4(b), which is more resolved and with contour maxima in slightly different positions in comparison to Fig. 4.4(a). Neither the increased resolution, nor the slight peak shifts, change the interpretation of the relaxation results and their relevance towards characterizing the drying solvent polymer system. Rather, the increased resolution will allow a more straightforward characterization of challenging samples, while at the same time enabling more accurate time constants to be obtained.

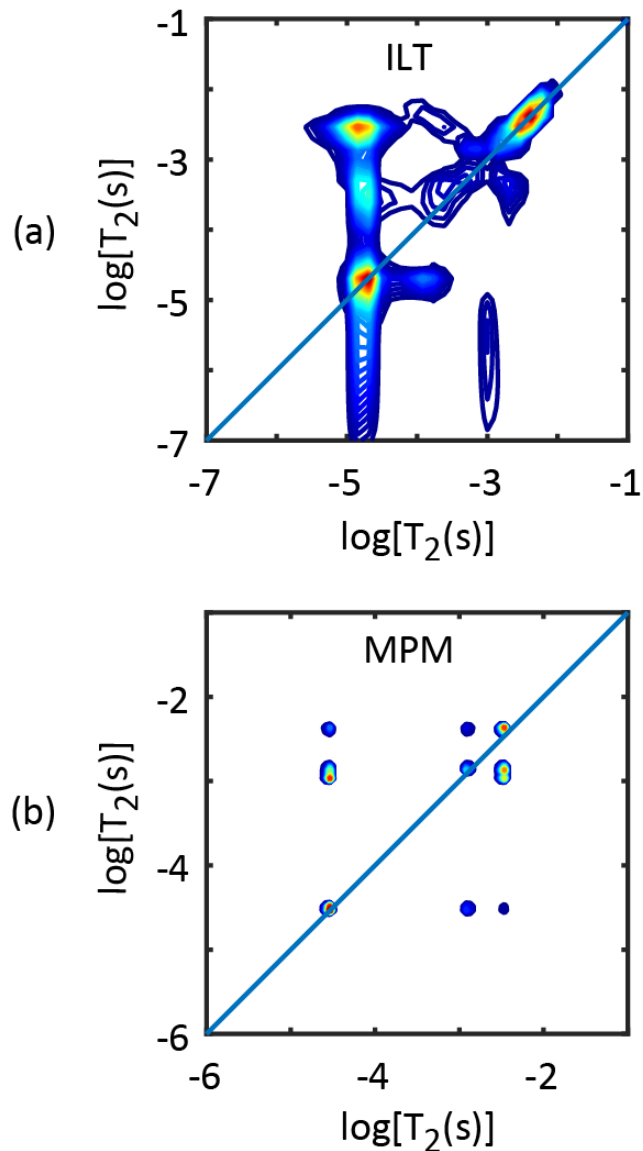


Figure 4.4. Comparison of ILT (a) and MPM (b) treated T_2T_2 correlation data obtained from an extensive data set studying glass drying dynamics in a solvent-polymer weak gel. The sample composition is 7% wt acetone and 93% wt hydroxypropyl methylcellulose acetate succinate. A 5 mm diameter rf coil with $3.5 - 7 \mu\text{s}$ $\pi/2$ rf pulses using 100 W of applied rf power was mounted inside of a 5.88 T magnet interfaced to a Bruker Avance III 250.12 MHz ^1H Larmor frequency spectrometer and used to generate the raw T_2T_2 data. The mixing time was 1 ms and a Diff30 coil was used to establish a 17.82 T/m field gradient. Further sample and pulse sequence details can be found in ref. 21.

The second example considers the application of chemical shift resolved PGSE pulse sequences, or diffusion ordered spectroscopy [27], at a 700 MHz ^1H Larmor frequency in the characterization of the dynamics of a mixture resulting from the enzymatic digestion of $\alpha(2-8)$ polysialic acid. Such mixtures are relevant to the study and development of polysaccharide-based vaccines. Characterization of vaccine components, present as mixtures, is critical and is currently difficult to accomplish. The determination of the D_i values for these components can be related to molecular size and used to simplify complex, overlapping 1D spectra by extracting subspectra of conjugate vaccines, as a function of D . Thus, NMR-based diffusion measurements can be used to characterize glycan structure of different vaccine components. This characterization is crucial, as the structures of glycans are immediately tied to their function and ability to interact with antibodies and their size may be tied to immunogenicity.[28-31] A typical NMR spectrum is shown at the top of Fig. 4.5. This spectrum was divided into seven regions, from high to low ^1H chemical shift, and the integrated area of these regions was tracked in the PGSE experiment as a function of the pulsed field gradient strength. The MPM and ILT analysis of the integrated signal decays in those seven separate regions is respectively shown on the left and right in Figs. 4.5(a) – (g). The MPM analysis (left), once again, provides narrower and in some cases slightly shifted responses in comparison to the ILT (right). The discrepancy between peak positions provided by the MPM and ILT processing is particularly notable in Fig. 4.5(d), where the ILT result differs from the MPM value by almost an order of magnitude. Again, NLLS treatment of the data yields constants within 5 % of the MPM values reported on the left in Figs. 4.5(a) – (g), suggesting a higher level of accuracy in the MPM results.

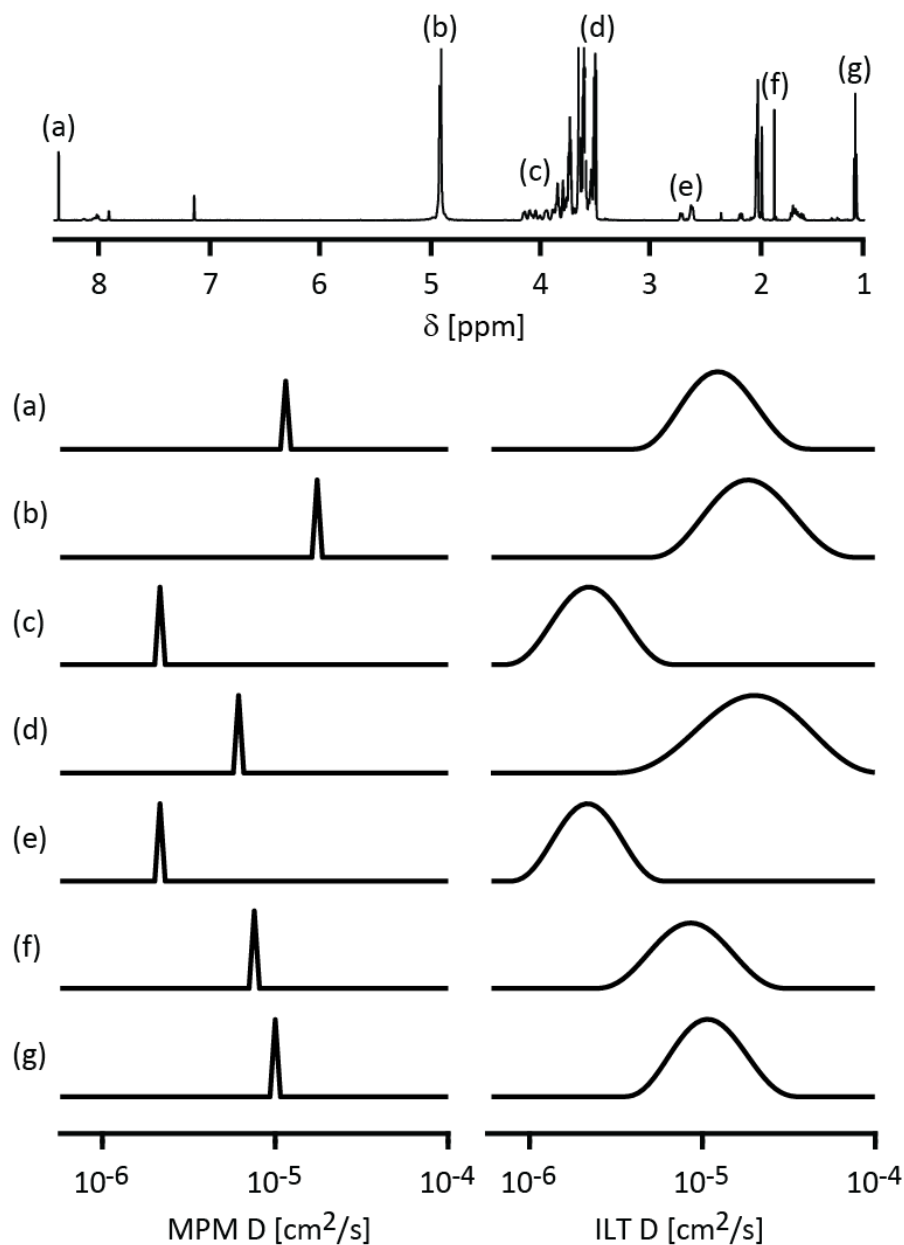


Figure 4.5. Comparison of MPM (left) to ILT (right) treated high resolution PGSE data obtained from a mixture produced from an enzymatic hydrolysis of α 2-8-linked polysialic acid (pSia). The mixture contains different oligomers of digested pSia, tris buffer and other small molecules as evidenced by the high resolution ^1H NMR spectrum shown at the top, which corresponds to the first transient of a diffusion ordered 2D experiment. A 16.45 T, 700 MHz ^1H Larmor frequency Bruker AV III HD NMR instrument equipped with an XYZ-gradient CryoProbeTM was used to generate the raw PGSE data at 283 K with a 0.524 T/m maximum pulsed field gradient. The hydrolysis reaction buffer contained 50 mM Tris and 100 mM PBS at pH 8. The signals at 2.0 ppm correspond to the sialic acid methyl proton from the N-Acetyl group, at 2.2 ppm and 2.6 ppm to the equatorial H3 proton, and at 1.6 ppm to the axial H3 protons of sialic acid. Further details can be found in ref. 28.

Ultimately, the usefulness of NMR is limited by the ability of an algorithm to extract information from a recorded signal. Therefore, it is essential to develop data processing methods that produce narrow lines, minimal error, and accurate and reliable results in systems that are currently challenging to study. Based on the performance here, the MPM appears to possess all of these characteristics. Since the MPM is purely linear algebra-based, in the case with no noise shown in Fig. 4.1, the MPM has no error. In comparison to the ILT, the MPM displayed narrower lines in the standard relaxometry experiments in Figs. 4.2 and 4.3. This superb resolution was also present in the case studies of complex materials shown in Figs. 4.4 and 4.5. Additionally, the positions of the peaks reported by the MPM displayed a high degree of accuracy, as confirmed by agreement with NLLS analyses for all cases. The MPM is inherently less prone to artifacts, a feature which is perhaps most evident in the multidimensional data shown in Figs. 4.3 and 4.4. Moreover, the MPM algorithm is typically a factor of 20 times faster than the ILT. The amount of data required to detect a unique decay component with the MPM in comparison to traditional transform methods is useful to consider. For the Fourier transform applied to noise-free data, the Nyquist limit dictates that three points are required to define an exponential or oscillatory curve. Throughout this study, experiment suggests that approximately 10 equally spaced points sampling the fast decay component that uniformly continue until the signal has disappeared into noise are needed for the MPM to reliably detect each component. Finally, the MPM is free and easy to use. A simple Matlab script that creates an exponential decay without noise, applies the MPM, and reports the decay time is provided in the Appendix.

4.5 Conclusion

The power of the MPM is linked to the efficiency of the eigenstructure formulation of an array of data. The time required for MPM data analysis is inconsequential in comparison to the data acquisition time because well-refined linear algebra is implemented in the algorithm in a non-iterative fashion. The size reduction offered by the SVD truncates the data to a dimensionality matching the number of significant components, which also improves algorithm speed. The complexity of the problem framed by the MPM is

further reduced by using unitary matrix transformation when solving for eigenvalues. Moreover, there is no further processing needed after the completion of the MPM algorithm, as the spectral parameters of interest are directly output as an ordered array of scalars and can be immediately used to construct a high resolution spectrum. In contrast, since integral transform techniques yield distribution functions as outputs, they require further processing in the form of peak searching, curve fitting, and intensity integration in order to produce quantitative information. To integrate the MPM with compressed sensing or constrained optimization techniques, non-uniformly sampled data must be linearly resampled to create a constant, uniform time interval increment. This is straightforward and can be accomplished by a wide variety of interpolation algorithms, thus extending the applicability of the MPM to data that has been sampled in any way.

One of the greatest strengths of the MPM in comparison to integral transform techniques is its enhanced resolution in the presence of substantial noise. Resolution is improved because the output parameters are scalars, rather than distributions, and are thus unrelated to spectral bandwidths. While suited to a wide variety of applications, the MPM is perhaps most notably useful for situations with intrinsically low S/N. Indeed, the MPM itself can be used as a noise filter in the style of SVD-based signal reconstruction. The key for widespread future implementation and automation of the MPM is to use it first as a noise filter and second as a parameter estimation tool.

The ability of the MPM to function as both a fitting tool, as demonstrated here, and as a filter, as discussed in a future publication, allow it to perform at the interface between low S/N input and high resolution output. This suggests that the MPM will facilitate the analysis of systems and samples that have previously been inaccessible to NMR relaxometry.

Acknowledgements

The authors thank Dr. Michael McCarthy for his continued inspiration, guidance, support and most importantly for assembling the members of this team. Support from the University of Washington, Center for Process Analysis and Control is gratefully acknowledged.

Appendix

The following Matlab script creates a 200-point single exponential signal array. The data sampling dwell time is $\Delta t = 100 \mu\text{s}$ and the exponential decay constant is $T_2 = 1 \text{ ms}$. The script outputs a plot of the exponential decay and numerical values for the MPM determined signal amplitude and decay constant.

```
%%% Create a noiseless single exponential signal
clear all
timepoints = 200;
T2 = 1e-3; % seconds
dt = 1e-4; % seconds
amp = 1;
data = amp*exp(-(0:timepoints-1)*dt/T2);
plot(data)

%%% Make the input matrix and reduce size with SVD %%%
ncomp = 1;
datamatrix = hankel(data);
[u,s,v] = svd(datamatrix);

for ii = 1:ncomp;
    decaymatrix_svd = u(:,ii)*s(ii,ii)*v(:,ii)';
end

%%% Matrix Pencil estimates of decay constants and amplitudes
for ii = 1:(length(data) - 1);
    d1(ii,:) = decaymatrix_svd(ii,1:(length(data) - 1));
    d2(ii,:) = decaymatrix_svd(ii,2:length(data));
```

```
end
```

```
eigs = eig(pinv(d1)*d2);
```

```
for jj = 1:ncomp;
```

```
    for ii = 1:(length(data)-1);
```

```
        eigvec_left(ii,jj) = real(eigs(jj))^(ii - 1);
```

```
        eigvec_right(jj,ii) = real(eigs(jj))^(ii - 1);
```

```
    end
```

```
    T_mpm(jj) = -dt/log(real(eigs(jj)))
```

```
end
```

```
Amplitude_mpm = pinv(eigvec_left)*decaymatrix_svd(1:(length(data)-  
1),1:(length(data)-1))*pinv(eigvec_right)
```

References

- [1] B. Blumich, J. Perlo, F. Casanova, Mobile single-sided NMR, *Prog. Nucl. Magn. Reson. Spectrosc.*, 52(4) (2008) 197–269.
- [2] R.J.S. Brown, Proton relaxation in crude oils, *Nature*, 189 (1961) 4762.
- [3] R.M Kroeker, R.M. Henkelman, Analysis of biological NMR relaxation data with continuous distributions of relaxation times, *J. Magn. Reson.*, 69(2) (1986) 218–235.
- [4] Y. Hua, T.K. Sarkar, Matrix pencil method for estimating parameters of exponentially damped/undamped sinusoids in noise, *IEEE Trans. Acoust. Speech Signal Process.*, 38(5) (1990) 814–824.
- [5] Y. Lin, P. Hodgkinson, M. Ernst, A. Pines, A novel detection-estimation scheme for noisy NMR signals: Applications to delayed acquisition data, *J. Magn. Reson.*, 128(1) (1997) 30–41.
- [6] V.A. Mandelshtam, H.S. Taylor, A.J. Shaka, Application of the filter diagonalization method to one- and two-dimensional NMR spectra, *J. Magn. Reson.*, 133 (1998) 304-312.
- [7] L. Venkataramanan, Y. Song, M. Hurlimann, Solving Fredholm integrals of the first kind with tensor product structure in 2 and 2.5 dimensions, *IEEE Trans. Signal Process.* 50 (5) (2002) 1017–102.
- [8] Y. Song, L. Venkataramanan, L. Burcaw, Determining the resolution of Laplace inversion spectrum, *J. Chem. Phys.*, 122 (2005) 104104.
- [9] C.L. Lawson, R.J. Hanson, *Solving Least Squares Problems*, Prentice-Hall, Englewood Cliffs, NJ, USA, 1974.
- [10] G.S. Armstrong, N.M. Loening, J.E. Curtis, A.J. Shaka, V.A. Mandelshtam, Processing DOSY spectra using the regularized resolvent transform, *J. Magn. Reson.*, 163 (2003) 139-148.

- [11] H. Neudecker, J.R. Magnus, *Matrix differential calculus with applications in statistics and econometrics*, John Wiley & Sons, New York, 1988.
- [12] P.T. Callaghan, *Translational dynamics and magnetic resonance: principles of pulsed gradient spin echo NMR*, Oxford University Press, Oxford, UK, 2011.
- [13] K.P. Whittall, A.L. MacKay, Quantitative interpretation of NMR relaxation data, *J. Magn. Reson.*, 84(1) (1989) 134–152.
- [14] C. Beaulieu, F.R. Fenrich, P.S. Allen, Multicomponent water proton transverse relaxation and T2-discriminated water diffusion in myelinated and nonmyelinated nerve, *Magn. Reson. Imaging*, 16(10) (1998) 1201-10.
- [15] J. Pfeuffer, S.W. Provencher, R. Gruetter, Water diffusion in rat brain in vivo as detected at very large b values is multicompartamental, *Magma*, 8(2) (1999) 98-108.
- [16] I. Ronen, S. Moeller, K. Ugurbil, D.-S. Kim, Analysis of the distribution of diffusion coefficients in cat brain at 9.4 T using the inverse Laplace transformation, *Magn. Reson. Imaging*, 24(1) (2006) 61-68.
- [17] D. Kim, E.K. Doyle, J.L. Wisnowski, J.H. Kim, J.P. Haldar, Diffusion-relaxation correlation spectroscopic imaging: A multidimensional approach for probing microstructure, *Magn. Reson. Med.*, 78(6) (2017) 2236-2249.
- [18] D. Benjamini, P.J. Basser, Magnetic resonance microdynamic imaging reveals distinct tissue microenvironments, *NeuroImage*, 163 (2017) 183-196.
- [19] A. Reci, A.J. Sederman, L.F. Gladden, Obtaining sparse distributions in 2D inverse problems, *J. Magn. Reson.*, 281 (2017) 188–198.
- [20] X. Zhou, G. Su, L. Wang, S. Nie and X. Ge., The inversion of 2D NMR relaxometry data using L1 regularization, *J. Magn. Reson.*, 275 (2017) 46–54.

- [21] N.H. Williamson, A.M. Dower, S.L. Codd, A.L. Broadbent, D. Gross, J.D. Seymour, Glass dynamics and domain size in a solvent-polymer weak gel measured by multidimensional magnetic resonance relaxometry and diffusometry, *Phys. Rev. Lett.*, 122(6) (2019) 068001.
- [22] T. Okuzono, K.Y. Ozawa, M. Doi, Simple model of skin formation caused by solvent evaporation in polymer solutions, *Phys. Rev. Lett.*, 97 (2006) 136103.
- [23] D.T. Friesen, R. Shanker, M. Crew, D.T. Smithey, W.J. Curatolo, J.A.S. Nightingale, Hydroxypropyl methylcellulose acetate succinate-based spray-dried dispersions: an overview, *Mol. Pharmaceutics* 5 (2008) 1003.
- [24] J.T. Moller, S. Fredsted, A primer on spray drying, *Chem. Eng.*, 116 (2009) 34.
- [25] J.J. van Franeker, M. Turbiez, W. Li, M.M. Wienk, R.A.J. Janssen, A real-time study of the benefits of co-solvents in polymer solar cell processing, *Nat. Commun.*, 6 (2015) 6229.
- [26] J.S. Boateng, K.H. Matthews, H.N.E. Stevens, G.M. Eccleston, Wound healing dressings and drug delivery systems: a review, *J. Pharm. Sci.* 97 (2008) 2892.
- [27] C.S. Johnson, Diffusion ordered nuclear magnetic resonance spectroscopy: principles and applications, *Prog. Nucl. Magn. Reson. Spectrosc.*, 34 (1999), pp. 203-256.
- [28] M.D. Battistel, H.F. Azurmendi, B. Yu, D.I. Freedberg, NMR of glycans: shedding new light on old problems, *Prog. Nucl. Magn. Reson. Spectrosc.*, 79 (2014) 49-68.
- [29] H.F. Azurmendi, J. Vionnet, L. Wrightson, L.B. Trinh, J. Shiloach, D.I. Freedberg, Extracellular structure of polysialic acid explored by on cell solution NMR; *Proc. Natl. Acad. Sci.*, 104 (2007) 11557-11561.
- [30] C. Abeygunawardana, T.C. Williams, J.S. Sumner, J.P Hennessey, Development and validation of an NMR-based identity assay for bacterial polysaccharides; *Anal. Biochem.*, 279 (2000) 226.

- [31] H. Yu, Y. An, M.D. Battistel, J.F. Cipollo, D.I. Freedberg, Improving analytical characterization of glycoconjugate vaccines through combined high-resolution MS and NMR: application to *Neisseria meningitidis* serogroup B oligosaccharide-peptide glycoconjugates; *Anal. Chem.*, 90 (2018) 5040.

5. ESTIMATES OF BLOOD PLASMA WATER CONTENT USING PORTABLE NMR RELAXOMETRY

Reproduced in part with permission from “S.N. Fricke, J. Pourtabib, J. Madsen, S. Chizari, J. Phan, N.K. Tran, M.P. Augustine, Estimates of blood plasma water content using portable NMR relaxometry, *Meas. Sci. Technol.*, **31** (2020) 035701 (9pp).”

Abstract

Although blood plasma water content (PWC) is a relevant metric for many medical diagnostic procedures, the routine clinical measurement of PWC has remained elusive. Portable nuclear magnetic resonance (NMR) offers one way to nondestructively and quickly measure PWC. Contrived pseudoplasma samples that mimic blood plasma while also allowing rigorous control over water content are used to demonstrate the role of NMR in this work. Calibration curves relating measured NMR relaxation time constants (T_2 and T_1) to gravimetric PWC values for a set of human lyophilized plasma samples are used to predict the PWC in porcine and model human blood plasma from respective NMR T_2 and T_1 values. It is shown that the T_2 and T_1 decay constants measured with low field NMR relaxometry correlate with the PWC values for pseudoplasma and human lyophilized plasma samples. Statistical testing of the NMR-PWC correlation model demonstrated a prediction accuracy exceeding 98%. The PWC obtained in this way was used to correct sodium cation concentrations reported from direct ion-selective electrode tests. The accuracy of PWC determination with NMR is comparable to that of the gravimetric method that requires sample lyophilization. The rapid turnaround time, non-destructive nature, and portable footprint of the NMR-PWC measurement makes rapid, point-of-care clinical electrolyte estimates possible.

5.1 Introduction

Sixty percent of the human body is water. Water serves as an important constituent for many biochemical pathways and homeostatic processes. Interestingly, the human plasma water content (PWC) also influences many fundamental medical tests like those used for measuring electrolyte and metabolite concentrations [1–5]. Despite the importance of water, the routine clinical measurement of the amount of this simple molecule in various organs, muscles and bodily fluids has remained elusive. Although gravimetric methods involving sample lyophilization have been used to determine PWC, they are not practical in a high throughput clinical laboratory where speed is critical for patient care [6]. Estimates of PWC have been accomplished by accounting for all of the non-water protein and lipid sample components and by comparing electrolyte concentrations obtained with direct and indirect ion selective electrodes (ISEs). These approaches are less accurate than the gravimetric approach and also consume the patient sample. Due to these limitations, medical practitioners are forced to make generalized assumptions for PWC, if at all, which can result in substantial risk to patient care.

The development and clinical implementation of both ISE and substrate specific electrodes (SSEs) for respective electrolyte and metabolite measurements revolutionized clinical chemistry in the 1980s. Early ISEs were “indirect ISEs” (I-ISEs) that required pre-analytical dilution to achieve sufficient volume to cover the sensor electrodes. Unfortunately, I-ISE specimen dilution assumed a normal PWC of 93%. It was quickly recognized that this PWC assumption was false since samples containing excess protein and/or lipids create a water exclusion effect that significantly alters the PWC [1,5,7]. Since the I-ISE dilution volume is unchanged, the exclusion effect introduces an additional dilution factor that falsely lowers measured electrolyte concentrations. Today, I-ISEs continue to be used in mainframe laboratory analyzers due to their longevity and cost-effectiveness, while direct ISEs (D-ISEs) not requiring pre-analytical dilution have been developed for point-of-care applications.

In contrast to ISEs, SSEs measure the molality of metabolites such as glucose and creatinine. As before, it was assumed that PWC remained unchanged. Fogh-Andersen et al. in the early 1990’s proposed

a whole blood-to-plasma glucose conversion factor of 1.11 based on the 93% PWC assumption [3,4]. This conversion factor was adopted by the International Federation for Clinical Chemistry (IFCC) in 2008 [8]. However, subsequent studies showed that whole blood glucose and creatinine measurements change during critical illness where PWC may also significantly change [2,9]. To this end, a rapid and accurate method for measuring PWC is currently an unmet need in human medicine.

Portable nuclear magnetic resonance (NMR) offers a way to quickly measure PWC without altering the specimen. In brief, portable NMR is a powerful analytical technique that can non-invasively probe samples with unorthodox geometries and differentiate between components of chemical mixtures [10]. When placed in a static external magnetic field, B_0 , a sample like water will magnetize. The size of magnetization is related to the nuclear spins in the proton nuclei, ^1H , residing in the hydrogen atoms. This magnetization is typically measured by applying a pulsed radio frequency (rf) magnetic field, B_1 , directed perpendicular to B_0 at the Larmor frequency, a value that depends on the size of B_0 and the structure of the ^1H nucleus [11,12]. In the experiments reported here, $B_0 = 0.367$ T and the Larmor frequency used for the rf pulses is 15.63 MHz. The time constant for a sample to magnetize when placed in a magnet is called T_1 , while the time constant for the signal to decay to zero, or equivalently, the time constant for magnetization created perpendicular to B_0 with an rf pulse to decay to zero is T_2 . Recent technological advancements have made portable NMR economically and practically feasible. The ease with which it can be customized to address specific, scientific and clinical problems makes portable NMR an extremely attractive technique.

NMR relaxometry has already been successfully applied to the study of blood plasma [13]. It is well known that the dominant proton NMR signal in blood plasma is attributed to water, because water generally accounts for >80% of blood and >90% of blood plasma or serum by mass, as shown in Fig. 2B of ref. 13. Spin relaxation occurs predominantly through dipolar coupling brought about by locally fluctuating magnetic fields [11,12]. The chief effector of these field fluctuations is the Brownian movement of molecules [14]. In addition to water, a myriad of proteins, lipoproteins, and metabolites are also present in blood, and these molecules interact with water molecules via the formation of hydrogen bonds. In turn,

these interactions affect the spin relaxation properties of water by altering the rotational correlation time of the bound-state water, which is inversely proportional to T_2 and T_1 , and is defined as the time required for a molecule or molecular complex to rotate by one radian. Since the correlation time increases with an increase in molecular size (i.e., in the addition of blood components to pure water), as well as with an increase in viscosity or decrease in temperature as described by the generalized Stokes-Einstein-Debye equation [14,15], it is expected that plasma samples with lower water content will have faster relaxation times.

Moreover, rapid proton exchange occurs between free water, protein-bound water, and other hydrogen atoms on proteins [16]. Since the exchange time for these protons is short in comparison to T_2 and T_1 , with respective timescales of 10^{-9} s for exchange versus $10^{-3} - 10^0$ s for spin relaxation, this phenomenon results in a weighted averaging of T_2 and T_1 values for bound and unbound water.

Over 90% of the total protein concentration in blood can be attributed to the following most abundant proteins, which are albumin, immunoglobins, transferrin, fibrinogen, α_2 -macroglobulin, α_1 -antitrypsin, C3 complement, and haptoglobin. Moreover, >80% of this total concentration corresponds to the first two respective proteins [17]. This means that, in effect, only a few different proteins have a significant influence on the nuclear spin relaxation of plasma water. It is therefore not surprising that the relaxation rate of plasma water correlates linearly with the net concentration of proteins in the blood [18-21].

The approach pioneered by Cistola and Robinson [13] is to use the relaxation properties of water to monitor the type and relative quantities of blood proteins and lipoproteins. This provides information relating to global biomarkers that can be used as early indicators of disease. The premise of this study is to take a complementary approach that uses the proton NMR signal to characterize the percentage of water, rather than the blood components, present in a plasma sample.

The preliminary goal of this study is to demonstrate the analytical performance of low field NMR relaxometry in PWC measurements. The approach takes advantage of a correlation between PWC and measured T_2 and T_1 values. By constructing models from the correlation of PWC to T_2 and T_1 values obtained from measurements on standard samples, the T_2 and T_1 values from similar substances like porcine and model human blood plasma are used to predict an appropriate PWC value. After describing the NMR experiments used to obtain the T_2 and T_1 values below, the accuracy of the approach is tested using contrived pseudoplasma matrices. The real value of the NMR-based PWC estimate is then framed by an application of the approach to porcine and model human blood plasma samples. In the latter model human blood plasma sample set, the NMR PWC measurement is used to correct clinical I-ISE sodium cation (Na^+) concentration estimates.

Table 5.1. Summary of best fit parameters for the shifted log function $PWC = A \log(T_n) + B$ for $n = 1, 2$

sample	T ₂		T ₁	
	A ^a	B ^a	A ^a	B ^a
pseudoplasma	11.61	12.66	38.02	-221.50
human lyophilized plasma	8.00	40.29	32.66	-175.78

^aAll error is within 1.8%.

5.2 Methods

5.2.1 Plasma Standards

Two separate liquids were used for standard materials and all chemicals were purchased from Sigma Aldrich, Lee Biosolutions, or similar vendors. The first standard referred to here as “pseudoplasma” was prepared by mixing bovine serum albumin, intralipid, sodium chloride, and urea with water to produce PWC percentages ranging from 70 – 98%, in increments of 2%. Normal saline water was used, since it is relatively (albeit not completely) isotonic to normal plasma. No special precautions were taken to de-oxygenate the water, in order to mimic the properties of clinical blood plasma samples and the fact that normal saline is dosed in the same manner in live patients. The partial pressure of oxygen (pO_2) in these samples would be comparable to what is present in atmospheric pressure (~160 mmHg). The pO_2 was constant throughout all of the samples.

In an effort to better simulate real world samples, the second standard, referred to here as “human lyophilized plasma,” or “model human blood plasma,” was purchased from a commercial vendor and diluted in the same way as the first standard. The correlation of NMR and gravimetric data for the human lyophilized plasma sample set was used to estimate the PWC in a test sample set of commercially available porcine blood plasma purchased from the UC Davis Meat Lab. The sample sets considered in this study are blood plasma or designed to simulate blood plasma. It is important to note that complications arising from the presence of paramagnetic deoxy-hemoglobin in whole blood that dramatically shorten the spin relaxation times [22] are avoided here, as the actual samples of interest are blood plasma, not whole blood.

5.2.2 Standard PWC and Na^+ Concentration Measurements

At present, there is no method to measure PWC in patient care. This is the chief motivation for this work. The time-intensive, laboratory based analytical technique currently used to measure the water content of blood plasma is gravimetric [6]. Specifically, the mass of a plasma sample is recorded before and after

a 24-hour lyophilization procedure. The mass difference is assumed to be water and can be converted into a percentage of the initial sample mass.

All Na⁺ concentrations reported here were estimated from clinical lab I-ISEs. These values were corrected by multiplication with a ratio of 93% to the PWC determined from the human lyophilized plasma NMR model shown in Table 5.1.

5.2.3 NMR Testing

All ¹H NMR experiments at a 15.63 MHz Larmor frequency were performed at B₀ = 0.367 T using a Model 4S SpinCore opposing pole face magnet. Free precession signals were obtained from a Tecmag Apollo LF1 spectrometer and ENI 250 kHz – 110 MHz rf amplifier connected to a tuned solenoid coil wrapped around a 1.8 mL tube that holds the plasma sample in the center of the magnet. Operation in this way typically yields an 8.5 μs, π/2 rf pulse with 56 W of applied rf power. The Carr–Purcell–Meiboom–Gill (CPMG) [23], spin-spin T₂ time constant value and the saturation recovery, spin-lattice T₁ time constant value were measured in triplicate at a controlled temperature of 23 °C for each sample.

For CPMG experiments used to measure T₂, the delay between π rf pulses was 3 ms, 1600 spin echoes were obtained, and the repetition time for signal averaging was 13 s. To cancel artifacts arising from pulse imperfections, the initial π/2 rf pulse and the receiver were cycled between +x and -x phase while holding the π rf pulse phase constant at +y. In all cases, signal averaging summed 12 CPMG transient signals. The effect of diffusion on T₂ measurements was inconsequential given the 3 ms π pulse spacing and the <0.5 G/cm field gradient presented by the permanent magnet. For further details on pulse sequences and phase-sensitive detection, the reader may consult refs. [11,12,24,25].

For T₁ measurement, a saturation recovery experiment was preferred because it is faster than an inversion recovery pulse sequence [11,12]. A comparison between the two pulse sequences yielded T₁ values within a few ms of each other for the entire range of pseudoplasma samples considered. As such, it

was determined that the reduced sampling window of the saturation recovery experiment did not appreciably sacrifice measurement precision. The number of free induction decays recorded for the saturation recovery experiments was 80, the repetition time was 13 s, and no signal averaging was required.

The signal-to-noise (S/N) of the raw NMR data was improved with a digital signal filter written in Matlab (Mathworks, Natick, MA).

5.3 Results

5.3.1 T_2 and T_1 Analysis

In order to determine if NMR T_2 and T_1 values correlate with PWC, a 15-sample set of pseudoplasma was prepared with $70\% < \text{PWC} < 98\%$. Both NMR T_2 and T_1 values, in addition to gravimetric estimates of PWC, were obtained for each of these samples and are reported in Supplemental Table 5.1. Figure 1(a) shows the raw CPMG transient signal obtained from the $\text{PWC} = 84\%$ pseudoplasma sample. The individual spin echoes that cause the shaded area beneath the exponential envelope disappear upon post data acquisition signal processing to yield the transient in Fig. 5.1(b). A similar improvement in S/N is obtained for the saturation recovery transient signal for the same sample as shown in Fig. 5.2.

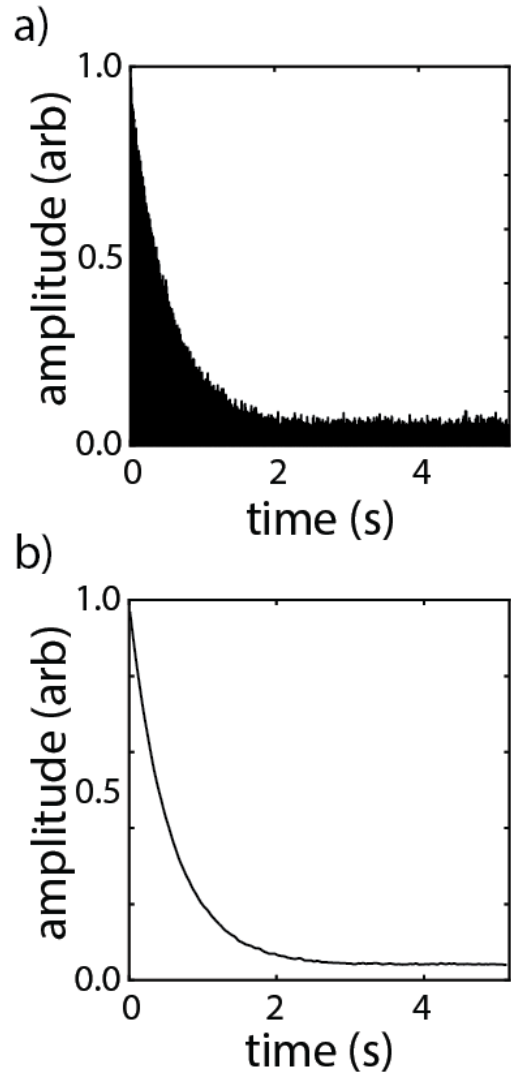


Figure 5.1. (a) An example of the raw, transient relaxation data generated by applying the CPMG pulse sequence to the PWC = 84% pseudoplasma sample. The shaded area corresponds to the 1,600 slightly overlapping spin echoes observed during the 68 s long experiment. Application of a Fourier transform based filter to this data yields the transient in (b).

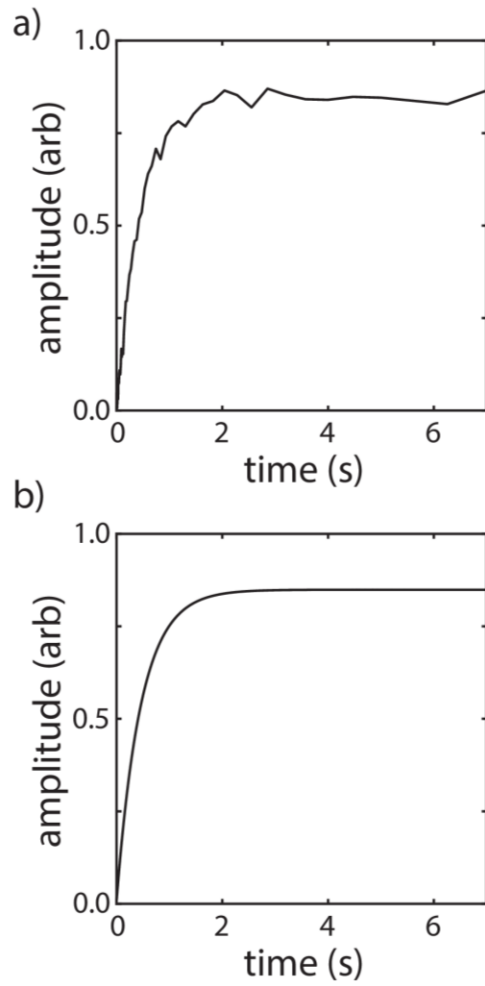


Figure 5.2. (a) An example of the raw, transient relaxation data generated by applying the saturation recovery pulse sequence to the PWC = 84% pseudoplasma sample. Application of a Fourier transform based filter to this data yields the transient in (b).

Analysis of transient signals like those in Figs. 5.1 and 5.2 for all of the pseudoplasma and human lyophilized plasma standards led to the T_2 and T_1 time constant values shown in the second and third columns in Supplemental Tables 1 and 2 respectively. The PWC values obtained from gravimetric analysis of these same samples are shown in the fourth column of these tables.

While the transient relaxation signals obtained in this study could be analyzed with the inverse Laplace transform (ILT) or other multiexponential decomposition signal processing algorithms to reveal multiple T_2 and T_1 components, a stronger correlation was mapped more easily to PWC using the more simplistic single component exponential fitting with non-linear least squares regression. Previous studies reported in depth analyses of the factors that change the distribution of T_2 in blood [13]. However, it is more convenient from a clinical standpoint to pursue the single exponential approach for three reasons. First, a regression-type analysis is more stable than the ILT and less computationally expensive because it is non-iterative. Second, and unlike the ILT, single exponential fitting is readily automated to yield fast and consistent results, which makes it easier to use in a large-scale hospital setting. Finally, a single T_2 or T_1 value from a blood plasma sample can be directly mapped to a standard curve with no ambiguity, which makes the approach attractive from a practical standpoint.

Although one would expect two-to-three exponential decay components for blood plasma, that relate in a physical sense to water, lipid, and protein components, with the largest of these being water, it was found that even in the lowest PWC case analyzed (70%), a mono-exponential fit provided an R^2 value of 0.9998 in the worst case. When compared to a three component multi-exponential fit, the R^2 value for the same sample was 0.9998. Therefore, without sacrificing the goodness of fit of the CPMG data, least squares fitting can rapidly extract a single decay constant. This constant is essentially a weighted average of the multiple T_2 values described in detail by Cistola and Robinson [13], that is simply obtained without any of the computational instability introduced by fixed component ILT. A modeling routine can be automated much more readily by fitting to a mono-exponential, as the correlation map is much simpler between a single decay constant and PWC. In practice, this simplicity makes the model less prone to error.

Since the goal of the NMR experiment in this work is to obtain estimates of T_2 and T_1 values, or the time constants of the transient relaxation signals, any data processing that sacrifices some amplitude but offers significant reduction in noise is attractive. All raw time-dependent transient relaxation signals were Fourier transformed and multiplied by a Gaussian peak in the frequency domain. The improved transient signal is then obtained from an inverse Fourier transform. Operation in this way significantly improves the S/N in both the CPMG and saturation recovery experiments as shown in Figs. 5.1 and 5.2, respectively. The bandwidth of the Gaussian apodization function used to multiply the data in the frequency domain was 100 Hz, a value large enough not to skew the measured T_2 and T_1 values.

5.3.2 T_2 and T_1 Correlation to PWC

Plots of the gravimetric PWC as a function of T_2 and T_1 value are provided in Figs. 5.3 and 5.4 respectively. The solid squares and diamonds in these plots pertain to the respective pseudoplasma and human lyophilized plasma samples. In both Figs. 5.3 and 5.4, the solid and dashed lines correspond to fits of the measured respective pseudoplasma and human lyophilized plasma data to the log-linear model function $PWC = A \log(T_n) + B$ for $n = 1, 2$. A summary of the A and B values for the two separate time constants and the two separate samples is shown in Table 5.1. It is clear from these two plots that both the NMR T_2 and T_1 values correlate well with gravimetric PWC for the pseudoplasma sample set. In all fits, the R^2 value was greater than 0.97.

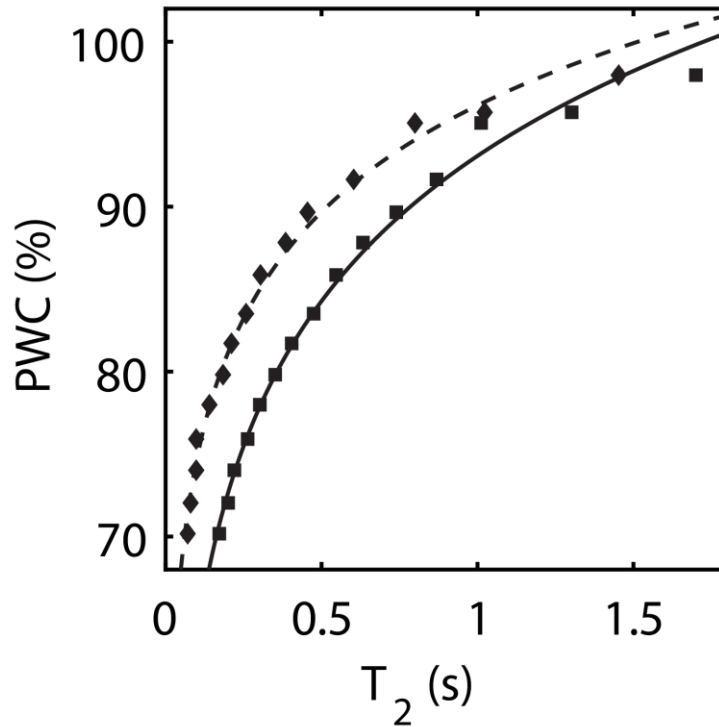


Figure 5.3. Plot showing the correlation of gravimetric PWC with NMR determined T_2 value for the pseudoplasma and human lyophilized plasma sample sets as solid squares and diamonds respectively. The solid and dashed lines for the respective pseudoplasma and human lyophilized plasma samples were calculated from the appropriate A and B values in Table 5.1. The error bars largely obscured by the data markers indicate 95% confidence.

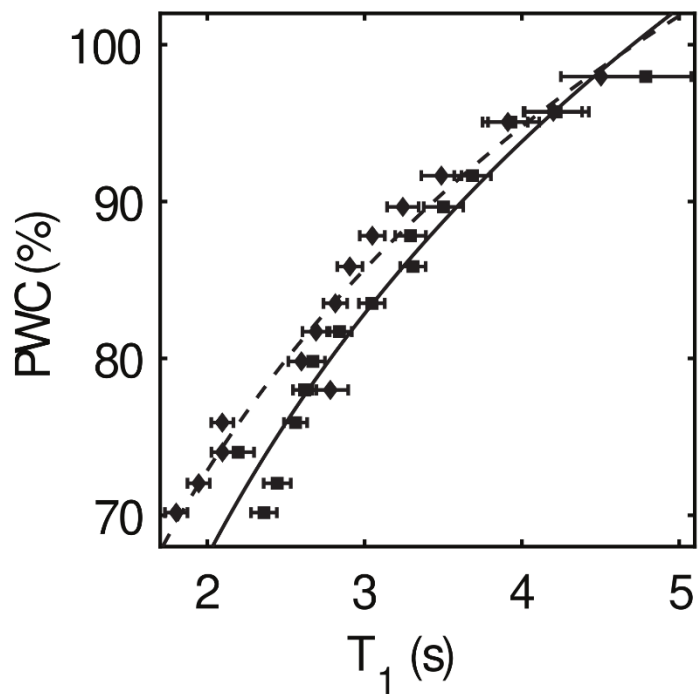


Figure 5.4. Plot showing the correlation of gravimetric PWC with NMR determined T_1 value for the pseudoplasma and human lyophilized plasma sample sets as solid squares and diamonds respectively. The solid and dashed lines for the respective pseudoplasma and human lyophilized plasma samples were calculated from the appropriate A and B values in Table 5.1. The error bars indicate 95% confidence.

To create models between non-linearly related variables, a log-linear function is typically the first choice, due to its flexibility and generalizability [26,27]. Log-linear models are one of the most prevalent types of statistical models, and they are known by many names, such as Gibbs distributions, undirected graphical models, Markov random fields or conditional random fields, exponential models, and (regularized) maximum entropy models. Logistic regression and Boltzmann machines are special types of log-linear models. Occam's razor, or the principle of parsimony, dictates that the least complex model with the smallest number of parameters to adequately map a relationship between variables is the best choice for a predictive model. This is because overfitting can lead to a loss of generality [28]. Despite creating a very good description of training data, overfit models may not generalize well to unknown "test" data, and therefore have poor predictive power.

The solid lines in Figs. 5.3 and 5.4 represent the shifted log function calculated from the appropriate parameters in Table 5.1. The parameterized log function allows a PWC to be calculated from the NMR relaxation time constant value. Such NMR estimates of PWC from T_2 and T_1 are also provided in Supplemental Table 5.1. The ability of NMR to estimate PWC in this way can be tested by exploring the percent difference between the NMR and gravimetric PWC measurements reported in Supplemental Table 5.1. This accuracy is also shown in Supplemental Table 5.1. Averages of these T_2 and T_1 respective accuracies of 98.8% and 98.2% suggest that T_2 measurements are slightly better at reproducing gravimetric PWC estimates in the pseudoplasma sample set.

The ability of the NMR T_2 and T_1 values to report the PWC with greater than 98% accuracy simply means that a correlation between T_2 , T_1 and PWC has been exploited, S/N was adequately improved, and a reasonable function that relates T_2 or T_1 values to PWC in an experimentally relevant range was identified. To make this approach useful, a set of human lyophilized plasma samples in the same $70\% < \text{PWC} < 98\%$ range was prepared to serve as a real sample standard. Construction of the gravimetric PWC value versus NMR T_2 and T_1 curves for these samples was then used to determine PWC in porcine and model human blood plasma samples from respective NMR relaxation time values.

The solid diamonds in Figs. 5.3 and 5.4 relate gravimetric PWC to the respective T_2 and T_1 values for the human lyophilized plasma sample set. Like Supplemental Table 5.1, Supplemental Table 5.2 for the human lyophilized plasma sample set reports these NMR T_2 and T_1 and gravimetric PWC values. The dashed lines in Figs. 5.3 and 5.4 correspond to a shifted log function calculated from the appropriate parameters in Table 5.1. These parameterized log functions are used to estimate PWC from the NMR T_2 and T_1 values, and the results of this calculation are also shown in Supplemental Table 5.2. Again, as was accomplished for the pseudoplasma sample set above, the accuracy of the NMR PWC estimate was calculated by comparison to the gravimetric PWC value. A summary of these accuracies for each of the human lyophilized plasma samples is shown in Supplemental Table 5.2. Averages of these T_2 and T_1 PWC estimate accuracies of 98.2% and 98.5% suggest that the NMR relaxation time constants faithfully reproduce gravimetric PWC values. Consideration of the T_2 and T_1 data simultaneously using a multidimensional regression does not improve the accuracy. The average accuracy in this mixed situation is midway between the accuracies for the separate one-dimensional cases. To evaluate the repeatability of the NMR testing, each sample was analyzed in triplicate. The standard error between trials is plotted in Figs. 5.3 and 5.4, and was much greater for T_1 measurements than for T_2 . In fact, the error in T_2 measurements is smaller than the data markers and is therefore not graphically visible in Fig. 5.3. This was one factor that suggested that the predictive model be based on T_2 , rather than T_1 , NMR measurements.

Table 5.2. Summary of NMR and gravimetric data obtained from the porcine blood plasma sample set

sample	T ₂ (ms) ^a	PWC (%)		prediction accuracy (%) ^d
		NMR ^b	grav. ^c	
1	554	90.8	91.6	99.2
2	451	89.2	91.3	97.7
3	434	88.9	90.6	98.1
4	406	88.3	90.1	98.0
5	372	87.6	89.2	98.2
6	399	88.2	88.9	99.3
7	303	86.0	86.8	99.1
8	259	84.8	85.1	99.6
9	248	84.4	85.0	99.3

^aAll error is within 2.8%.

^bAll error is within 0.006%.

^cAll error is within 0.002%.

^dAccuracy = $(1 - |NMR - grav. / grav. |) \times 100$. All error is within 1.7%.

It can be noted in Figs. 5.3 and 5.4 that the T_2 and T_1 values for human lyophilized plasma samples are slightly shorter than those for the pseudoplasma samples at the same PWC. It is possible that the separation of red blood cells from the plasma was not perfect. These residual red blood cells could lyse to release hemoglobin or paramagnetic deoxy-hemoglobin, which would shorten the spin relaxation times in a consistent way across all samples. Another possibility is that the subjects who provided the samples had some trace amounts of free hemoglobin, which was not measurable by spectrophotometry (or by eye), but was enough to impact the T_2 and T_1 values. Blood collection itself could also cause some hemolysis.

5.3.3 PWC Model Testing

In order to determine whether portable NMR relaxometry can estimate the PWC in real blood plasma samples, the shifted log function with the parameters reported in Table 1 for the human lyophilized plasma data relating T_2 value to gravimetric PWC in Fig. 5.3 and Supplemental Table 5.2 was used. Since the T_2 and T_1 measurements report a PWC value equally well, and because T_2 measurements demonstrated higher repeatability, only T_2 data was obtained for the porcine and model human blood plasma samples. Moreover, the CPMG experiment for estimating T_2 is significantly less time consuming than the saturation recovery pulse sequence used to determine T_1 . It should be clear that, since NMR relaxation times can be magnetic field–and temperature–dependent, corresponding fit parameters from a model cannot be employed on NMR systems operating at different static field strengths and temperatures. The model parameters reported here only apply for this specific magnet at the reported 23 °C temperature. To accomplish this work with other magnets or at other temperatures, calibrations like those reported here must be completed.

Table 5.2 reports the NMR T_2 value for a porcine blood plasma sample set and the PWC value determined from that T_2 value and the human lyophilized plasma parameterized, shifted log function. A gravimetric analysis of these same samples produced the PWC values shown in the fourth column in Table

5.2. Table 5.2 also reports the accuracy of the NMR–determined PWC for each sample in reference to the gravimetric PWC value in that same sample. This accuracy is a true representation of the performance of the NMR based PWC estimation method. The accuracies reported in Supplemental Tables 5.1 and 5.2 communicate self-consistency within each individual model. Here the NMR PWC estimate in porcine blood plasma is based on a gravimetric PWC measurement in human lyophilized plasma via the parameterized, shifted log function determined from human lyophilized plasma. It is this PWC estimate, based on a gravimetric PWC value from human lyophilized plasma, that is compared to the gravimetric PWC measurement for porcine blood plasma in Table 5.2. The 98.7% average prediction accuracy over all samples shown in Table 5.2 is surprisingly as good as the self-consistency checks for all of the relaxation models considered in Supplemental Tables 5.1 and 5.2.

5.3.4 Electrolyte Test Correction

The real value in rapid, non-destructive PWC estimates is in improving clinical measurements. One such measurement is the clinical monitoring of electrolyte concentrations in blood plasma using both D-ISE and I-ISE based devices. It is well known that electrolyte concentrations derived from D-ISE and I-ISE as [D-ISE] and [I-ISE] respectively, differ by a scaling factor as $[D-ISE] = \alpha[I-ISE]$. The reason that the two ISE derived concentrations differ is that the algorithm relating the electrochemical response to the electrolyte concentration in the I-ISE device assumes a 93% PWC. As mentioned above, a constant $\alpha = 1.11$ value was proposed by Fogh-Andersen et al. and was ultimately adopted by the IFCC [3,4,8], although there are many cases during critical illness where $\alpha \neq 1.11$ and thus I-ISE measurements fail to report accurate blood and blood plasma electrolyte concentrations. In these cases, where the actual PWC differs from 93%, better estimates of α are required.

The calculations summarized in Table 3 examine the consequence of correcting the I-ISE measurement by choosing $\alpha = 93\%/PWC$ where PWC is the NMR–determined value. Table 5.3 reports the

NMR T_2 values obtained from a model human blood plasma sample set along with the NMR-determined PWC value calculated from the parameterized, shifted log function for the human lyophilized plasma sample set. The laboratory D-ISE and clinical I-ISE estimates for the Na^+ concentration in these same samples is also reported in Table 5.3, along with two separate I-ISE corrections where α was calculated using both NMR and gravimetric values for PWC. The accuracies of these two separate corrections were also probed by comparison to the D-ISE Na^+ concentration values. The results of this exercise are also shown in Table 5.3. The slightly better 98.1% average accuracy of the NMR based I-ISE Na^+ concentration correction in comparison to the 97.8% average value for the gravimetric measurement is a useful result. This result suggests that once calibrated, a simple, non-destructive, rapid NMR estimate of blood PWC can be used in tandem with clinical I-ISE measurements to faithfully produce equivalent results to the more lengthy and destructive D-ISE tests and sample lyophilization.

Table 5.3. Summary of NMR, gravimetric, D-ISE Na⁺ concentration, and I-ISE Na⁺ concentration results from model human blood plasma samples

sample	NMR		[D-ISE] (mmol/L) ^d	[I-ISE] (mmol/L)			prediction accuracy (%) ^a	
	T ₂ (ms) ^b	PWC(%) ^c		clinic ^e	NMR ^f	grav. ^g	NMR ^h	grav. ^h
1	332	80.1	173.0	151	175.7	175.5	98.5	98.6
2	329	80.0	171.4	150	175.8	174.0	97.5	98.5
3	695	88.6	149.7	141	147.5	145.5	98.5	97.2
4	690	88.6	151.4	142	148.5	146.8	98.1	97.0

^aAccuracy = (1 - |[I-ISE] - [D-ISE]|/[D-ISE])x100

^bAll error is within 1.5%

^cAll error is within 0.004%

^dAll error is within 0.5%

^eAll error is within 1%

^fAll error is within 0.01%

^gAll error is within 0.002%

^hAll error is within 0.9%

5.4 Discussion

Plasma water content affects the accuracy of routine laboratory measurements. Altered PWC *in vivo* is also attributed to disease [29]. Until this study, the routine measurement of PWC in clinical specimens was not feasible. The ability of NMR spectroscopy to quickly and inexpensively detect the water content of blood plasma relies on the experimental observation that the two NMR relaxation time constants T_2 and T_1 appear to correlate with water content or PWC at low magnetic field.

This work provides no information regarding the underlying, molecular-level mechanisms that govern nuclear spin relaxation in serum samples. Sample viscosity, temperature, dissolved salts, proteins, and metabolites all contribute to the observed T_2 and T_1 values. A correlation of T_2 and T_1 values with PWC does not mean that water concentration dictates or directly controls the observed relaxation times. In contrast to assays that detect the concentrations of individual metabolites and biomarkers directly, measurement of plasma T_2 and T_1 values can provide information about the bulk, macroscopic properties of a plasma sample. This type of analysis, in conjunction with parameters obtained from traditional laboratory testing, offers a way to monitor net changes in blood plasma that have the potential to inform clinicians about the overall health of a patient.

The central idea behind the NMR method presented here is simplicity. This measurement is not intended to be the sole technique implemented for clinical analysis of a sample, rather, it is meant to be used together with the host of other laboratory techniques that provide accurate measurements of other blood components. The speed with which this method provides results might be beneficial in time-sensitive cases as well, since PWC is not yet routinely measured, despite the fact that knowledge of PWC would better inform clinicians about a patient's health.

5.5 Conclusion

A significant percentage of medical decisions are based on laboratory tests, many of which are blood chemistry assays [30–35]. However, the accuracy of certain blood tests depends on PWC, which is not typically measured in clinical laboratories. This is because the current gold standard method for measuring PWC is lyophilization, which is a time-intensive process that requires about a day. The delays from this procedure are prohibitive in a clinical laboratory that must process thousands of samples daily, and are unacceptable in situations that require urgent treatment decisions. Consequently, blood test results are based on the assumption of a standard value of $PWC = 93\%$. However, variance in PWC between patients can influence many test results, with blood electrolyte and metabolite measurements being perhaps the most notable. Without knowledge of the patient PWC, clinicians are unable to correct for possible inaccuracies and patients are thus more subject to misdiagnosis and suboptimal care.

It has been estimated that at least \$200 billion are wasted annually on unnecessary testing and treatment in the United States alone [36,37]. Development of a rapid test to measure PWC provides clinicians with a means to improve the accuracy of blood chemistry assays and diagnostic tests, which improves patient care and reduces waste.

This study uses portable NMR relaxometry to estimate PWC. Since NMR is non-destructive to the sample and testing can be accomplished in a matter of minutes, it is an ideal tool for the clinical laboratory. The accuracy of PWC determination with NMR is comparable to the gravimetric method that requires sample lyophilization. The rapid turnaround time and non-destructive nature of the NMR approach is a significant advantage in comparison to lyophilization to determine PWC. Given that it takes about one minute to run a CPMG experiment on a plasma sample, the delay will have a negligible effect on the throughput of a modern clinical laboratory. In fact, this time is comparable to the time required to perform a hemolysis index to evaluate specimen integrity. This test can be implemented immediately to run on all plasma samples intended to measure electrolytes and metabolites such as glucose. The NMR instrument can be configured to run automatically and does not disrupt the workflow in any foreseeable way.

While most tests require a considerable volume of blood, there is an added benefit since NMR only requires a small amount of sample (ca. 1 mL). NMR is also non-destructive, meaning that the same sample can be used for other laboratory tests. Altogether, this is helpful for patients because it reduces the amount of blood that has to be drawn, and yields faster and more accurate blood test results and diagnoses. Future studies are needed to determine the clinical significance of PWC in human health, as well as to study the use of NMR in the non-invasive evaluation of the quality of biological products such as donated blood. It is clear that clotting processes used in hemostasis testing can also be studied. The clinical implementation of portable NMR instruments is currently being explored for immediate application to burn patient hydration treatments at the Regional Burn Center at the UC Davis Medical School.

5.6 Acknowledgements

This project was made possible by funding from NIBIB R25EB012963, the Clinical and Translational Science Center at University of California, Davis, and the Center for Process Analysis and Control at the University of Washington. We thank the UC Davis Health Clinical Chemistry Laboratory for encouragement and support.

Supplemental Table 5.1. Summary of NMR and gravimetric data obtained from the pseudoplasma sample set

sample	NMR time constants (ms)			PWC (%)		prediction accuracy (%) ^a	
	T ₂ ^b	T ₁ ^c	grav. ^d	T ₂ calc. ^d	T ₁ calc. ^d	T ₂ ^e	T ₁ ^f
1	172	2360	70.2	72.4	73.8	96.8	94.8
2	201	2444	72.0	74.2	75.1	97.0	95.8
3	220	2196	74.0	75.3	71.0	98.3	95.9
4	263	2561	75.9	77.3	76.9	98.2	98.7
5	302	2619	78.0	78.9	77.7	98.8	99.6
6	351	2671	79.8	80.7	78.5	98.9	98.4
7	404	2840	81.7	82.3	80.8	99.3	98.9
8	475	3046	83.5	84.2	83.5	99.2	100.0
9	547	3307	85.9	85.8	86.6	99.9	99.1
10	633	3292	87.8	87.5	86.4	99.6	98.4
11	740	3501	89.7	89.3	88.8	99.6	99.0
12	869	3686	91.7	91.2	90.7	99.5	99.0
13	1012	3930	95.1	93.0	93.2	97.8	98.0
14	1302	4218	95.7	95.9	95.9	99.8	99.8
15	1700	4788	98.0	99.0	100.7	99.0	97.2

^aAccuracy = (1 - |NMR - grav. / grav.) x 100

^bAll error is within 1.5%.

^cAll error is within 12%.

^dAll error is within 0.002%.

^eAll error is within .05%.

^fAll error is within 0.1%.

Supplemental Table 5.2. Summary of NMR and gravimetric data obtained from the human lyophilized plasma sample set

sample	NMR time constants (ms)			PWC (%)		prediction accuracy (%) ^a	
	T ₂ ^b	T ₁ ^c	grav. ^d	T ₂ calc. ^e	T ₁ calc. ^f	T ₂ ^g	T ₁ ^h
1	71	1802	70.2	74.3	69.1	94.1	98.5
2	80	1945	72.0	75.3	71.5	95.5	99.3
3	98	2096	74.0	77.0	74.0	96.0	100.0
4	98	2095	75.9	77.0	74.0	98.6	97.5
5	140	2782	78.0	79.8	83.2	97.7	93.3
6	184	2598	79.8	82.0	81.0	97.3	98.5
7	211	2691	81.7	83.1	82.2	98.3	99.4
8	258	2814	83.5	84.7	83.6	98.6	99.9
9	304	2906	85.9	86.0	84.7	99.8	98.7
10	385	3049	87.8	87.9	86.2	99.9	98.2
11	455	3243	89.7	89.3	88.2	99.6	98.4
12	603	3488	91.7	91.5	90.6	99.8	98.9
13	800	3911	95.1	93.8	94.4	98.7	99.3
14	1023	4200	95.7	95.7	96.7	100.0	99.0
15	1453	4503	98.0	98.5	99.0	99.5	99.0

^aAccuracy = (1 - |NMR - grav. / grav.) x 100

^bAll error is within 1.4%.

^cAll error is within 11%.

^dAll error is within 0.002%.

^eAll error is within 0.07%.

^fAll error is within 0.001%.

^gAll error is within 0.04%.

^hAll error is within 0.1%.

References

- [1] Lyon AW, Baskin LB. Pseudohyponatremia in a myeloma patient: direct electrode potentiometry is a method worth its salt. *Lab Med* 2003;34:357–60.
- [2] Straseski JA, Lyon ME, Clarke W, DuBois JA, Phelan LA, Lyon AW. Investigating interferences of a whole-blood point-of-care creatinine analyzer: comparison to plasma enzymatic and definitive creatinine methods in an acute-care setting. *Clin Chem* 2011;57(11):1566-73.
- [3] Fogh-Andersen N, Wimberley PD, Thode J, Siggaard-Andersen O. Direct reading glucose electrodes detect the molality of glucose in plasma and whole blood. *Clin Chim Acta* 1990;189:33-8.
- [4] Fogh-Andersen N, D’Orazio P. Proposal for standardizing direct-reading biosensors for blood glucose. *Clin Chem* 1998;44(3):655-9.
- [5] Nguyen MK, Ornekian V, Butch AW, Kurtz I. A new method for determining plasma water content: application in pseudohyponatremia. *Am J Physiol Renal Physiol* 2007;292:F1652-6.
- [6] Waugh WH. Utility of expressing serum sodium per unit of water in assessing hyponatremia. *Metabolism* 1969;18(8):706-12.
- [7] Lopez J. Carl A. Burtis, Edward R. Ashwood and David E. Bruns (eds): *Tietz Textbook of Clinical Chemistry and Molecular Diagnosis* (5th edition): Elsevier, St. Louis, USA, 2012, 2238 pp, 909 illustrations. ISBN: 978-1-4160-6164-9. *Indian J Clin Biochem* 2013;28(1):104-5.
- [8] D’Orazio P, Burnett RW, Fogh-Andersen N, et al. Approved IFCC recommendation on reporting results for blood glucose (abbreviated). *Clin Chem* 2005;51(9):1573-6.
- [9] Lyon ME, DuBois JA, Fick GH, Lyon AW. Estimates of total analytical error in consumer and hospital glucose meters contributed by hematocrit, maltose, and ascorbate. *J Diabetes Sci Technol* 2010;4(6):1479-94.
- [10] Blumich B, Perlo J, Casanova F. Mobile single-sided NMR. *Prog Nucl Magn Reson Spectrosc* 2008;52(4):197-269.

- [11] Freeman R. A Handbook of Nuclear Magnetic Resonance (second ed.): Longman Group, United Kingdom, 1997.
- [12] Levitt M. Spin Dynamics: Basics of Nuclear Magnetic Resonance: John Wiley & Sons, Ltd, New York, NY, 2001.
- [13] Cistola DP, Robinson MD. Compact NMR relaxometry of human blood and blood components. Trends Anal. Chem 2016;83:53-64.
- [14] Einstein A. Investigations on the Theory of the Brownian Movement: Dover Publications, Mineola, New York, 1956 (re-publication of the original translation from 1926).
- [15] Debye PJW. Polar Molecules: The Chemical Catalog Company, Inc., New York, 1929.
- [16] Hills BP. The proton exchange cross-relaxation model of water relaxation in biopolymer systems. Mol Phys 1992;76:489-508.
- [17] Lundblad R. Considerations for the Use of Blood Plasma and Serum for Proteomic Analysis. Internet J. Genom. Proteom. 2003;1(2).
- [18] Kang YS, Gore JC, Armitage IM. Studies of factors affecting the design of NMR contrast agents: manganese in blood as a model system. Magn Reson Med 1984;1(3):396-409.
- [19] Raeymaekers HH, Borghys D, Eisendrath H. Determinants of water proton T_1 in blood serum. Magn Reson Med 1988;6:212.
- [20] Schuhmacher JH, Conrad D, Manke HG, Clorius JH, Matys ER, Hauser H, Zuna I, Maier-Borst W, Hull WE: Investigations concerning the potential for using ^1H NMR relaxometry or high resolution spectroscopy of plasma as a screening test for malignant lung disease. Magn Reson Med 1990;13:103-132.
- [21] Yilmaz A, Ulak FS, Batun MS. Proton T_1 and T_2 relaxivities of serum proteins. Magn Reson Imaging 2004;22(5):683-8.

- [22] Silvennoinen MJ, Kettunen MI, Clingman CS, Kauppinen RA. Blood NMR relaxation in the rotating frame: mechanistic implications. *Arch. Biochem. Biophys.* 2002;405(1), 78–86. doi:10.1016/s0003-9861(02)00286-2
- [23] Meiboom S, Gill D. Modified spin-echo method for measuring nuclear relaxation times. *Review of Scientific Instruments* 1958;29(8), 688–691. <https://doi.org/10.1063/1.1716296>
- [24] Carr HY, Purcell EM. Effects of diffusion on free precession in nuclear magnetic resonance experiments. *Physical Review* 1954;94(3), 630–638. <https://doi.org/10.1103/PhysRev.94.630>
- [25] Cavanagh J, Fairbrother WJ, III Palmer WG, Rance M, Skelton NJ. *Protein NMR Spectroscopy* (second ed.): Elsevier, 2007.
- [26] Bishop YM, Fienberg SE, Holland PW. *Discrete Multivariate Analysis: Theory and Practice*: Springer, 2007.
- [27] Steyerberg E. *Clinical Prediction Models: A Practical Approach to Development, Validation, and Updating*. Springer, 1st ed., 2009.
- [28] Hawkins D. The problem of overfitting, *J. Chem. Inf. Comput. Sci.*, 2004;44(1), 1–12.
- [29] Ismael S, Savalle M, Trivin C, Gillaizeau F, D’Auzac C, Faisy C. The consequences of sudden fluid shifts on body composition in critically ill patients. *Crit Care* 2014;18(2):R49.
- [30] Hallworth MJ, Epner PL, Ebert C, Fantz CR, Faye SA, Higgins TN, et al. Current evidence and future perspectives on the effective practice of patient-centered laboratory medicine. *Clin Chem* 2015;61(4):589-99.
- [31] Badrick T. Evidence-based laboratory medicine. *Clin Biochem Rev* 2013;34(2):43-6.
- [32] Ngo A, Gandhi P, Miller WG. Frequency that laboratory tests influence medical decisions. *J Appl Lab Med* 2017;1(4):410-4.
- [33] Epner PL, Gans JE, Graber ML. When diagnostic testing leads to harm: a new outcomes-based approach for laboratory medicine. *BMJ Qual Saf* 2013;22(Suppl 2):ii6-10.

- [34] Drozda JP Jr. Physician performance measurement: the importance of understanding physician behavior. *JAMA Intern Med* 2013;173(15):1444-6.
- [35] Zhi M, Ding EL, Theisen-Toupal J, Whelan J, Arnaout R. The landscape of inappropriate laboratory testing: a 15-year meta-analysis. *PLoS One* 2013;8(11):e78962.
- [36] Caloyeras JP, Kanter MH, Ives NR, Kim CY, Kanzaria HK, Berry SH, et al. Understanding waste in health care: perceptions of frontline physicians regarding time use and appropriateness of care they and others provide. *Perm J* 2018;22:17-176.
- [37] Institute of Medicine (US) Roundtable on Evidence-Based Medicine; Yong PL, Saunders RS, Olsen LA, editors. *The healthcare imperative: lowering costs and improving outcomes: workshop series summary*. Washington (DC): National Academies Press; 2010.

6. REAL-TIME SENSOR FOR IN-LINE ANALYSIS OF MATERIAL RHEOLOGY

6.1 Introduction

Any discussion of relaxometry measurements that relate to rheology, or flow, begs the question of: how one can perform measurements on a sample when it is literally leaving as soon as it is magnetized? Essentially, there is now a moving target. The first observation one will notice after starting a flow pump and beginning a CPMG experiment with a magnet placed next to a liquid-containing pipe, is that the T_2 shortens. T_1 measurement is out of the question because it takes too long, and detection of a free induction decay is nearly impossible. Additionally, the phase of the signal changes as a sample moves through the coil because rf induction of magnetization occurs at a different location than the relaxation that induces the detected signal. As the flow velocity increases, the apparent T_2 also shortens. Because T_2 is difficult to detect in a robust way with a standard CPMG, it is necessary to explore alternative pulse sequence strategies for T_2 measurement.

The pseudoecho experiment described by Ferrari et al. [1] is useful for situations where the T_2 is too short to measure traditionally. In essence, a weak lock rf field is implemented before and after π pulses of a standard spin echo experiment to negate the distributive effects of diffusion and to slow down the loss of coherence. This, in turn, introduces a frequency-dependent phase shift that can be noted in a process of even echo rephasing and odd echo dephasing. A final $\pi/2$ readout pulse is optional. This weak lock rf field strategy is also effective between π pulses in an echo train to create a “pseudo-CPMG”. Figure 6.1 depicts a pulse sequence for the pseudoecho experiment.

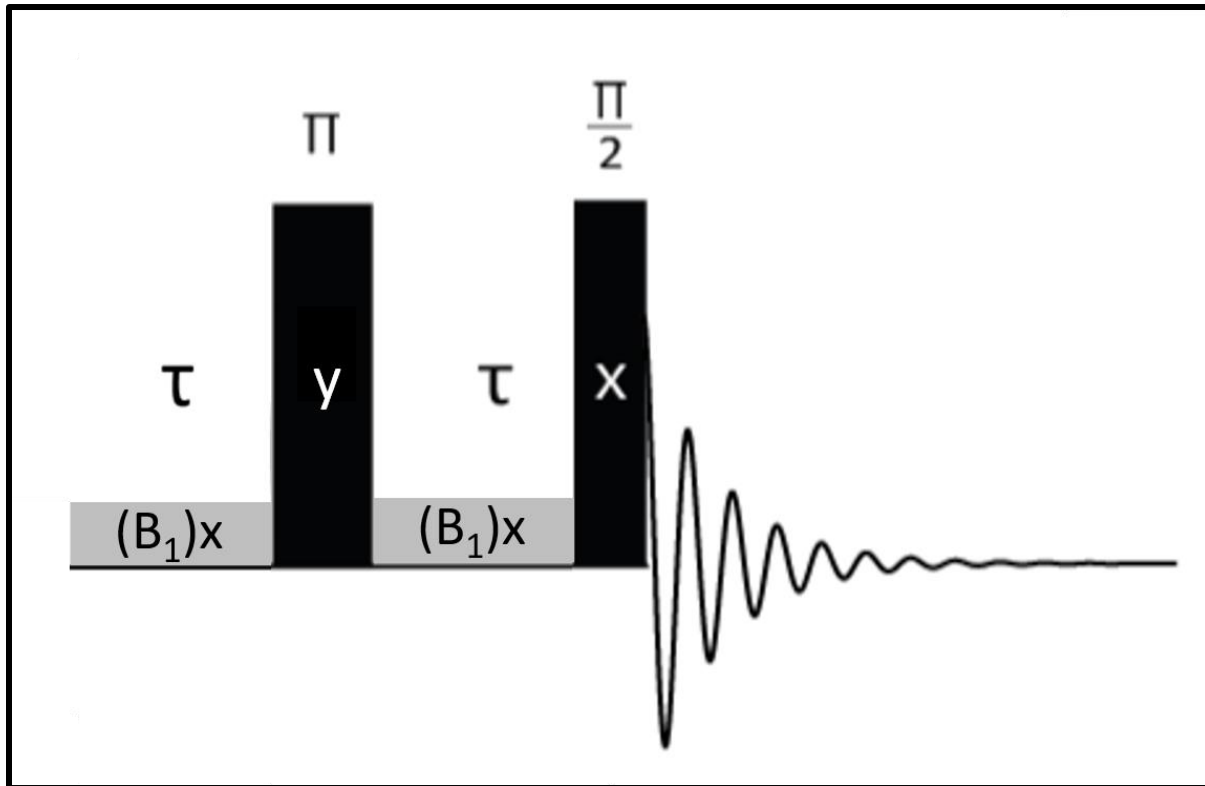


Figure 6.1. Pulse sequence diagram for a pseudoecho experiment, shown with a weak lock rf field, $(B_1)x$, sandwiching the π pulse in a spin echo experiment. The final $\pi/2$ readout pulse is optional – with it, the signal appears like a nutation signal decaying from an initial positive amplitude. Without the readout pulse, the signal exhibits decaying oscillations from an initial amplitude of zero.

The phase shift due to diffusion or flow that is experienced by a moving spin is proportional to its velocity, v , the strength of the applied gradient, G , and the square of the length of time it moves within that gradient, t^2 , as

$$\theta(t) = \frac{1}{2} \gamma G v t^2. \quad (6.1)$$

Additionally, gradients can be controlled by coil designs in the probe. Hence, it would be advantageous to build a coil that could be tuned to take advantage of gradient effects to control the modulation evident in the signal that results from the phase shift.

6.2 Methods and Results

Here, two coils were built to measure flowing samples. The geometry of the first coil is shown diagrammatically in Fig. 6.2 – it is a classic solenoid wrapped around a pipe, which allows a liquid to flow through it.

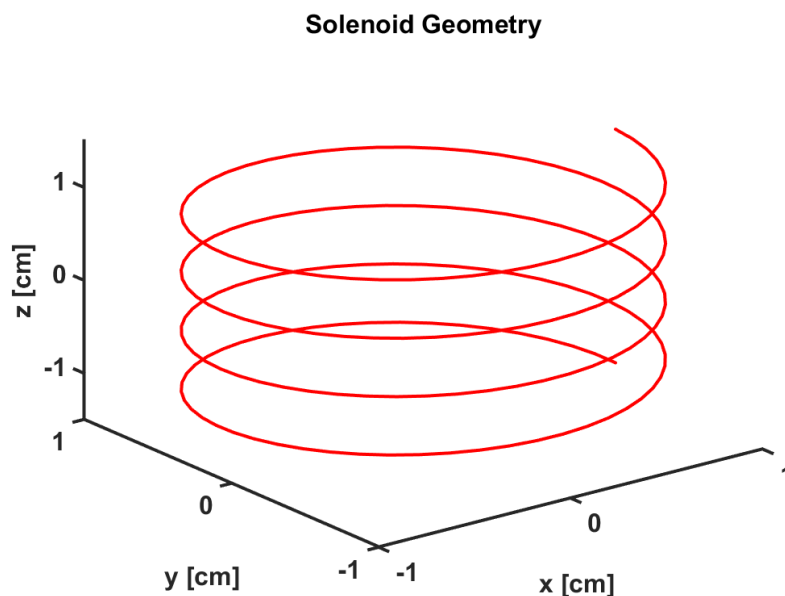


Figure 6.2. Diagram of a classic solenoid coil that was wrapped around a pipe, which allows a liquid to flow through it.

The second coil that was built is called a split solenoid, shown in Fig. 6.3. Simply put, it is a solenoid that reverses direction in the middle to change the direction of the applied rf field. This generates a gradient in induced rf magnetic field (B_1).

Split Solenoid Geometry

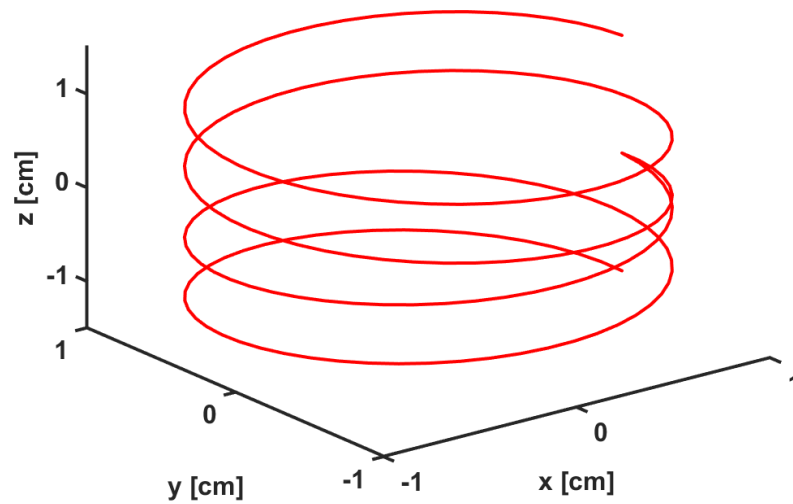


Figure 6.3. Diagram of a split solenoid coil that was wrapped around a pipe, which allows a liquid to flow through it. The solenoid that reverses direction in the middle to change the direction of the applied rf field.

Next, to visualize the magnetic flux lines and B_1 fields generated by each coil, Biot-Savart modeling was performed in Matlab to create B_1 heat maps and flux line plots for the simple and split solenoids. The results are shown in Figs. 6.4 – 6.7. It is particularly helpful to note the field reversal in the upper section of the split solenoid in Figs. 6.5 and 6.7.

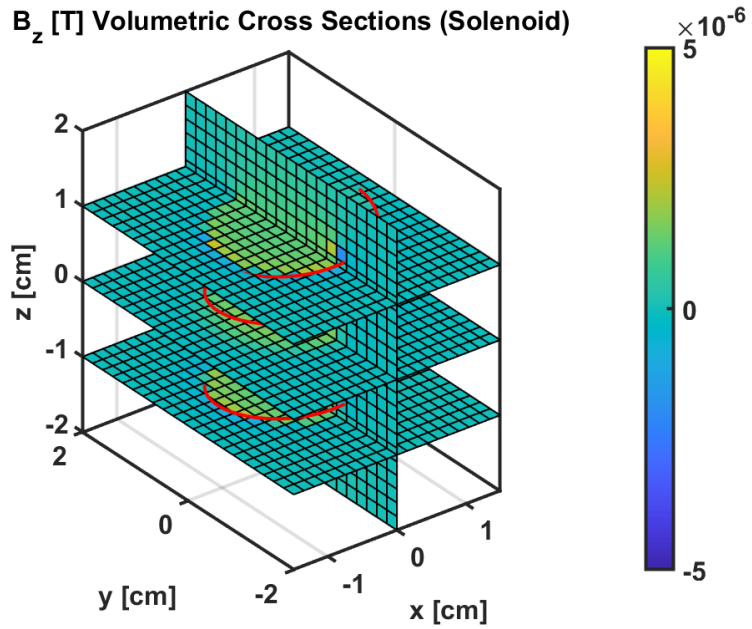


Figure 6.4. Biot-Savart modeling of B_1 fields generated by original solenoid inductor. Modeling B_1 fields generated by coils such as this is useful in probe design.

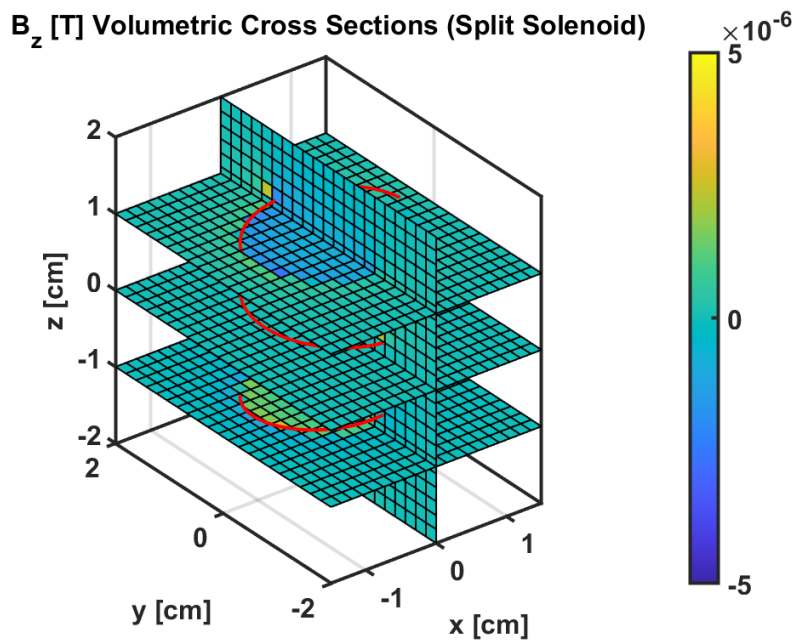


Figure 6.5. Biot-Savart modeling of B_1 fields generated by split solenoid inductor.

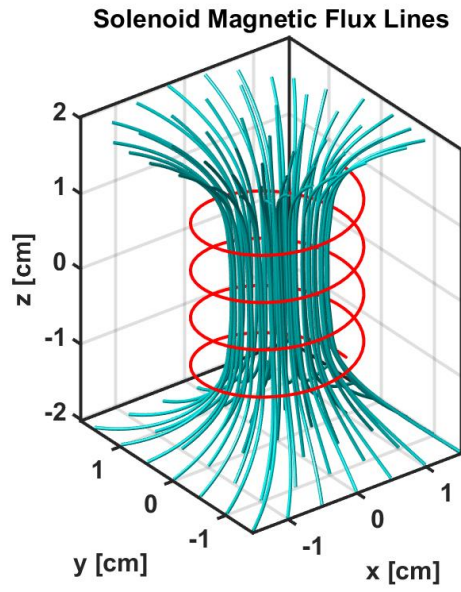


Figure 6.6. Magnetic flux lines created from Biot-Savart modeling of the simple solenoid.

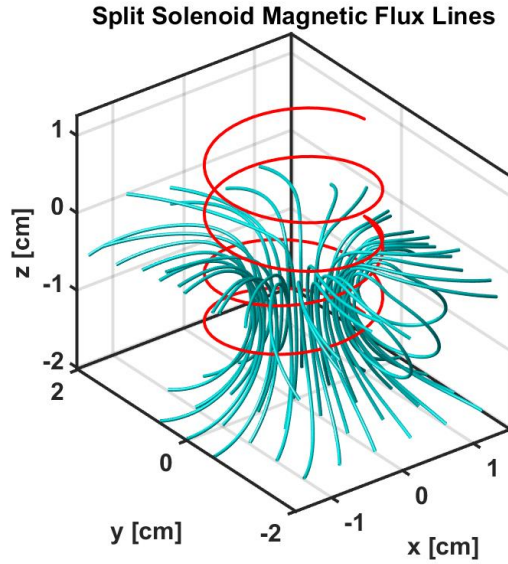


Figure 6.7. Magnetic flux lines created from Biot-Savart modeling of the split solenoid, showing a field reversal at the directional change at the coil midpoint.

The split solenoid, or gradient coil, accentuates the modulation effect of the weak spin-lock field on flowing samples in the pseudoecho experiment. Figure 6.8 demonstrates the heightened signal modulation in the split solenoid compared to the original solenoid with a static sample, using a 4 MHz ^1H frequency single sided magnet [2].

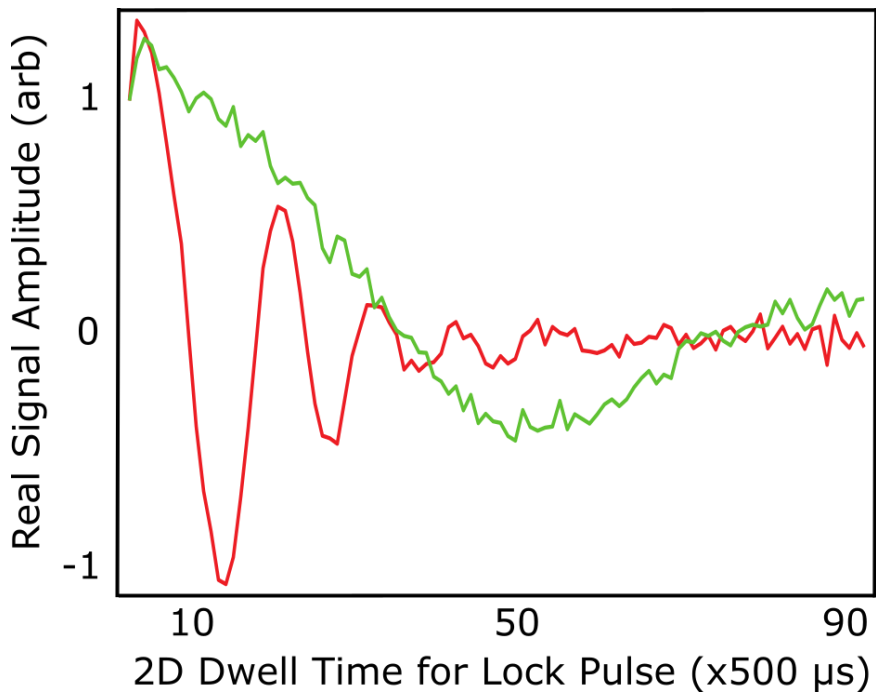


Figure 6.8. Signal from a pseudoecho experiment using the split solenoid (shown in red) and original solenoid (shown in green). Note the enhancement in modulation frequency with the split solenoid. The sample was CoffeeMate coffee creamer.

Additionally, varying the strength of the locking rf field can control the frequency of the signal modulation. This is shown in Fig. 6.9, which illustrates that stronger lock fields cause a higher modulation frequency in the signal.

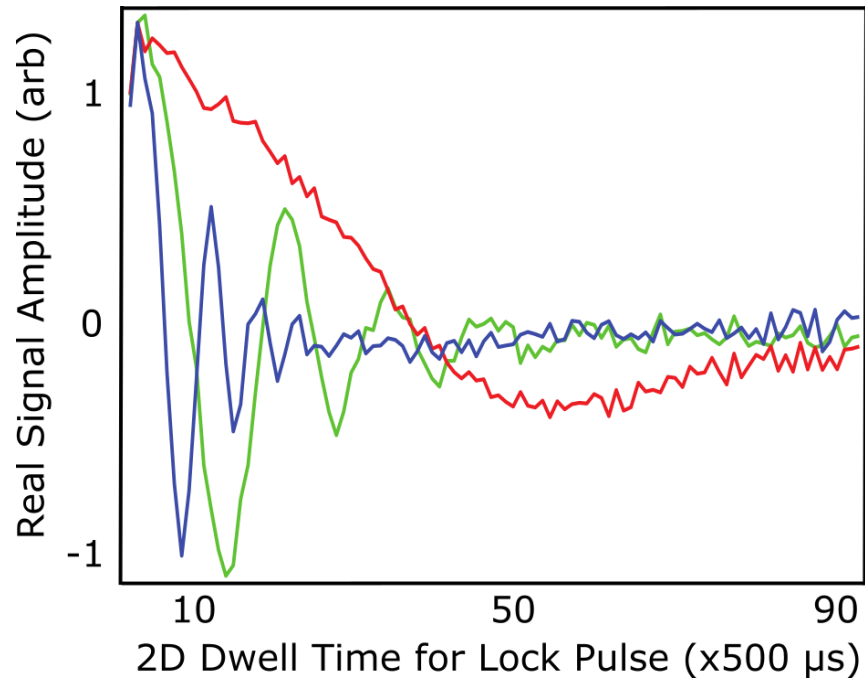


Figure 6.9. Variation in lock rf field strength affects the frequency of the signal modulation from a static sample of coffee creamer. The red signal represents the weakest locking field used, at one quarter the strength of the rf pulse. The green signal was from an intermediate locking field that was one third the strength of the rf pulse. The blue signal was from the strongest locking field that was half the strength of the rf pulse.

The modulation amplitude can be used to correlate to and predict Reynolds number, i.e., the relationship between inertial and viscous forces in a fluid, as shown in Figs. 6.10 – 6.13 for a slightly viscous flowing sample of coffee creamer.

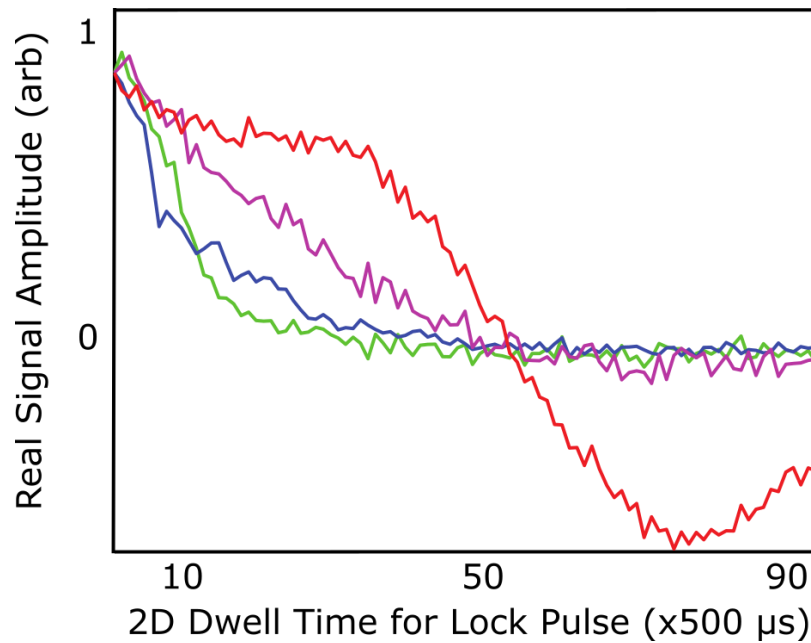


Figure 6.10. Real signal amplitude vs. lock pulse time in units of 500 microseconds for four different flow rates of 0.56 cm/s in green, 0.22 cm/s in blue, 0.11 cm/s in purple, and static 0 cm/s in red with the original solenoid. The modulations occur on too long of a scale to measure accurately.

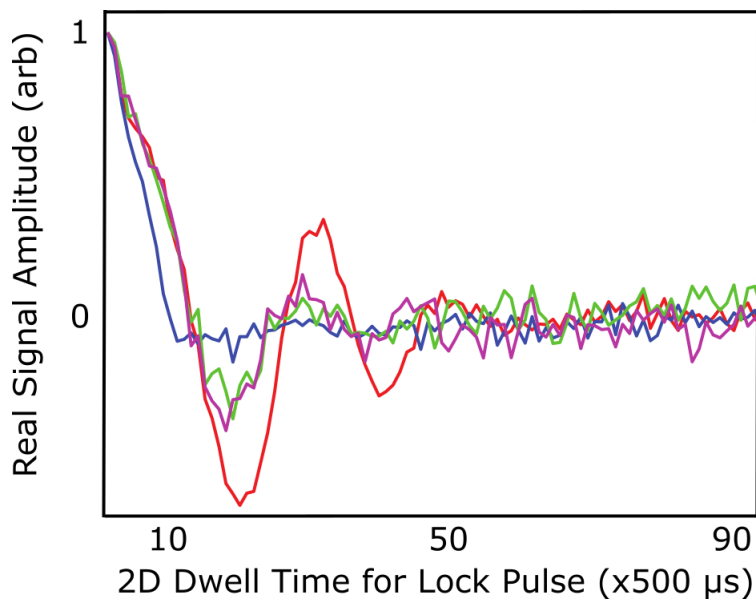


Figure 6.11. Real signal amplitude vs. lock pulse time in units of 500 microseconds for four different flow rates of 0.56 cm/s in blue, 0.13 cm/s in green, 0.075 cm/s in purple, and static 0 cm/s in red with the split solenoid. The modulations occur on a shortened time scale due to the B_1 field gradient.

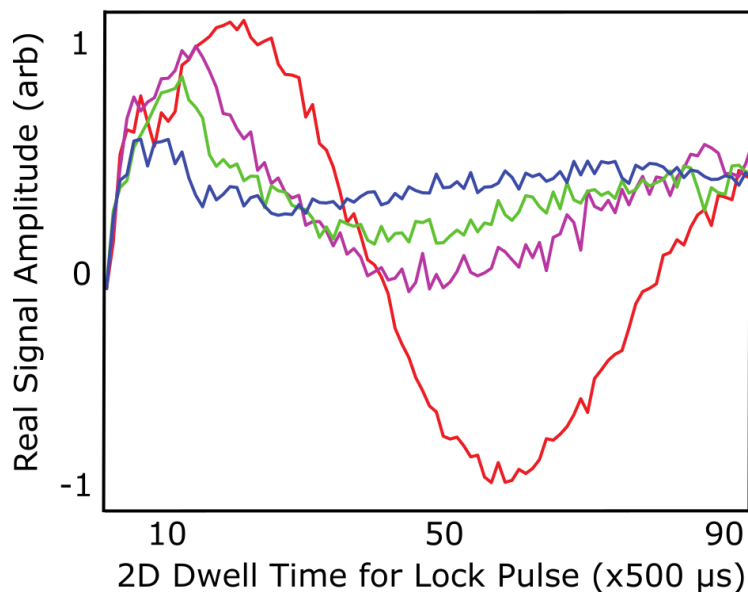


Figure 6.12. Real signal amplitude vs. lock pulse time in units of 500 microseconds for four different flow rates of 0.56 cm/s in blue, 0.13 cm/s in green, 0.075 cm/s in purple, and static 0 cm/s in red with the original solenoid. The modulations occur on a shortened time scale due to the B_1 field gradient. A final π pulse was used before readout to demonstrate a phase shift in the modulations such that they would start at zero.

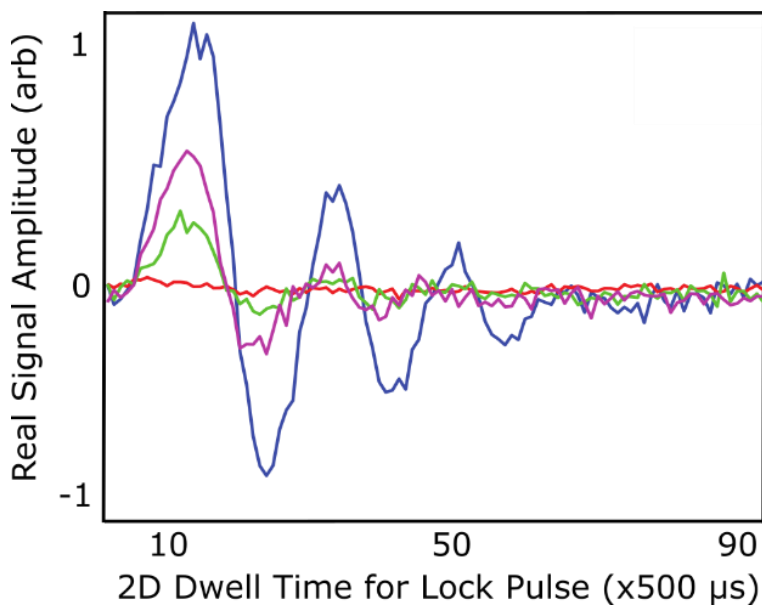


Figure 6.13. Real signal amplitude vs. lock pulse time in units of 500 microseconds for four different flow rates of 0.56 cm/s in red, 0.37 cm/s in green, 0.073 cm/s in purple, and static 0 cm/s in blue with

the split solenoid. The modulations occur on a shortened time scale due to the B_1 field gradient. A final π pulse was used before readout to demonstrate a phase shift in the modulations such that they would start at zero.

The results shown in Figs. 6.10 – 6.13 were measured at four different flow rates with a slightly viscous sample of coffee creamer. The flow setup was a homebuilt mini loop on a laser table that passed through a pump, and pipe segments with coils wrapped around them were incorporated above 4 MHz single sided magnets. The plots in Figs. 6.8 and 6.10 show the pseudoecho signal with the classic solenoid – the modulations are present, but too long to fully capture. The enhanced phase effects from the split solenoid in Figs. 6.9 and 6.11 better capture the modulations, and, interestingly, allow them to be correlated with the flow rate and Reynolds number.

6.3 Discussion and Future Work

The Reynolds number, R_e , is the ratio of inertial forces to viscous forces within a fluid that is subjected to relative internal movement due to different fluid velocities [3,4] as

$$R_e = \frac{\rho u L}{\mu} = \frac{u L}{\nu}. \quad (6.2)$$

In Eq. 6.2, ρ is the density, u is flow speed, L is a linear dimension, μ is the dynamic viscosity, and ν is the kinematic viscosity. Reynolds numbers are an important dimensionless quantity in fluid mechanics. In a practical sense, the Reynolds number helps to predict flow patterns in different fluid flow situations. At low Reynolds numbers, flows are predominantly laminar, or sheet-like, while at high Reynolds numbers, flows are typically more turbulent. The turbulence results from differences in the fluid's speed and direction,

which may sometimes intersect or even move counter to the overall direction of the flow, leading to eddy currents. These eddy currents begin to churn the flow, using up energy in the process, which increases the chances of cavitation for liquids.

Since the Reynolds number is a key metric for many rheological materials, it is worth pursuing the correlation with pseudoecho signal modulation with the gradient coil in greater detail in the future, and exploring a greater range of fluid velocities and viscosities.

References

- [1] Ferrari M, Moyne C, Canet D. Measurement of short transverse relaxation times by pseudo-echo nutation experiments. *J Magn Reson.* 2018;292:8-15.
- [2] A.E. Marble, I.G. Mastikhin, B.G. Colpitts, B.J. Balcom, A compact permanent magnet array with a remote homogeneous field, *J. Magn. Reson.*, 186 (2007) 100-104.
- [3] Stokes G. On the Effect of the Internal Friction of Fluids on the Motion of Pendulums. *Transactions of the Cambridge Philosophical Society.* 1851;9:8–106.
- [4] Reynolds O. An experimental investigation of the circumstances which determine whether the motion of water shall be direct or sinuous, and of the law of resistance in parallel channels". *Philosophical Transactions of the Royal Society.* 1883;174: 935–982.

7. PORTABLE HIGH RESOLUTION NMR FOR AGRICULTURAL AND ENVIRONMENTAL PURPOSES

7.1 Field-based Agricultural Plant Screening for Citrus Greening Disease

Recently, there has been growing interest in using high field NMR as a screening tool for performing metabolomic analysis in agricultural industries. One of the biggest problems in the California citrus industry is a greening disease that not only kills trees and destroys crops, but is also highly contagious [1]. Early detection is an issue, and NMR has emerged as one of the most sensitive chemometric tools for early detection. Previous studies [1] have focused on testing extractions from symptomatic and asymptomatic leaves, and using principal component analysis to create models from the resulting spectra.

The greening disease is transmitted by citrus psyllids, which are insects that feed from the sap of citrus trees, and, in doing so, spread the disease. Here, the presence of these insects was used as confirmation of infection in some lemon trees that were screened at UC Davis.

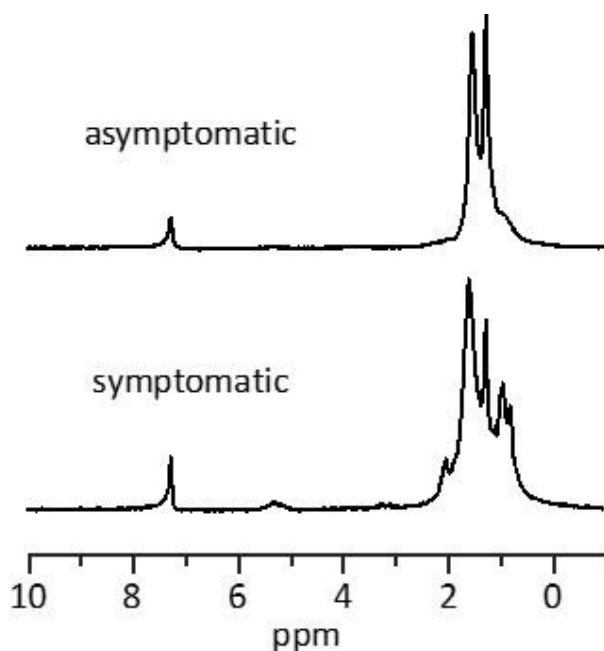


Figure 7.1. Altered NMR profile of symptomatic versus asymptomatic lemon tree leaf extraction in CDCl₃ taken at 60 MHz ¹H frequency.

The goal of this study was to reproduce published spectra [1] from a 300 MHz spectrometer that could differentiate between symptomatic and asymptomatic trees with a cryogen-free, benchtop 60 MHz Aspect Imaging instrument that has been optimized for portable, high-field use. The results in Fig. 7.1 suggest that a difference was detected that could be used for earlier detection and rapid screening of the disease in the future.

7.2 Tracking Wildfire Forest Recovery through Terpene Analysis of Pine Resin

Another example that motivates the goal of making high field NMR portable is to monitor forest recovery after wildfires. Recently, wildfires have been devastating a variety of ecosystems in California with unprecedented magnitude. As this problem has emerged, there is a growing need to scientifically track the impact and recovery of burn scar areas, and this can now be accomplished in the field through terpene profiling of pine resin. Figure 7.2 shows some burned and unburned trees that have been tested in the Sierra, and the altered profile from the NMR spectrum from burned area.

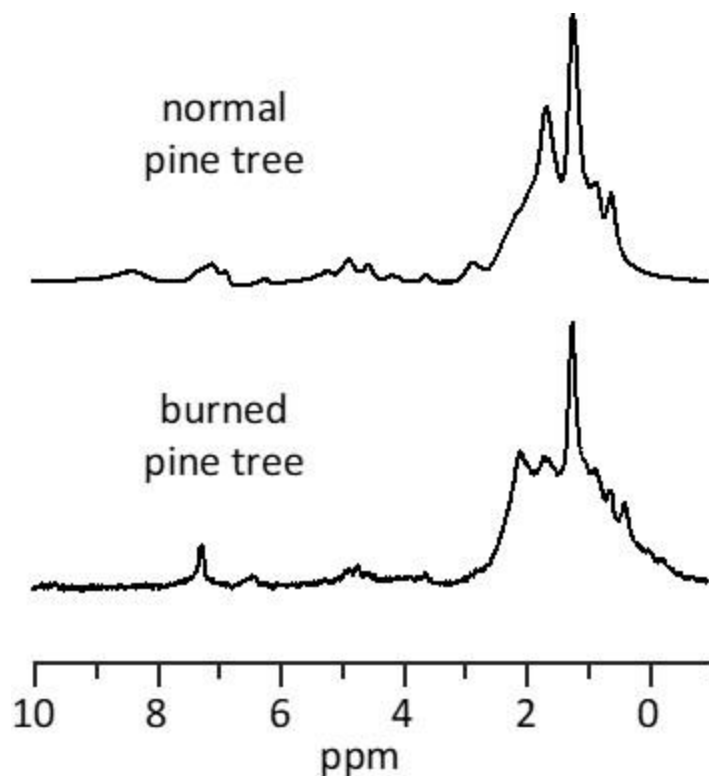


Figure 7.2. NMR spectrum of healthy and burned coniferous tree resins in CDCl_3 .

7.3 Multiple Quantum Coherence Experiments: Detection of J-Coupling at Low Fields

Unfortunately, not all samples can be easily dissolved and placed into a 5 mm glass tube to measure with a high field spectrometer, even if the spectrometer is portable. This motivates a return to single sided, low field magnets that can accommodate a much wider variety of samples. The challenge of resolution remains the foremost issue to tackle to enable structural specificity from low field measurements. However, different chemical information can be gained depending on the nature of the pulse sequence that is implemented. By selecting for specific quantum states that evolve during the delays with techniques such as a multiple quantum filter (MQF), it is possible to gain information other than T_1 , T_2 , and D from low-field experiments, such as J-coupling [2]. With mobile instruments, these couplings are generally inaccessible via the traditional method of resolving the hyperfine structure of a frequency spectrum. An

MQF can selectively generate a signal from “forbidden” double quantum transitions, which reveal the J-couplings of a chemical structure through spin echo modulation. Moreover, the width of this J modulation yields information relating to the network size or polymer length of a material. Additionally, singlet states can be generated by a mixture of zero and double quantum coherences; they have relaxation times about one order of magnitude longer than the typically observed triplet states, and can be used to study slow dynamic processes.

This approach is worth keeping in mind for future field-based measurements of porous media and heterogeneous, macroscopic systems that are more accessible with single sided magnets (geological sediment sampling, biofilms in thermal springs, industrial “vats”, etc.). Field measurements of this nature could be enabled by combining the MQF filter with alternative sensor designs, involving a flat coil snapped into place on top of a magnet.

References

- [1] Freitas DS, Carlos EF, Gil MCSS, Vieira LGE, Alcantara GB. NMR-Based Metabolomic Analysis of Huanglongbing-Asymptomatic and -Symptomatic Citrus Trees. *Journal of Agricultural and Food Chemistry*. 2015;63(34):7582-7588.

- [2] Levitt M. Spin Dynamics: Basics of Nuclear Magnetic Resonance. John Wiley & Sons, Ltd, New York, NY, 2001.

8. CONCLUSION

I was taught that the way of progress was neither swift nor easy.

– Marie Curie, 1867 – 1934

This dissertation primarily focused on the diverse applications of portable nuclear magnetic resonance. It opened with a brief discussion of the theory of magnetic resonance in Ch. 1, with a consideration of both classical and quantum mechanical descriptions of dynamic spin systems. This was followed in Ch. 2 by an overview of nuclear spin relaxation, from the foundational mechanics to the experimental measurement of this phenomenon.

Next, due to the growing need to operate in the low signal-to-noise regime to obtain portable measurements at low field strengths, filtering was developed in Ch. 3 as a way to essentially make “poor signals good” for experiments performed in compromising environments, of complex materials, or otherwise inhomogeneous or difficult systems. The matrix pencil method (MPM) was presented as a tool that can be used for both filtering and subsequent data analysis and parameter estimation.

The MPM is described as an alternative to the ILT for data processing, due to its low noise sensitivity, high resolution, and minimal computational requirements in Ch. 4. This advantage is gained primarily by exploiting the eigenstructure of a matrix pencil, which can be formulated directly from discretely sampled data, thereby avoiding integral transforms. In the cases presented here, the MPM outperforms the ILT in speed, resolution, and accuracy, suggesting that the MPM is better suited for rapid analysis of data in low-field settings. In the limit of zero noise, the MPM provides an analytically exact, closed-form solution to the problem of multi-exponential decomposition. The key for widespread future

implementation and automation of the MPM is to combine it with effective noise filters, such as MPM reconstruction itself, or, alternatively, singular value decomposition, multi-point moving averaging, integration smoothing methods, wavelet transforms, and sliding Fourier transform apodization. This will ultimately enable measurements of systems that have previously been inaccessible with portable NMR.

The final chapters demonstrate useful applications of NMR in field-based settings. First, Ch. 5 shows a clinical study of blood plasma to demonstrate a field application of portable NMR. Here, a rapid correlation of blood sample T_2 with water content was used to improve upon the accuracy of current methods of plasma water measurement. Next, the measurement of rheological properties in an in-line, factory-type setting is explored in Ch. 6. Finally, Ch. 7 opens the discussion of portable, high field structure analysis for agricultural and environmental purposes. The goal of these sections is to illustrate the diverse and creative possibilities for using portable NMR to solve emerging problems in the world today.

The theory, applications, and results presented here demonstrate that portable NMR is a technology of the future. By taking an interdisciplinary approach to couple new data analysis techniques with creative hardware design, the reach of magnetic resonance can be extended to address new problems and, ultimately, to push forward this field in ways that would have seemed unrealistic ten years ago.